ABSTRACT

Title of dissertation: PROBLEMS IN SPATIOTEMPORAL CHAOS

Matthew Tyler Cornick
Doctor of Philosophy, 2007

Dissertation directed by: Edward Ott
Department of Physics

In this thesis we consider two problem areas involving spatiotemporally chaotic systems. In Part I we investigate data assimilation techniques applicable to large systems. Data assimilation refers to the process of estimating a system's state from a time series of measurements (which may be noisy or incomplete) in conjunction with a model for the system's time evolution. However, for practical reasons, the high dimensionality of large spatiotemporally chaotic systems prevents the use of classical data assimilation techniques such as the Kalman filter. Here, a recently developed data assimilation method, the local ensemble transform Kalman Filter (LETKF), designed to circumvent this difficulty is applied to Rayleigh-Bénard convection, a prototypical spatiotemporally chaotic laboratory system. Using this technique we are able to extract the full temperature and velocity fields from a time series of shadowgraphs from a Rayleigh-Bénard convection experiment. The process of estimating fluid parameters is also investigated. The presented results suggest the potential usefulness of the LETKF technique to a broad class of laboratory experiments in which there is spatiotemporally chaotic behavior.

In Part II we study magnetic dynamo action in rotating electrically conducting fluids. In particular, we study how rotation effects the process of magnetic field growth (the dynamo effect) for a externally forced turbulent fluid. We solve the kinematic magnetohydrodynamic (MHD) equations with the addition of a Coriolis force in a periodic domain. Our results suggest that rotation is desirable for producing dynamo flows.

PROBLEMS IN SPATIOTEMPORAL CHAOS

by

Matthew Tyler Cornick

Dissertation submitted to the Faculty of the Graduate School of the
University of Maryland, College Park in partial fulfillment
of the requirements for the degree of
Doctor of Philosophy
2007

Advisory Committee:
Professor Edward Ott, Chair/Advisor
Professor Brian Hunt
Dr. Istvan Szunyogh
Professor Thomas Antonsen
Professor Daniel Lathrop

Preface

This thesis is organized into two parts. Both are concerned with the study of spatiotemporal chaos, a form of chaos characterized by disorder in both space and time. Spatiotemporal chaos often arises in spatially extended systems which have a finite correlation length; in particular, those which have a correlation length much smaller than the full system size. These complex systems are high dimensional; they have many (often hundreds or thousands) of dynamical degrees of freedom. Examples of spatiotemporal chaos have been found in optics [1], chemical and biological media [2], and hydrodynamics [3, 4], including geophysical flows in the ocean and atmosphere.

Part I is concerned with the problem of state and parameter estimation in spatiotemporally chaotic systems. In particular we study the problem in relation to a common experimental system, Rayleigh-Bénard convection. In Part II we report on results from magnetohydrodynamic simulations of rotating turbulence.

Often spatiotemporal chaos is distinguished from turbulence [5, 6], and thus many geophysical flows, such as the atmosphere (which is highly turbulent) and magnetohydrodynamic turbulence, would not be classified as spatiotemporal chaos. For our purposes this distinction is unimportant, but it is instructive to discuss the differences. Consider the various length scales in a system. The size of the full system is denoted D while the correlation length is denoted ξ_c. In addition, the length scale at which energy is introduced into the system is l_E, while the length scale at which energy is dissipated (usually the smallest scale in the system) is l_D. When $l_D \ll l_E$

the system is said to be turbulent. While for $l_D \sim l_E$, the system may exhibit low dimensional *temporal* chaos ($\xi_c \sim D$) or spatiotemporal chaos ($\xi_c \ll D$). Despite this distinction, both turbulence and spatiotemporal chaos are high dimensional, spatially disordered states. Part II is concerned with a turbulent type of chaos, while Part I is concerned mainly with Rayleigh-Bénard convection, an example of non-turbulent spatiotemporal chaos. However, many of the results and techniques described in Part I can (and have) been applied to turbulent systems (in particular, for the purpose of weather forecasting).

Dedication

For my wife, and Mr. Magney.

Acknowledgments

Over the many years of my education there have been several people who have have influenced me to take the path towards a physics Ph.D. Two high school teachers in particular, Mr. Magney and Mr. Rischling, were vital in my decision to study Physics from the beginning. Their constant encouragement was a powerful motivator. As an undergraduate, my advisor Dr. Field had a tremendous effect on my decision to study physics in graduate school. He constantly took interest in my growth and understanding.

I owe my gratitude to the University of Maryland. I would especially like to thank my advisor Edward Ott who provided his wisdom and experience throughout my years at UMD. I would also like to thank him for his text on Dynamical Systems, which, as a undergraduate, captured my interest and greatly influenced my choice of graduate school. Thanks to Brian Hunt, who gave me valuable advice on many occasions. I am also tremendously grateful for the direction and advice provided by Tom Antonsen and Dan Lathrop, for Mike Schatz who always made me feel welcome during visits to Georgia Tech, and for Alex Dragt who gave me my first opportunity at graduate research. Thanks to Nick Mecholsky for always having an interesting problem to solve, and to Young-Noh Yoon, who constantly reminded me that even the most basic things can be questioned. I am grateful to Laurette Tuckerman for providing her Fortran code for simulating the Boussinesq equations.

Of course, without the encouragement of my parents, none of this would have been possible. My father's passion for science and nature drove me to similar inter-

ests. Lastly, thanks to my wife, who was with me at every step, and who reminds me that the most important things cannot be found in a text book.

Table of Contents

List of Tables

List of Figures

List of Abbreviations

KF	Kalman filter
EKF	extended Kalman filter
EnKF	ensemble Kalman filter
LEKF	local ensemble Kalman filter
LETKF	local ensemble transform Kalman filter
RMS	root mean square
MHD	magnetohydrodynamics
FFT	fast Fourier transform
CFL	Courant-Friedrichs-Levy

Part I

PARAMETER AND STATE ESTIMATION IN EXPERIMENTS EXHIBITING SPATIOTEMPORAL CHAOS

Chapter 1

Introduction

Estimation of the state of an evolving dynamical system from measurements is often a prerequisite for prediction and control of the system. However, obtaining the system state is a common experimental difficulty for many spatiotemporally chaotic systems, where available measurements may be incomplete and noisy. When an approximate model for the system is available, it can be used in conjunction with incoming measurements to estimate the evolving system state, a process referred to as 'data assimilation'.

Most data assimilation algorithms are iterative, cycling between a predict and update step once every time interval Δt. In the update step, current measurements are used to update (or correct) the prediction. The prediction step then propagates the updated state, via the model, to the next measurement time (*i.e.*, it is a short term forecast). The aim of this process is to synchronize the system and its model by coupling them via the measurements.

The Kalman filter [7], described in Section 1.3, optimally solves the data assimilation problem for systems with linear dynamics. Several methods extending the Kalman filter methodology to nonlinear systems have been proposed, including the extended Kalman filter (EKF) [8] (Section 1.3), and the class of ensemble Kalman filters (EnKF) [9] (Section 1.4). Straightforward application of these methods to *large*

spatiotemporally chaotic systems is often completely infeasible. In particular, the EKF requires inversion of $N \times N$ matrices, where N is the number of model variables. This can be quite prohibitive; for a discretized partial differential model evolving M scalar spatial fields in time, the number of model variables is M multiplied by the number of grid points (which can number in the millions). In addition, the ensemble (EnKF) methods require prohibitively large ensemble sizes when applied to high-dimensional systems. Despite these difficulties, recent developments [10, 11, 12] from the field of numerical weather prediction [13, 14, 15, 16, 17, 18] suggest the possibility of achieving good accuracy (as in a Kalman filter), but in a way that is computationally feasible for large nonlinear systems.

In this thesis we demonstrate the efficacy of a new method, the local ensemble transform Kalman filter (LETKF) [12] (Chapter 2). Although originally motivated by application to weather prediction, the LETKF is potentially broadly applicable to any large spatiotemporally chaotic system. In particular, we investigate Rayleigh-Bénard convection (Section 1.1). Flows such as *spiral defect chaos* [19, 3] in the Rayleigh-Bénard problem are, perhaps, the best studied experimental examples of spatiotemporal chaos; nevertheless, many general aspects of spiral defect chaos remain poorly understood.

The LETKF is motivated by the observation that spatiotemporally chaotic systems exhibit a finite correlation length much smaller than the system size. Frequently, regions much smaller than the system size can be described by relatively few degrees of freedom. With this in mind, the LETKF employs many independent data assimilations in a set of overlapping local regions, each with a characteristic

length on the order of the correlation length. Because these regions are relatively small, their individual computations are not prohibitive. Furthermore, by use of a simple example [10, 11] it was indicated that, by exploiting localization in this way, state estimates with accuracies virtually the same as those for a classical Kalman filter technique (thus presumably of near optimal accuracy) can be achieved.

What follows is an introduction to Rayleigh-Bénard convection in Section 1.1 and an introduction to the classical methods of data assimilation in Sections 1.2, 1.3, and 1.4. Details of the LETKF algorithm, as well as our application of the LETKF to Rayleigh-Bénard convection is described in Chapter 2. Tests of the accuracy of the LETKF are presented in Sections 3.1 and 3.2, in which we investigate performance with extremely sparse/noisy measurements and test extensions of the LETKF for estimating model parameters.

1.1 Rayleigh-Bénard Convection

In Rayleigh-Bénard convection, a horizontal fluid layer of thickness d is confined between a heated lower plate and a cooled upper plate. For a temperature difference between the plates ΔT that is sufficiently small, the fluid is at rest, and heat is transported by conduction. In this state, the temperature rises linearly from the lower boundary with temperature T_H to the upper boundary with temperature $T_C = T_H - \Delta T$. The onset of fluid motion occurs when buoyancy overcomes viscous dissipation and thermal diffusion as ΔT is raised above a critical value ΔT_c.

Initial analytic work on Rayleigh-Bénard convection showed that, in a space

of infinite horizontal extent, the system has a stable state consisting of parallel convection rolls. However, Rayleigh-Bénard convection was recently shown [3] to support a type of spatiotemporal chaos which has been named spiral defect chaos due to the abundance of spiral structures and roll defects present in the evolving state. This state has been extensively studied theoretically, numerically, and experimentally [20, 21, 22, 23, 24, 25, 6, 3, 26]. For a recent review of Rayleigh-Bénard convection see [19].

Rayleigh-Bénard convection is typically modeled using the Boussinesq equations [27], which are commonly nondimensionalized with temperature scaled by ΔT, length scaled by d, and time scaled by the vertical diffusion time $t_v = d^2/\kappa$, where κ is the thermal diffusivity. This system of units is used throughout Part I of this thesis. The temperature field is denoted T, while the temperature deviation from the conducting static solution is denoted θ; $T(x,y,z) = \Delta T\theta(x,y,z) + T_H - \Delta T\frac{z}{d}$. We solve the Boussinesq equations in the disk shaped region $x^2 + y^2 \leq \Gamma^2$, $|z| \leq \frac{1}{2}$, with Dirichlet boundary conditions $\mathbf{u} = 0$, $\theta = 0$ on all walls. Γ is the radius of the disk in units of d and is often referred to as the aspect ratio. The θ boundary condition represents the situation which would occur for a conducting wall (when the wall's thermal conductivity much higher than the fluid's thermal conductivity). In terms the fluid's velocity $\mathbf{u}$, temperature deviation θ, and pressure p, the Boussinesq equations take the form

$$\begin{aligned} \left(\frac{\partial}{\partial t} + \mathbf{u}\cdot\nabla\right)\mathbf{u} &= -\nabla p + Pr\nabla^2\mathbf{u} + PrR\,\theta\,\hat{\boldsymbol{z}}\,, \\ \left(\frac{\partial}{\partial t} + \mathbf{u}\cdot\nabla\right)\theta &= \nabla^2\theta + \mathbf{u}\cdot\hat{\boldsymbol{z}}\,, \end{aligned} \tag{1.1}$$

$$\nabla \cdot \mathbf{u} \;=\; 0\,.$$

These equations have two dimensionless parameters, the Rayleigh number R and the Prandtl number Pr,

$$R = \frac{g\alpha d^3 \Delta T}{\nu\kappa},\; Pr = \frac{\nu}{\kappa}. \tag{1.2}$$

Here α is the thermal expansion coefficient, ν is the kinematic viscosity, and g is gravitational acceleration (in the $-\hat{\boldsymbol{z}}$ direction). The critical Rayleigh number for convective onset is $R_c \approx 1707$. The *reduced* Rayleigh number

$$\epsilon = \frac{R - R_c}{R_c} = \frac{\Delta T - \Delta T_c}{\Delta T_c} \tag{1.3}$$

measures the amount above onset. Fluid convection arises when $\epsilon > 0$.

We have investigated the parameter region near $\epsilon = 1$, $Pr = 1$. At these values of ϵ and Pr, the spatiotemporally chaotic state known as spiral defect chaos can arise [3, 19]; however, in our studies using $\Gamma \approx 20$, the region is too small to support the large spirals typically seen in spiral defect chaos. Nevertheless, the convective flows in our studies exhibit complex behavior in both space and time. See Fig. 1.1 for an example of the spatial structure of the evolving state (the images show simulated shadowgraphs, an imaging technique described in Section 1.1.1).

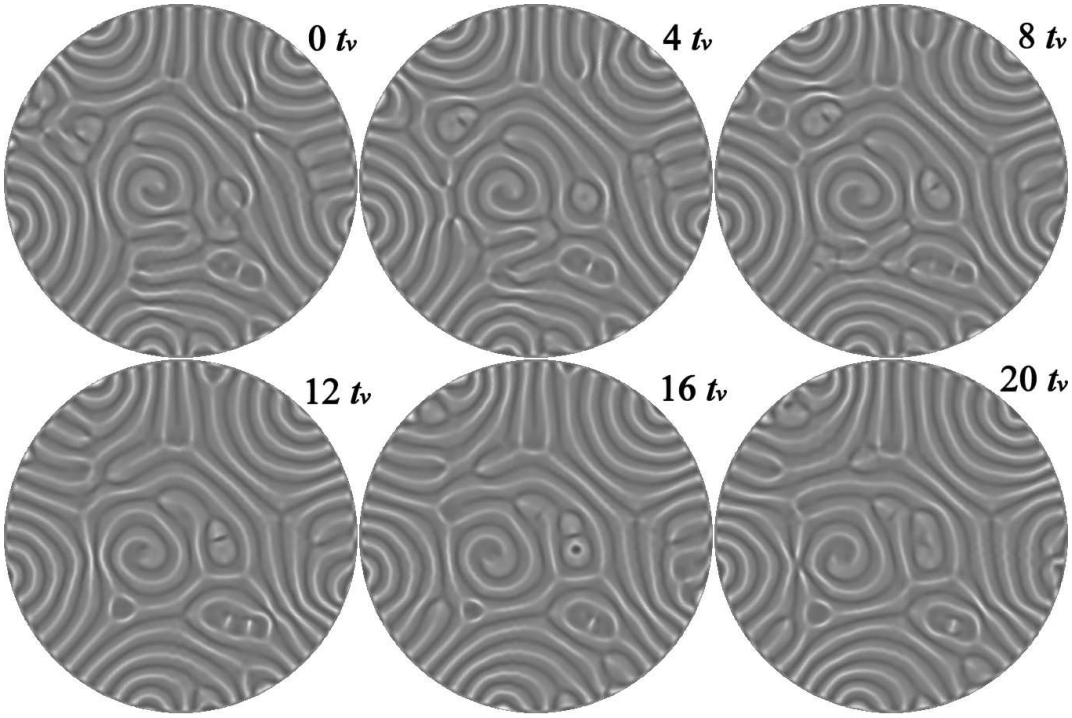

Figure 1.1: Images from simulated Rayleigh-Bénard convection ($\epsilon = 1$, $\Gamma = 20$), demonstrating the time evolution of a typical system state. White represents cold descending fluid, while black represents warm rising fluid.

The z-dependence of the $\theta(x, y, z)$ field from a typical state on the system attractor exhibits asymmetry about $z = 0$, as shown in Fig. 1.2.

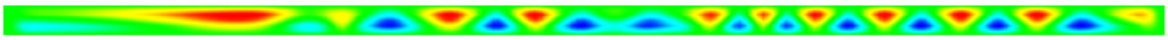

Figure 1.2: The z-dependence of the temperature deviation is shown in this cross-section (the $x = 0$ plane). Red indicates that the temperature is higher than the conducting profile, whereas blue indicates that it is lower.

Our technique for integrating equations (1.1) is the pseudospectral method

described in [28]. Briefly, it uses a backward Euler time step for the linear terms, and a second order Adams-Bashforth method for the nonlinear terms. All fields are expressed in terms of their Fourier components in the periodic azimuthal ϕ direction, and in terms of Chebyshev polynomials in the bounded directions $-1/2 < z < 1/2$ and $0 < r < \Gamma$. Thus the physical space representation exists on a mesh of grid points $(r_m,\ \phi_n,\ z_l)$ which are evenly spaced in ϕ and located at the Chebyshev points in z and r; $\phi_n = \frac{2\pi n}{N_\phi},\ r_m = \Gamma\cos(\frac{\pi(m-1)}{2(N_r-1)}),\ z_l = \frac{1}{2}\cos(\frac{\pi(l-1)}{N_z-1})$. Here, the number of grid points in the r, z, and ϕ direction are N_r, N_z, and N_ϕ respectively.

The dynamics of this system are driven by two instabilities. The skewed varicose instability, for large wave numbers (small wavelengths) and the Eckhaus instability (dilation instability), associated with small wave numbers (large wavelengths). Between these extremes lie stable wave numbers inside the *Busse balloon*, a compact region of stable wavelengths in the space $(\epsilon,\ k)$. The motion of defects in the roll planform are ultimately a consequence of these instabilities.

Small structures (defects) rapidly evolve on a time scale of approximately one vertical diffusion time. Large structures evolve on a time scale of one *horizontal* diffusion time $t_h = \Gamma^2 t_v$. The correlation length ξ decreases with increasing ϵ approximately according to a power law, $\xi \sim \epsilon^{-1/2}$ [19]. For the investigated parameter region $(Pr,\ \epsilon \approx 1)$ the correlation length of this system is much smaller than the diameter of the domain; approximately $2d$ to $3d$.

Other than the Boussinesq equations, several models for Rayleigh-Bénard convection have been proposed and studied [6]. In particular, the modified Swift-Hohenberg equations [29, 30] reduce the problem to two dimensions; compared to

three dimensions for the full Boussinesq equations (and thus they may be simulated more easily than the full Boussinesq equations). These equations are used to model many spatiotemporally chaotic phenomena, including spatiotemporal chaos in lasers [31]. They are

$$\frac{\partial \psi}{\partial t} + g_m \mathbf{u} \cdot \boldsymbol{\nabla} \psi = \left[\epsilon' - (1 + \nabla^2)^2\right] \psi - \Psi^3, \tag{1.4}$$

$$\frac{\partial v}{\partial t} = \left[\frac{\partial \psi}{\partial y}\frac{\partial f}{\partial x} - \frac{\partial \psi}{\partial x}\frac{\partial f}{\partial y}\right] + Pr\left(\nabla^2 - c^2\right) v. \tag{1.5}$$

The ψ field is similar to the midplane temperature field of the Boussinesq equations, the $v = \nabla^2 \zeta$ field is vertical vorticity of the fluid flow $\mathbf{u} = \frac{\partial \zeta}{\partial y}\hat{\boldsymbol{x}} - \frac{\partial \zeta}{\partial x}\hat{\boldsymbol{y}}$, and $f = \nabla^2 \psi$. The parameter ϵ' is related to ϵ via the relation $\epsilon' \approx 2.78\epsilon$. These equations, when simulated with boundary conditions $\psi = v = \zeta = f = 0$ on the boundary of a circular region, result in patterns very similar to those found in experiments on Rayleigh-Bénard convection. In particular, large rotating spirals and defects are present. Although these equations produce qualitatively similar solutions to the Boussinesq equations, they exhibit spiral defect chaos only as a transient behavior. Thus, in contrast to the full Boussinesq equations, spiral defect chaos does not occur on the Swift-Hohenberg attractor. Because of this drawback we decided to use the full Boussinesq equations as our model of Rayleigh-Bénard convection, despite the computational complexity of simulating a full three dimensional domain.

Spiral defect chaos in Rayleigh-Bénard convection exhibits sensitivity to initial conditions. It is instructive to demonstrate the error growth of an initial perturbation. To do so, we simulate two fluid states, one termed the *reference*, and the other which is identical to the reference state except for a small local perturbation in the

initial condition. The state of the reference field is denoted $T_r(x, y, z), \mathbf{u}_r(x, y, z)$, while the perturbed state is denoted $T(x, y, z), \mathbf{u}(x, y, z)$. Fig. 1.3 shows a sequence of images demonstrating the nonlinear growth of $T(x, y, 0) - T_r(x, y, 0)$ (in the mid-plane $z = 0$). The error initially decays, and the two states remain close for several t_v. When the states diverge it is usually at the location of a defect. For example, in the reference state a roll may be pinched off by the action of the skewed varicose instability forming a defect while the second state may not undergo the pinch-off event. This defect related error growth quickly spreads across the entire disk in a time much less than the horizontal diffusion time. This highlights an important property of spiral defect chaos; the dynamics are stable to small local perturbations almost everywhere. It is only near some defects that the perturbation grows. This was shown in [20]. The Lyapunov vector associated with the largest Lyapunov exponent is negative almost everywhere (except near a few defects, where it is large and positive).

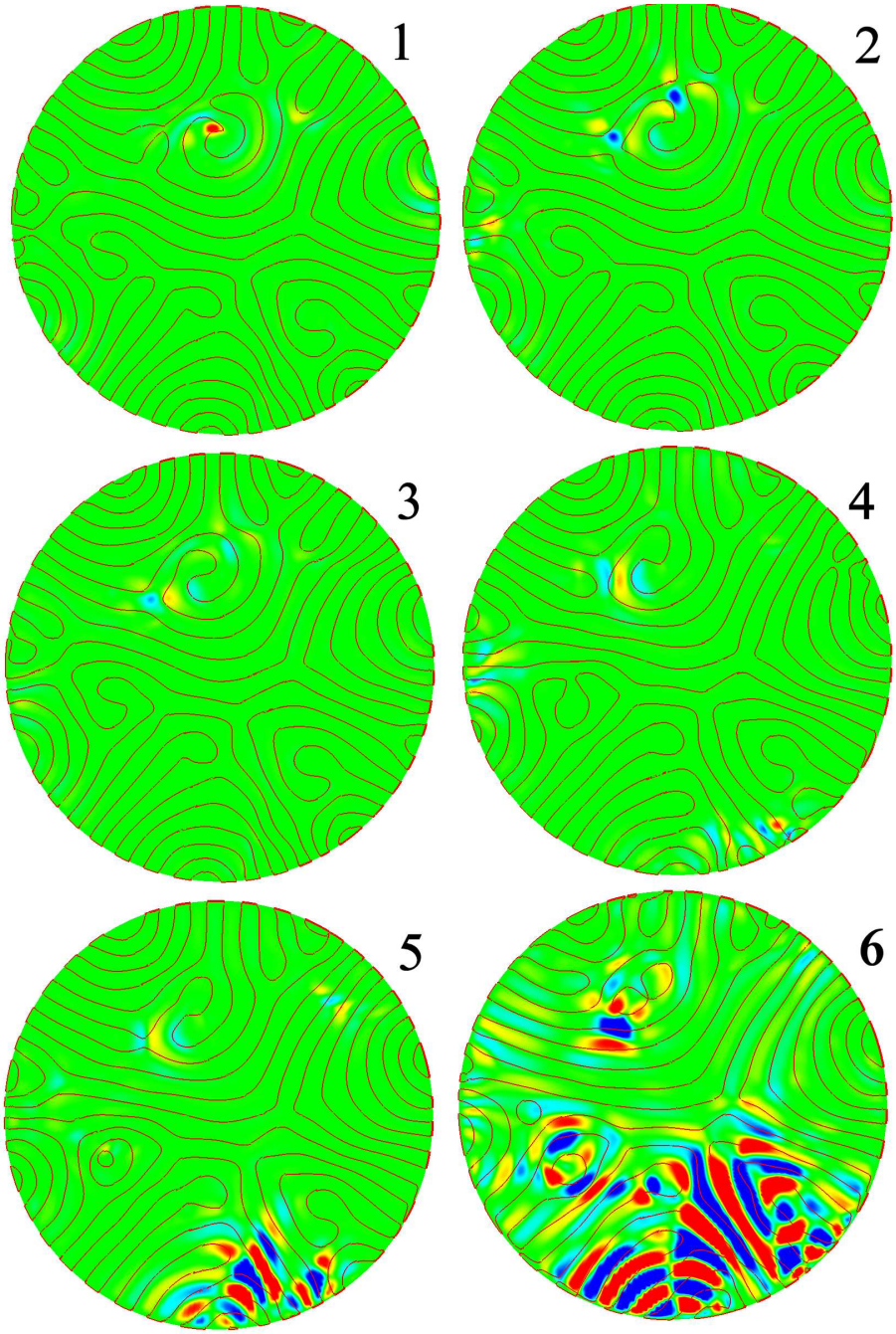

Figure 1.3: Sequence of images showing the growth of a small initial perturbation located in the upper center of the disk at frame 0. Contours are the curves for which $T_r(x, y, 0) = 0$. Red indicates a slightly warmer midplane temperature than the reference state, while blue indicates a slightly cooler temperature. The time spanned between frame 0 and frame 6 is approximately $10t_v$.

1.1.1 The Shadowgraph Method

In experiments, Rayleigh-Bénard flows are visualized using the shadowgraph method [32]. The typical setup consists of a reflecting bottom plate and a transparent top plate, confining the (transparent) fluid. Light shines down through the fluid, reflects from the bottom plate, travels up through the fluid and out of the disk region. The exiting light is modified by the index of refraction of the fluid (which has a slight temperature dependence) and imaged via a CCD camera. With this method the vertically integrated temperature field of the fluid is indirectly measured.

We connect the shadowgraph light intensity $I(x, y)$ to the temperature field in the flow using the relation derived from geometric optics [32, 33]

$$I(x, y) = \frac{I_\circ(x, y)}{1 - a\nabla_\perp^2 \bar{\theta}(x, y)}. \tag{1.6}$$

Here, $\nabla_\perp^2 \equiv \partial^2/\partial x^2 + \partial^2/\partial y^2$ is the horizontal Laplacian, and the temperature field is vertically averaged: $\bar{\theta}(x, y) \equiv \int \theta(x, y, z)\mathrm{d}z$. $I_\circ(x, y)$ is the incident light intensity and $a = 2z_1|dn/dT|$, where n is the index of refraction of the fluid, z_1 is the optical path length from the midplane of the fluid layer to the image plane (in units of d), and the temperature coefficient of the index of refraction $|dn/dT|$ is evaluated at the average temperature of the fluid layer. Equation (1.6) is derived in Appendix A. For geometric optics to be valid, the condition $\|a\nabla_\perp^2 \bar{\theta}\| \ll 1$ must hold.

This remote sensing method represents an incomplete observation of the full fluid state. The z-dependence of the temperature field is unmeasured, as is the entire velocity field. The velocity field is largely composed of the circulating roll velocity. However, there is a smaller dynamically important component to the velocity field

known as the mean flow $\bar{\mathbf{u}}(x, y)$ (which advects the roll pattern),

$$\bar{\mathbf{u}}(x, y) \equiv \int \mathbf{u}_\perp(x, y, z)\, \mathrm{d}z, \tag{1.7}$$

where $\mathbf{u} = \mathbf{u}_\perp + u_z \hat{\boldsymbol{z}}$. This component of the velocity field plays a significant role in the dynamics [24] and is difficult to measure in the experiments. In order to achieve prediction and control of Rayleigh-Bénard convection, accurate estimates of the fluid state are required, including the mean flow. Thus we pursue the use of data assimilation techniques for the purpose of estimating the fluid state $(\mathbf{u}(x, y, z),\ \theta(x, y, z))$ from a sequence of shadowgraph images.

1.2 Data Assimilation

In the most general situation, we are given a time series of measurements from a particular dynamical system, where the measurements are made at the times t_j $(j = 1, 2 \ldots)$. These measurements may not describe the system state $\boldsymbol{\xi}$ exactly; they may be incomplete, sparse, or noisy. Suppose that, at each time, a measurement may be written as a collection of scalar quantities so that we can represent a measurement by a s-component vector $\boldsymbol{y}$, and the time series as the collection of the vectors $\boldsymbol{y}_1,\ \boldsymbol{y}_2,\ \ldots$. Our goal, at each time t_j, is to infer the N component system state $\boldsymbol{\xi}_j$ from the time series $\boldsymbol{y}_1,\ \boldsymbol{y}_2,\ \ldots$.

We begin with the dynamical model,

$$\boldsymbol{\xi}_{j+1} = \boldsymbol{G}(\boldsymbol{\xi}_j), \tag{1.8}$$

which describes the time evolution of the system from a time t_j to t_{j+1}. In this thesis we shal not consider the situation where there is an added random component on

the right hand side of (1.8). We assume the system evolves in continuous time,

$$\frac{\mathrm{d}\boldsymbol{\xi}}{\mathrm{d}t} = \mathbf{F}(\boldsymbol{\xi}), \tag{1.9}$$

so that $\boldsymbol{G}$ is an integration of (1.9) from $t = t_j$ to t_{j+1}. $\boldsymbol{G}$ may be exact, though generally it describes only approximately the dynamics of the true system. This discrepancy, when it exists, is known as model error. In addition, we assume that measurements are ideally (in the absence of measurement noise) uniquely determined by the system state, $\boldsymbol{y} = \boldsymbol{M}(\boldsymbol{\xi})$. $\boldsymbol{M}$ is known as an *observation operator*, the mapping of $\boldsymbol{\xi}$ into the observation space; it need not be a one-to-one mapping. When measurement noise is present, individual measurements take the form $\boldsymbol{y}_j = \boldsymbol{M}(\boldsymbol{\xi}_j) + \boldsymbol{\delta}$. Here, $\boldsymbol{\delta}$ represents a random error, which is assumed to be normally distributed with mean zero and $(s \times s)$ covariance matrix $\boldsymbol{R}$. In addition to model error, the observation operator $\boldsymbol{M}$ may be approximate. We refer to this form of error as observation operator error.

There are many ways to view the above problem. In one sense it can be thought of as an inversion problem: find $\boldsymbol{\xi}_1,\ \boldsymbol{\xi}_2,\ \ldots$ given $\boldsymbol{y}_1,\ \boldsymbol{y}_2,\ \ldots$. Even though $\boldsymbol{M}$ may not be invertible, this is possible because *all* measurements can be used, in conjunction with the model, to determine *each* $\boldsymbol{\xi}_j$. In other words, each individual $\boldsymbol{y}_j$ may not contain enough information to determine the state $\boldsymbol{\xi}_j$, but the entire time series $\boldsymbol{y}_1,\ \boldsymbol{y}_2,\ \ldots$ contains quite a bit of information, potentially enough to obtain any individual $\boldsymbol{\xi}_j$.

In a different sense, we can think of the problem as finding the trajectory in state space satisfying (1.8) that, when projected into the observation space, best fits

the measured time series. In this sense we can construct a quadratic cost function to be minimized in order to obtain a maximum likelihood estimate of the trajectory. Since we have assumed measurement noise follows Gaussian statistics, the most sensible cost at each time is given by $c(\boldsymbol{\xi}, \boldsymbol{y}) = (\boldsymbol{M}(\boldsymbol{\xi}) - \boldsymbol{y})^T \boldsymbol{R}^{-1} (\boldsymbol{M}(\boldsymbol{\xi}) - \boldsymbol{y})$. To see why this form is used, consider the vector $\boldsymbol{\Delta} = \boldsymbol{S}^{-1}(\boldsymbol{M}(\boldsymbol{\xi}_j) - \boldsymbol{y}_j)$ where $\boldsymbol{S}$ is real and symmetric and solves $\boldsymbol{S}^2 = \boldsymbol{R}$. We have $c(\boldsymbol{\xi}, \boldsymbol{y}) = (\boldsymbol{M}(\boldsymbol{\xi}) - \boldsymbol{y})^T \boldsymbol{S}^{-1} \boldsymbol{S}^{-1} (\boldsymbol{M}(\boldsymbol{\xi}) - \boldsymbol{y}) = \boldsymbol{\Delta}^T \boldsymbol{\Delta} = |\boldsymbol{\Delta}|^2$. Roughly speaking, the cost is then the square 'distance' between $\boldsymbol{\xi}$ and $\boldsymbol{y}$ in units of the number of standard deviations they are separated in the observation space.

The trajectory is uniquely determined from the state at ant particular time t_k: $\boldsymbol{\xi}_j = \boldsymbol{G}^{j-k}(\boldsymbol{\xi}_k)\ \forall j$, where the notation $\boldsymbol{G}^n(\xi)$ means applying $\boldsymbol{G}$ to $\boldsymbol{\xi}$ n times ($\boldsymbol{G}$ is invertible so n may be negative). Using this notation, the cost of a trajectory is given by

$$C(\boldsymbol{\xi}_k) = \sum_j c(\boldsymbol{G}^{j-k}(\boldsymbol{\xi}_k), \boldsymbol{y}_j),$$

where the trajectory is constrained to pass through the point $\boldsymbol{\xi}_k$ at time t_k.

Yet another perspective would be to look at the problem as a synchronization problem, as alluded to in the introduction. If we can use the measurements to synchronize the model with the true system, we will have obtained a trajectory similar to the one sought above.

The last two perspectives, that of synchronization, or finding the trajectory with maximum likelihood, are instructive. They propose not only ways of thinking about the problem, but ways of solving it as well, *i.e.* by synchronizing the model

to the true system, or by minimizing a cost function. When $\boldsymbol{G}$ and $\boldsymbol{M}$ are linear, there is a solution which accomplishes all the above objectives, the Kalman filter.

1.3 The Kalman Filter

Suppose that the model and observation operator are linear, $\boldsymbol{G}(\boldsymbol{\xi}) = \boldsymbol{Q}\boldsymbol{\xi}$, and $\boldsymbol{M}(\boldsymbol{\xi}) = \boldsymbol{H}\boldsymbol{\xi}$, where $\boldsymbol{H}$ and $\boldsymbol{Q}$ are matrices of size $s \times N$ and $N \times N$, respectively. The Kalman filter is an recursive Bayesian approach to the problem of state estimation. It is provably optimal given the statement of the problem (Gaussian measurement noise, linear $\boldsymbol{G}$ and $\boldsymbol{M}$). Before describing the Kalman filter, we introduce the concepts of Bayesian estimation.

1.3.1 Bayesian Estimation

Suppose we have a probability distribution function (PDF) $p(\boldsymbol{\xi})$ representing our knowledge of the system state. It is unimportant how exactly we came about this information. When a new piece of information comes along, in the form of a measurement $\boldsymbol{y}$, we wish to update the PDF to reflect the new information. Denote the conditional probability of measuring $\boldsymbol{y}$, given that the state is $\boldsymbol{\xi}$, as $p(\boldsymbol{y}|\boldsymbol{\xi})$. Using Bayes' rule, the new PDF of the state, reflecting the new information provided by the measurement is then

$$p(\boldsymbol{\xi}|\boldsymbol{y}) = \frac{p(\boldsymbol{y}|\boldsymbol{\xi})p(\boldsymbol{\xi})}{p(\boldsymbol{y})}, \tag{1.10}$$

where $p(\boldsymbol{y}) = \int p(\boldsymbol{y}|\boldsymbol{\xi})p(\boldsymbol{\xi})\mathrm{d}\boldsymbol{\xi}$ is simply a normalizing factor. If we make the assumption that $p(\boldsymbol{\xi})$ is Gaussian, we have

$$p(\boldsymbol{\xi}) \sim \exp\left[-\frac{1}{2}(\boldsymbol{\xi} - \bar{\boldsymbol{\xi}}^p)^T \mathbf{P}^{-1}(\boldsymbol{\xi} - \bar{\boldsymbol{\xi}}^p)\right], \tag{1.11}$$

for some covariance matrix $\mathbf{P}$ and mean $\bar{\boldsymbol{\xi}}^p$. The assumption that measurement noise is Gaussian leads to

$$p(\boldsymbol{y}|\boldsymbol{\xi}) \sim \exp\left[-\frac{1}{2}(\boldsymbol{y} - \boldsymbol{H}\boldsymbol{\xi})^T \boldsymbol{R}^{-1}(\boldsymbol{y} - \boldsymbol{H}\boldsymbol{\xi})\right]. \tag{1.12}$$

Using equation (1.10) we get the updated PDF

$$p(\boldsymbol{\xi}|\boldsymbol{y}) \sim \exp\left[-\frac{1}{2}\left((\boldsymbol{y} - \boldsymbol{H}\boldsymbol{\xi})^T \boldsymbol{R}^{-1}(\boldsymbol{y} - \boldsymbol{H}\boldsymbol{\xi}) + (\boldsymbol{\xi} - \bar{\boldsymbol{\xi}}^p)^T \mathbf{P}^{-1}(\boldsymbol{\xi} - \bar{\boldsymbol{\xi}}^p)\right)\right]. \tag{1.13}$$

This PDF is Gaussian as well. Expressing $p(\boldsymbol{\xi}|\boldsymbol{y})$ in the form

$$p(\boldsymbol{\xi}|\boldsymbol{y}) \sim \exp\left[-\frac{1}{2}(\boldsymbol{\xi} - \bar{\boldsymbol{\xi}}^u)^T \boldsymbol{U}^{-1}(\boldsymbol{y} - \bar{\boldsymbol{\xi}}^u)\right], \tag{1.14}$$

leads to the relation

$$(\boldsymbol{\xi} - \bar{\boldsymbol{\xi}}^u)^T \boldsymbol{U}^{-1}(\boldsymbol{\xi} - \bar{\boldsymbol{\xi}}^u) + C_\circ = (\boldsymbol{y} - \boldsymbol{H}\boldsymbol{\xi})^T \boldsymbol{R}^{-1}(\boldsymbol{y} - \boldsymbol{H}\boldsymbol{\xi}) + (\boldsymbol{\xi} - \bar{\boldsymbol{\xi}}^p)^T \mathbf{P}^{-1}(\boldsymbol{\xi} - \bar{\boldsymbol{\xi}}^p). \tag{1.15}$$

The constant $C_\circ$ may take any value since it leavs $p(\boldsymbol{\xi}|\boldsymbol{y})$ proportional to $p(\boldsymbol{y}|\boldsymbol{\xi})p(\boldsymbol{\xi})$ (any normalization is fixed by the factor $p(\boldsymbol{y})$). In order for this relation to hold for all $\boldsymbol{\xi}$, we must have

$$\boldsymbol{U} = \left[\mathbf{P}^{-1} + \boldsymbol{H}^T \boldsymbol{R}^{-1} \boldsymbol{H}\right]^{-1}, \tag{1.16}$$

$$\bar{\boldsymbol{\xi}}^u = \boldsymbol{U}\left[\mathbf{P}^{-1}\bar{\boldsymbol{\xi}}^p + \boldsymbol{H}^T \boldsymbol{R}^{-1}\boldsymbol{y}\right]. \tag{1.17}$$

To summarize, beginning with an initial Gaussian PDF $p(\boldsymbol{\xi})$ with mean $\bar{\boldsymbol{\xi}}^p$ and covariance $\mathbf{P}$, we have included new information obtained from a measurement made

in the observation space with mean $\boldsymbol{y}$ and covariance $\boldsymbol{R}$. The end result is the *updated* PDF with mean $\bar{\boldsymbol{\xi}}^u$ and covariance $\boldsymbol{U}$, given by equations (1.16) and (1.17).

1.3.2 Kalman Filter Equations

With the tools of Bayesian estimation established, we proceed with the Kalman filter formulation. Note that, since $\boldsymbol{G}$ is linear, that a Gaussian PDF transforms, under the action of $\boldsymbol{G}$ to another PDF with Gaussian form. The PDF with mean $\bar{\boldsymbol{\xi}}^u_{j-1}$ and covariance $\boldsymbol{U}_{j-1}$ at a time t_{j-1} transforms into the PDF at time t_j with mean and covariance

$$\bar{\boldsymbol{\xi}}^p_j = \boldsymbol{Q}\bar{\boldsymbol{\xi}}^u_{j-1}, \tag{1.18}$$

$$\mathbf{P}_j = \boldsymbol{Q}\boldsymbol{U}_{j-1}\boldsymbol{Q}^T. \tag{1.19}$$

This PDF is known as the *predicted* PDF; it is then updated using (1.16) and (1.17), forming the *updated* PDF with mean and covariance,

$$\boldsymbol{U}_j = \left[\mathbf{P}_j^{-1} + \boldsymbol{H}^T\boldsymbol{R}^{-1}\boldsymbol{H}\right]^{-1}, \tag{1.20}$$

$$\bar{\boldsymbol{\xi}}^u_j = \boldsymbol{U}_j\left[\mathbf{P}_j^{-1}\bar{\boldsymbol{\xi}}^p_j + \boldsymbol{H}^T\boldsymbol{R}^{-1}\boldsymbol{y}_j\right]. \tag{1.21}$$

These update equations are often rewritten in the form

$$\boldsymbol{U}_j = \left(\boldsymbol{I} + \mathbf{P}_j\boldsymbol{H}^T\boldsymbol{R}^{-1}\boldsymbol{H}\right)^{-1}\mathbf{P}_j, \tag{1.22}$$

$$\bar{\boldsymbol{\xi}}^u_j = \bar{\boldsymbol{\xi}}^p_j + \boldsymbol{U}_j\boldsymbol{H}^T\boldsymbol{R}^{-1}(\boldsymbol{y}_j - \boldsymbol{H}\bar{\boldsymbol{\xi}}^p_j). \tag{1.23}$$

Equations (1.18), (1.19), (1.22), and (1.23) are the complete Kalman filter equations. In words, the Kalman filter evolves a PDF of the system state forward

in time with successive updates whenever measurements are made. This process of predict/update steps continues in an iterative fashion for all measurements in the time series. At any given time, the PDF represents the accumulated information provided by all previous assimilated measurements. The process typically begins with a covariance $\mathbf{P}_1$ which is large enough that the initial PDF spans the entire system attractor (or the range of possible system states).

1.3.3 The Extended Kalman Filter

In the case that $\boldsymbol{G}$ and $\boldsymbol{M}$ are not linear, we can still perform the Kalman filter steps by linearizing them about the current state estimate in equations (1.19), (1.22), and (1.23). Although this allows one to proceed with the computation, it is no longer provably optimal. However, if the nonlinearities are weak, or measurements are very frequent, linearization may be a successful strategy. We have the linear maps

$$\hat{\boldsymbol{G}}(\boldsymbol{\xi}, \boldsymbol{\xi}_\circ) = \boldsymbol{G}(\boldsymbol{\xi}_\circ) + \boldsymbol{DG}(\boldsymbol{\xi}_\circ)(\boldsymbol{\xi} - \boldsymbol{\xi}_\circ), \tag{1.24}$$

$$\hat{\boldsymbol{M}}(\boldsymbol{\xi}, \boldsymbol{\xi}_\circ) = \boldsymbol{M}(\boldsymbol{\xi}_\circ) + \boldsymbol{DM}(\boldsymbol{\xi}_\circ)(\boldsymbol{\xi} - \boldsymbol{\xi}_\circ), \tag{1.25}$$

where $\boldsymbol{DG}(\boldsymbol{\xi}_\circ)$ is the Jacobian of $\boldsymbol{G}$ evaluated at the point $\boldsymbol{\xi}_\circ$, and $\boldsymbol{DM}(\boldsymbol{\xi}_\circ)$ is the Jacobian of $\boldsymbol{M}$ evaluated at the point $\boldsymbol{\xi}_\circ$.

Replacing the Kalman filter equations with

$$\bar{\boldsymbol{\xi}}_j^p = \boldsymbol{G}(\bar{\boldsymbol{\xi}}_{j-1}^u), \tag{1.26}$$

$$\mathbf{P}_j = \boldsymbol{DG}(\bar{\boldsymbol{\xi}}_{\boldsymbol{j-1}}^{\boldsymbol{u}})\boldsymbol{U}_{j-1}\boldsymbol{DG}(\bar{\boldsymbol{\xi}}_{\boldsymbol{j-1}}^{\boldsymbol{u}})^T, \tag{1.27}$$

$$\boldsymbol{U}_j = \left(\boldsymbol{I} + \mathbf{P}_j\boldsymbol{DM}(\bar{\boldsymbol{\xi}}_j^p)^T\boldsymbol{R}^{-1}\boldsymbol{DM}(\bar{\boldsymbol{\xi}}_j^p)\right)^{-1}\mathbf{P}_j, \tag{1.28}$$

$$\bar{\boldsymbol{\xi}}_j^u = \bar{\boldsymbol{\xi}}_j^p + \boldsymbol{U}_j\boldsymbol{DM}(\bar{\boldsymbol{\xi}}_j^p)^T\boldsymbol{R}^{-1}(\boldsymbol{y}_j - \boldsymbol{M}(\bar{\boldsymbol{\xi}}_j^p)), \tag{1.29}$$

gives the *extended* Kalman filter (EKF) equations.

Since the EKF does not treat the nonlinear evolution of the PDF, it is of interest how quickly the exact PDF (if it were evolved with the full nonlinear model) would deviate from a normal distribution. The growth in the skewness and kurtosis of the distribution measure this tendency to deviate from normality, which gives a sense for the accuracy of the approximation made in (1.27). Appendix A treats this problem by considering the initial time evolution of the skewness and kurtosis of a Gaussian PDF evolving in a generic nonlinear model. The growth of the standard skewness and kurtosis measures is shown to be second order in time for short times. One method for roughly compensating for the nonlinear evolution of the covariance matrix is the method of multiplicative *variance inflation*, in which the predicted covariance matrix is inflated by a factor $\Omega^2 > 1$ [16, 12].

Although the EKF has solved (approximately) the problem of state estimation for nonlinear systems, it still must compute the inverse of at least one $N \times N$ matrix. When N numbers in the millions this is computationally infeasible. In addition, consider that with 8 bytes of precision per floating point number, simply storing $\mathbf{P}$ when $N = 10^6$ would require 4 terabytes (even after taking advantage of symmetry). These restrictions limit the applicability of the EKF.

1.4 Ensemble Kalman Filters

For a spatially extended system evolving according to a set of partial differential equations, the system state is usually represented as a collection of values

(for each variable of interest) on each grid point of a mesh. This collection of variables may number in the millions ($N \sim 10^6$). Often, the system investigated has many fewer dynamical degrees of freedom, in the sense that the dimension of the attractor is much less than N. One could conceivably take advantage of this fact by constructing a reduced rank representation of the covariance matrices $\boldsymbol{U}$ and $\mathbf{P}$.

The class of ensemble Kalman filters (EnKF) accomplish this through the representation of the PDF, not by its mean and covariance, but by an ensemble of system states. This ensemble gives a finite sampling approximate representation of the probability distribution function (PDF) of the system state. For an ensemble $\boldsymbol{\xi}^1$, $\boldsymbol{\xi}^2$, $\ldots$ $\boldsymbol{\xi}^k$ with k members, the PDF mean $\bar{\boldsymbol{\xi}}$ is

$$\bar{\boldsymbol{\xi}} = \frac{1}{k}\sum_{i=1}^{k} \boldsymbol{\xi}^i, \tag{1.30}$$

while the covariance $\boldsymbol{C}$ is given by

$$\boldsymbol{C} = \frac{1}{k-1}\boldsymbol{Z}\boldsymbol{Z}^T, \tag{1.31}$$

where the matrix $\boldsymbol{Z}$ has columns

$$\boldsymbol{Z} = \left[\delta\boldsymbol{\xi}^1 | \delta\boldsymbol{\xi}^2 | \ldots | \delta\boldsymbol{\xi}^k\right], \tag{1.32}$$

and $\delta\boldsymbol{\xi}^i$ are the ensemble perturbations

$$\delta\boldsymbol{\xi}^i = \boldsymbol{\xi}^i - \bar{\boldsymbol{\xi}}. \tag{1.33}$$

The EnKF approach is to approximate the PDF as lying in the space spanned by the k ensemble members [9, 34, 16, 14]. The number of ensemble members must then be large enough to account for the many dynamical degrees of freedom in the system,

but it need not be so large as to span the entire N dimensional space of possible states. The general procedure is to compute the *updated ensemble* $\{\boldsymbol{\xi}^{u,1} \dots \boldsymbol{\xi}^{u,k}\}$ from an update of the *predicted ensemble* $\{\boldsymbol{\xi}^{p,1} \dots \boldsymbol{\xi}^{p,k}\}$,

$$\begin{aligned} \text{update step} \quad &: \quad \{\boldsymbol{\xi}_j^{p,1} \dots \boldsymbol{\xi}_j^{p,k}\} + \\ &\qquad \{\text{measurements}\} \rightarrow \{\boldsymbol{\xi}_j^{u,1} \dots \boldsymbol{\xi}_j^{u,k}\} \qquad (1.34) \\ \text{predict step} \quad &: \quad \boldsymbol{\xi}_{j+1}^{p,i} = \boldsymbol{G}(\boldsymbol{\xi}_j^{u,i}) \quad i = 1 \dots k. \qquad (1.35) \end{aligned}$$

This iterative procedure begins with an initial predicted ensemble $\{\boldsymbol{\xi}_0^{p,1} \dots \boldsymbol{\xi}_0^{p,k}\}$ consisting of states randomly sampled from the system attractor. The maximum likelihood estimate of the system's state after an update step is the center of the updated ensemble given by (1.30). Here, the entire ensemble evolves nonlinearly, not just the mean as in equation (1.26) of the EKF. Furthermore, in the space spanned by the ensemble, only $k \times k$ matrices are required, rather than the $N \times N$ matrices of the EKF. Although the EnKF comes in many forms, they all approach the problem in this way. Here we follow a particular type of EnKF known as an ensemble square-root Kalman filter [14].

The predicted ensemble $\boldsymbol{\xi}^{p,i}$ has mean $\bar{\boldsymbol{\xi}}^p$ and covariance $\mathbf{P}$, defined as in (1.30) and (1.31). From this point on, all quantities are assumed to have a subscript j (we are performing the $t = t_j$ update step). We wish to find the updated ensemble $\boldsymbol{\xi}^{u,i}$ with mean $\bar{\boldsymbol{\xi}}^u$ and covariance $\boldsymbol{U}$, also defined as in (1.30) and (1.31). This update step is performed in the space of k-component vectors $\tilde{\boldsymbol{\xi}}$ which transform to the full state space via

$$\boldsymbol{\xi} = \bar{\boldsymbol{\xi}}^p + \boldsymbol{Z}^p \tilde{\boldsymbol{\xi}}, \qquad (1.36)$$

where $\boldsymbol{Z}^p$ is defined as in (1.32) for the predicted ensemble $\boldsymbol{\xi}^{p,i}$. In this space of $\tilde{\boldsymbol{\xi}}$ vectors, the predicted ensemble has mean zero and a covariance which is simply a multiple of the $k \times k$ identity matrix, $\tilde{\mathbf{P}} = (k-1)^{-1}\boldsymbol{I}$.

Each predicted ensemble member is projected into the observation space by forming the ensemble $\boldsymbol{y}^{p,i} = \boldsymbol{M}(\boldsymbol{\xi}^{p,i})$, using the full (possibly nonlinear) form of $\boldsymbol{M}$. The observation mean $\bar{\boldsymbol{y}}^p$ is defined similarly to (1.30). In addition, we define the matrix $\boldsymbol{Y}^p$, containing the ensemble perturbations, $\boldsymbol{Y}^p = \left[\delta\boldsymbol{y}^{p,1}|\delta\boldsymbol{y}^{p,2}|\ldots|\delta\boldsymbol{y}^{p,k}\right]$, where $\delta\boldsymbol{y}^{p,i} = \boldsymbol{y}^{p,i} - \bar{\boldsymbol{y}}^p$. $\boldsymbol{Y}^p$ can be considered as a linear mapping from k-component $\tilde{\boldsymbol{\xi}}$ vectors to s-component $\boldsymbol{y}$ vectors. By regarding $\boldsymbol{Y}^p$ as an observation operator of the new k-dimensional space, we effectively have linearized $\boldsymbol{M}$. This linearization is not the same as in the EKF equation (1.25). Rather, regarding $\boldsymbol{Y}^p$ as an observation operator effectively linearly interpolates between the full (possibly nonlinear) observations $\boldsymbol{y}^{p,i}$.

Although the predicted ensemble may not be Gaussian, we apply the standard Kalman filter update equations (1.22) and (1.23) by making the substitutions

$$\begin{aligned}
\bar{\boldsymbol{\xi}}^p &\rightarrow \bar{\tilde{\boldsymbol{\xi}}}^p = \mathbf{0}, \\
\mathbf{P} &\rightarrow \tilde{\mathbf{P}} = (k-1)^{-1}\boldsymbol{I}, \\
\boldsymbol{H} &\rightarrow \boldsymbol{Y}^p, \\
\boldsymbol{H}\bar{\boldsymbol{\xi}}^p &\rightarrow \bar{\boldsymbol{y}}^p.
\end{aligned}$$

Application of these substitutions to equations (1.22) and (1.23) results in the EnKF update equations for computing the updated covariance $\tilde{\boldsymbol{U}}$ and mean $\bar{\tilde{\boldsymbol{\xi}}}^u$.

$$\tilde{\boldsymbol{U}} = \left((k-1)\boldsymbol{I} + (\boldsymbol{Y}^p)^T\boldsymbol{R}^{-1}\boldsymbol{Y}^p\right)^{-1}, \tag{1.37}$$

$$\bar{\tilde{\boldsymbol{\xi}}}^u = \tilde{\boldsymbol{U}}(\boldsymbol{Y}^p)^T\boldsymbol{R}^{-1}(\boldsymbol{y}-\bar{\boldsymbol{y}}^p). \tag{1.38}$$

In principle, we could now compute the full state space mean and covariance

$$\bar{\boldsymbol{\xi}}^u = \bar{\boldsymbol{\xi}}^p + \boldsymbol{Z}^p\bar{\tilde{\boldsymbol{\xi}}}^u, \tag{1.39}$$

$$\boldsymbol{U} = \boldsymbol{Z}^p\tilde{\boldsymbol{U}}(\boldsymbol{Z}^p)^T. \tag{1.40}$$

However, it would be an inefficient to compute $\boldsymbol{U}$ directly; all that is required is to obtain the updated ensemble $\boldsymbol{\xi}^{u,i}$, and this can be obtained directly from $\tilde{\boldsymbol{U}}$ and $\bar{\boldsymbol{\xi}}^u$.

A Monte-Carlo method of obtaining the ensemble would be to randomly sample k points in the k-dimensional space according to a PDF with mean $\bar{\tilde{\boldsymbol{\xi}}}^u$ and covariance $\tilde{\boldsymbol{U}}$. These points could them be transformed into the state space using (1.36), forming the updated ensemble. However, it is generally beneficial if the choice of updated ensemble is deterministic. We seek a linear transformation from the predicted ensemble perturbations $\delta\boldsymbol{\xi}^{p,i}$ (equivalently, the matrix $\boldsymbol{Z}^p$) to the updated ensemble perturbations $\delta\boldsymbol{\xi}^{u,i}$ (equivalently, the matrix $\boldsymbol{Z}^u$) such that the covariance of the updated ensemble perturbations, as computed by (1.31), gives the required $\boldsymbol{U}$ of equation (1.40). The transformation is written $\boldsymbol{Z}^u = \boldsymbol{Z}^p\boldsymbol{W}$. Plugging this into (1.31) gives $\boldsymbol{U} = (k-1)^{-1}\boldsymbol{Z}^u(\boldsymbol{Z}^u)^T = (k-1)^{-1}\boldsymbol{Z}^p\boldsymbol{W}\boldsymbol{W}^T(\boldsymbol{Z}^p)^T$. Thus if $\boldsymbol{W}$ satisfies

$$\tilde{\boldsymbol{U}} = (k-1)^{-1}\boldsymbol{W}\boldsymbol{W}^T, \tag{1.41}$$

equation (1.40) will be satisfied. There are several $\boldsymbol{W}$ matrices which satisfy equation (1.41). However there is a unique real $\boldsymbol{W}$ which satisfies (1.41) *and* is symmetric; this is our choice of $\boldsymbol{W}$. It can be found numerically by computing the

Eigendecomposition of $\tilde{\boldsymbol{U}}$,

$$\tilde{\boldsymbol{U}} = \boldsymbol{V}\boldsymbol{D}\boldsymbol{V}^T, \tag{1.42}$$

leading to

$$\boldsymbol{W} = \sqrt{k-1}\boldsymbol{V}\boldsymbol{D}^{1/2}\boldsymbol{V}^T. \tag{1.43}$$

The final updated ensemble is

$$\boldsymbol{\xi}^{u,i} = \bar{\boldsymbol{\xi}}^u + \sum_{j=1}^{k} W_{ij}\delta\boldsymbol{\xi}^{p,j}, \tag{1.44}$$

where the W_{ij} are elements of the $\boldsymbol{W}$ matrix, and $\bar{\boldsymbol{\xi}}^u$ is given by (1.39). This step completes the EnKF update.

1.4.1 Parameter Estimation

There is a straightforward extension of the ensemble methods for cases in which some model parameters are unknown. Consider the model

$$\boldsymbol{\xi}_{j+1} = \boldsymbol{G}(\boldsymbol{\xi}_j, \boldsymbol{p}) \tag{1.45}$$

and the extended state space to vectors having the form $\boldsymbol{\gamma} = \begin{bmatrix} \boldsymbol{\xi} \\ \boldsymbol{p} \end{bmatrix}$, where $\boldsymbol{p}$, the vector of model parameters, is treated as a state variable. The extended model evolves as

$$\boldsymbol{\gamma}_{j+1} = \begin{bmatrix} \boldsymbol{\xi}_{j+1} \\ \boldsymbol{p}_{j+1} \end{bmatrix} = \begin{bmatrix} \boldsymbol{G}(\boldsymbol{\xi}_j, \boldsymbol{p}_j) \\ \boldsymbol{p}_j \end{bmatrix} = \hat{\boldsymbol{G}}(\boldsymbol{\gamma}_j). \tag{1.46}$$

Estimates of $\boldsymbol{\gamma}$ (and therefore the parameters $\boldsymbol{p}$) result from an implementation in the same way as for $\boldsymbol{\xi}$, but in the space of $\boldsymbol{\gamma}$ vectors.

1.4.2 Discussion

Although this form of EnKF has many advantages over the EKF, it may still be computationally infeasible for systems exhibiting high dimensional chaos. As the system size grows and the dynamical degrees of freedom increase, so too must the number of ensemble members k in order to sample the state space. This is a major drawback of ensemble methods like the EnKF, preventing their use for spatiotemporal chaos in large domains which would require an unfeasibly large k. In this case, the bottleneck in the computation may not be the EnKF update, but rather the simulation of k different system states. This is especially true when the model must simulate a system of partial differential equations, as in many spatiotemporally chaotic systems. This motivated the development of the LETKF of Chapter 2. The LETKF algorithm is presented in the next section in a context specific to Rayleigh-Bénard convection.

Chapter 2

Application of Data Assimilation to Rayleigh-Bénard Convection

The EnKF reduces the rank of covariance matrices by only keeping track of the PDF in the space spanned by the ensemble members. The LETKF reduces the rank further, by considering that, for spatiotemporal chaos with a small correlation length, the system state at any point is uncorrelated with the system state at points far away. For example, it is unnecessary to compute or store elements of covariance matrices corresponding to the temperature at two points far from one another (we can expect this element of the matrix to be approximately zero). Alternatively, one can consider that in spatiotemporally chaotic systems the dynamics in local regions tend to lie in a low dimensional space. To take advantage of this property of spatiotemporal chaos, the LETKF performs local updates on overlapping patches covering the domain. This is advantageous since the number of ensemble members required is independent of the system size, making the method applicable to large domains [10, 11]. Local regions may be spanned by fewer ensemble members, and thus the required k is smaller for the LETKF as compared to the EnKF. Other than this important difference, the LETKF operates similarly to the EnKF. The LETKF update uses the same equations as the EnKF, using an ensemble of system states to represent the PDF. The only difference being that the computations take place for many local ensembles, rather than one global ensemble. The full LETKF algorithm

is presented in Section 2.1.

Our goal is to determine the full fluid state of a Rayleigh-Bénard convection experiment, from a time series of shadowgraph measurements. We view this as a test case investigation of the general usefulness of the LETKF technique for laboratory experiments on spatiotemporal chaos. The fluid state $\boldsymbol{\xi}$ consists of the variables θ and $\mathbf{u}$ defined on the grid points (r_m, ϕ_n, z_l) of the cylindrical mesh; symbolically

$$\boldsymbol{\xi} = \begin{bmatrix} \theta \\ \\ \mathbf{u} \end{bmatrix}.$$

For the model $\boldsymbol{G}$ we simulate the Boussinesq equations (1.1). We assume that measurements are made at constant intervals Δt ($t_j \equiv j\Delta t$). In this context the measurements come as a collection of shadowgraph pixels, $\boldsymbol{y} = [I(x_1, y_1)\ I(x_2, y_2)\ \ldots\ I(x_s, y_s)]^{\mathrm{T}}$ where $I(x_l, y_l)$ is the light intensity at the location (x_l, y_l) of pixel l. Note that the location of these intensity measurements need not occur on a uniform mesh; we assume that their location is fixed but arbitrary. We assume for simplicity that $\boldsymbol{R} = \sigma^2 \boldsymbol{I}$, *i.e.*, a multiple of the identity matrix, so that measurement noise is homogeneous and uncorrelated with a standard deviation of σ. This assumption is justified for most experimental setups, as shown in Section 3.2. The map $\boldsymbol{M}(\boldsymbol{\xi})$ outputs the vector of pixel intensities $\boldsymbol{y}$ using a finite resolution approximation to (1.6), where for $\nabla_\perp^2$ we use a finite difference on the cylindrical mesh. Note that, since we require $\|a\nabla^2\bar{\theta}\| \ll 1$ for (1.6) to be a good approximation, $\boldsymbol{M}$ is only weakly nonlinear.

An application of any of the previously introduced data assimilation techniques (EKF, EnKF) to high aspect ratio Rayleigh-Bénard convection leads to enormous computation. Either inversion of an $N \times N$ matrix, or the requirement for a large

number of ensemble members make both methods infeasible. For example, we found for the Rayleigh-Bénard problem (with $\Gamma = 20$) that, using the EnKF, it was not computationally feasible to use large enough ensembles to obtain results of any use. For a small domain ($\Gamma = 6$ with $\epsilon = 2.0$) we found that the EnKF required $k \approx 100$ ensemble members. Since the dimensionality of Rayleigh-Bénard convection has been shown to be extensive [20], we expect on the order of $k \sim 1000$ ensemble members would be required for an aspect ratio $\Gamma = 20$.

2.1 The Local Ensemble Transform Kalman Filter

We now describe the LETKF's update step (1.34). This Appendix is an adaptation to our Rayleigh-Bénard problem of the technique developed in [12]. Let $\boldsymbol{\xi}_{mn}$ be a vector whose components consist of the collection of all elements of $\boldsymbol{\xi}$ (in any order) that lie on grid points within a horizontal distance L of the point (r_m, ϕ_n) of the mesh used by the model. We call $\boldsymbol{\xi}_{mn}$ a *local* state and L the local region radius. There are as many (overlapping) local regions as horizontal grid points (r_m, ϕ_n), see Fig. 2.1. Note that, since the problem of interest is essentially two dimensional, local regions are indexed by two indices (m, n). The three dimensional nature of the system is reflected in the fact that, for each horizontal grid point, the vector $\boldsymbol{\xi}_{mn}$ contains the state at all z levels z_l, $l = 1 \ldots N_z$. Associated with the updated and predicted (global) ensemble members $\boldsymbol{\xi}^{u,i}$ and $\boldsymbol{\xi}^{p,i}$ are the *local* ensemble members $\boldsymbol{\xi}^{u,i}_{mn}$ and $\boldsymbol{\xi}^{p,i}_{mn}$ (all local states, global states, and ensemble states have an implied time index j).

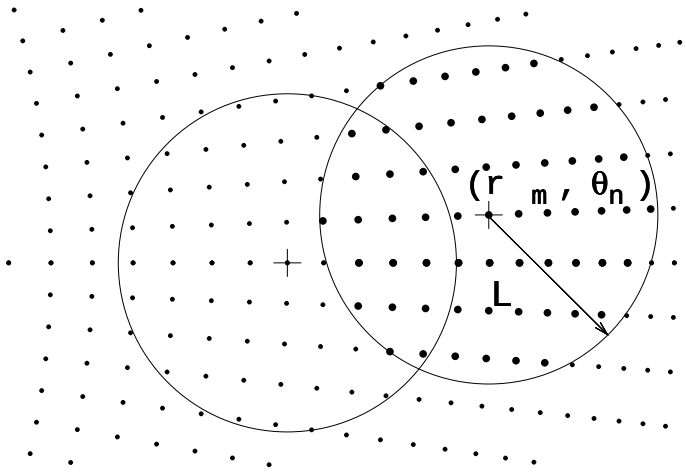

Figure 2.1: Two local regions are shown on a reduced resolution mesh. Every grid point (m, n) is the center of a local region. Associated with each local region (m, n) is the local state vector $\boldsymbol{\xi}_{mn}$ consisting of state variables on the indicated horizontal grid points and all vertical grid points associated with them.

Recal that the observation ensemble of predicted shadowgraphs $\{\boldsymbol{y}^{p,1} \ldots \boldsymbol{y}^{p,k}\}$ is defined as $\boldsymbol{y}^{p,i} = \boldsymbol{M}(\boldsymbol{\xi}^{p,i})$ (the projection of the predicted ensemble into the observation space). Let $\boldsymbol{y}^{p,i}_{mn}$ be all elements of $\boldsymbol{y}^{p,i}$ within the local region (m, n). If there are s_{mn} measurements made within the local region (m, n), then the vector $\boldsymbol{y}^{p,i}_{mn}$ has dimension s_{mn}. Form the matrix $\mathbf{Y}^{p}_{mn} \equiv [\delta\boldsymbol{y}^{p,1}_{mn} \mid \delta\boldsymbol{y}^{p,2}_{mn} \mid \cdots \mid \delta\boldsymbol{y}^{p,k}_{mn}]$ where $\delta\boldsymbol{y}^{p,i}_{mn} = \boldsymbol{y}^{p,i}_{mn} - \bar{\boldsymbol{y}}^{p}_{mn}$ and $\bar{\boldsymbol{y}}^{p}_{mn}$ is defined as in (1.30). The local measurements $\boldsymbol{y}_{mn}$ have an associated *local* $s_{mn} \times s_{mn}$ covariance matrix $\boldsymbol{R}_{mn}$, which is equal to σ^2 multiplied by the $s_{mn} \times s_{mn}$ identity matrix. We modify this matrix by forming the

tapered diagonal covariance matrix $\boldsymbol{Q}_{mn}$ having i, ith element

$$\boldsymbol{Q}_{mn}^{ii} \equiv [\sigma e^{(r/r_f)^2}]^2, \tag{2.1}$$

where r is the (horizontal) distance from the grid point (m, n) to the location of the ith element of $\boldsymbol{y}_{mn}$, and r_f is some falloff distance. This modification effectively weights measurements further from the grid point (m, n) less heavily when estimating the state of the (m, n) local region. This type of distance-dependant modification to the covariance matrices has been investigated previously [17]. The form (2.1) in particular is very effective for reducing the convergence time in our tests on Rayleigh-Bénard convection when compared to other forms (for example a linear function of r/r_f). We also weight current measurements more heavily than prior ones by the method of multiplicative variance inflation. The predicted covariance matrix is inflated by a factor $\Omega^2 > 1$, to lessen the influence of prior measurements on the current state, and to compensate in some rough way for model nonlinearities [16, 12]. Ordinarily Ω is chosen empirically.

We proceed to compute the *updated ensemble*. The following equations take place in the k-dimensional space of local predicted perturbations $\delta\boldsymbol{\xi}_{mn}^{p,i}$. The inputs are the global predicted ensemble $\boldsymbol{\xi}^{p,i}$ and the measurement $\boldsymbol{y}$. The output is the global updated ensemble $\boldsymbol{\xi}^{u,i}$.

Compute each $\boldsymbol{y}^{p,i} = \boldsymbol{M}(\boldsymbol{\xi}^{p,i})$.

For each grid point (m, n):

1. Form $\boldsymbol{y}_{mn}$ from the elements of the measurement $\boldsymbol{y}$, along with the tapered covariance matrix $\boldsymbol{Q}_{mn}$.

2. Form $\bar{\boldsymbol{y}}^p_{mn}$ and $\boldsymbol{Y}^p_{mn}$ from the ensemble $\boldsymbol{y}^{p,i}$.

3. Compute the updated $k \times k$ covariance matrix,

$$\tilde{\boldsymbol{U}}_{mn} = [(k-1)\Omega^{-2}\boldsymbol{I} + (\boldsymbol{Y}^p_{mn})^{\mathrm{T}}\boldsymbol{Q}^{-1}_{mn}\boldsymbol{Y}^p_{mn}]^{-1}. \tag{2.2}$$

4. Next compute the update vector

$$\boldsymbol{w}_{mn} = \tilde{\boldsymbol{U}}_{mn}(\boldsymbol{Y}^p_{mn})^{\mathrm{T}}\boldsymbol{Q}^{-1}_{mn}(\boldsymbol{y}_{mn} - \bar{\boldsymbol{y}}^p_{mn}), \tag{2.3}$$

   which is a transformation of the difference between the predicted and actual measurement into the k dimensional space of perturbations $\delta\boldsymbol{\xi}^{p,i}_{m,n}$.

5. Calculate the matrix

$$\boldsymbol{W}_{mn} = [(k-1)\tilde{\boldsymbol{U}}_{mn}]^{1/2} + \boldsymbol{w}_{mn}, \tag{2.4}$$

   where, by adding a vector to a matrix we mean adding it to each column of the matrix. The $1/2$ power here indicates taking a symmetric square root.

6. Form the local predicted ensemble $\{\boldsymbol{\xi}^{p,1}_{mn} \ldots \boldsymbol{\xi}^{p,k}_{mn}\}$ from the global predicted ensemble $\{\boldsymbol{\xi}^{p,1} \ldots \boldsymbol{\xi}^{p,k}\}$ as well as the matrix $\boldsymbol{Z}^p_{mn} \equiv [\delta\boldsymbol{\xi}^{p,1}_{mn} \mid \delta\boldsymbol{\xi}^{p,2}_{mn} \mid \cdots \mid \delta\boldsymbol{\xi}^{p,k}_{mn}]$.

7. Finally, compute the local updated ensemble perturbations $\delta\boldsymbol{\xi}^{u,i}_{mn}$,

$$\boldsymbol{Z}^u_{mn} = \boldsymbol{Z}^p_{mn}\boldsymbol{W}_{mn}. \tag{2.5}$$

As before, $\boldsymbol{Z}^u_{mn} \equiv [\delta\boldsymbol{\xi}^{u,1}_{mn} \mid \delta\boldsymbol{\xi}^{u,2}_{mn} \mid \cdots \mid \delta\boldsymbol{\xi}^{u,k}_{mn}]$, and the local updated ensemble is given by $\boldsymbol{\xi}^{u,i}_{mn} = \bar{\boldsymbol{\xi}}^{p}_{mn} + \delta\boldsymbol{\xi}^{u,i}_{mn}$.

To complete the update step, the *global* updated ensemble member $\boldsymbol{\xi}^{u,i}$ is obtained from the center elements of each $\boldsymbol{\xi}^{u,i}_{mn}$. by setting the value of $\boldsymbol{\xi}^{u,i}$ at each point (m, n) equal to the elements of $\boldsymbol{\xi}^{u,i}_{mn}$ corresponding to the center of local region (m, n) (*i.e.*, corresponding to the local state at grid point (m, n)). Note that each local region is assimilated independently, allowing for massive parallelization.

To estimate parameters, simply replace $\boldsymbol{\xi}$ with $\boldsymbol{\gamma}$ everywhere in the above steps. This formulation assumes state variables are spatially extended. Thus, when adding *global* parameters to the state space we must assume that they *are* spatially dependant. That is, when estimating both the Rayleigh number and a of (1.6) ($\boldsymbol{p} = [R \;\; a]^{\mathrm{T}}$), the state $\boldsymbol{\gamma}$ is the concatenation of $\boldsymbol{\xi}$ and $\hat{\boldsymbol{p}}$, where $\hat{\boldsymbol{p}} = [R_{11} \;\ldots\; R_{mn} \;\ldots\; a_{11} \;\ldots\; a_{mn} \;\ldots]^{\mathrm{T}}$. The LETKF is then augmented by averaging these parameter values over the grid, after the update step, to form global parameters. This average is performed for each global ensemble member $\boldsymbol{\gamma}^{u,i}$ by setting its $\hat{\boldsymbol{p}}$ component to $\hat{\boldsymbol{p}}^{u,i} = [\bar{R}^i \;\; \bar{R}^i \;\ldots\; \bar{a}^i \;\; \bar{a}^i \;\ldots]^{\mathrm{T}}$, where $\bar{R}^i$ and $\bar{a}^i$ are the ith ensemble members spatial averages of R and a, respectively. If the model allows for spatially dependent parameters then this last averaging step is not necessary.

2.2 Direct Insertion

In order to assess how well the LETKF method is performing, we will compare it to a more naive approach that we call Direct Insertion (DI). The DI approach is motivated by a style of synchronization used by Pecora and Carroll in [35] in which the available measurements simply substitute their corresponding state variables. This only applies to when state variables are measured directly. With shadowgraph measurements, no state variables are measured directly; however, there is a one to one correspondence between a shadowgraph and the vertically averaged field $\bar{\theta}(x, y)$. With this in mind, the DI update step adjusts the *predicted* $t = t_j$ temperature field $\bar{\theta}_j^p(x, y)$ to reflect the current measurement exactly.

At the time t_j of the shadowgraph measurement $I_j(x, y)$, the DI method updates the predicted temperature field $\theta_j^p(x, y, z)$ by adding a correction $\delta\theta_j(x, y, z)$ which is the unique field that is quadratic in z, matches the boundary conditions at $|z| = \frac{1}{2}$, and for which the updated field $\theta_j^u(x, y, z) = \theta_j^p(x, y, z) + \delta\theta_j(x, y, z)$ satisfies

$$I_j(x, y) = \frac{I_\circ(x, y)}{1 - a\nabla_\perp^2 \bar{\theta}_j^u(x, y)}. \tag{2.6}$$

This gives the update

$$\delta\theta_j(x, y, z) = (\bar{\theta}_j^u(x, y) - \bar{\theta}_j^p(x, y)) \left(\frac{3}{2} - 6z^2\right), \tag{2.7}$$

where $\bar{\theta}_j^u(x, y)$ is found by solving a Poisson equation,

$$\nabla^2 \bar{\theta}_j^u(x, y) = \frac{1}{a}\left[1 - \frac{I_\circ(x_c, y_c)}{I_j(x_c, y_c)}\right], \tag{2.8}$$

and (x_c, y_c) is the location of the closest pixel to (x, y) that is observed. Note that with DI the velocity is not updated, $\mathbf{u}_j^u(x, y, z) = \mathbf{u}_j^p(x, y, z)$, rather it develops

through coupling with the temperature during the simulation step,

$$\begin{bmatrix} \theta^p_{j+1}(x,y,z) \\ \mathbf{u}^p_{j+1}(x,y,z) \end{bmatrix} = \boldsymbol{G}\left(\begin{bmatrix} \theta^u_j(x,y,z) \\ \mathbf{u}^u_j(x,y,z) \end{bmatrix}\right).$$

The z-dependence of the predicted field is only slightly affected by the update since, if measurements are sufficiently frequent, the correction $\delta\theta_j(x,y,z)$ (which has quadratic dependence) is small. This method is the most successful data assimilation technique we have tested that does not use an update based on the Kalman Filter. It is meant to represent what one might try without knowledge of the localization techniques described in this section.

Chapter 3

Results

3.1 Perfect Model

In this section we describe so-called *perfect model* tests in which a time series of states, generated from a Boussinesq simulation ($\Gamma = 20$, $\epsilon = 1$, $Pr = 1$) of one particular initial condition, serves as a proxy for the experimental system. Simulated shadowgraph measurements of this time series are generated every $\Delta t = 1/4$ by using (1.6) with the parameters $a = 0.08$, $I_\circ(x, y) = 0.5$. By this technique we generate a situation in which the 'true state' to be estimated and the model used to estimate it both evolve under exactly the same dynamical rules. In Sec. 3.2 we use real (not simulated) observations of a physical system for which the model dynamics is surely not an exact description.

To reproduce the effects of measurement noise we add to each pixel a small random error that is an uncorrelated normally distributed number with mean zero and standard deviation σ. Measurements are made sparse by removing shadowgraph pixels, leaving only those which lie on *observation locations*. We introduce the measurement density $\rho \equiv s/(\pi\Gamma^2)$ as a measure of sparseness, where s is the number of observation locations. For $\rho \geq 4$ we randomly and uniformly distribute observation locations over the disk, otherwise the observation locations are placed on a Cartesian grid covering the disk (giving more repeatable results when using sparse

measurements). The observation locations are fixed for the entire data assimilation process.

We apply the LETKF and DI methods to our simulated shadowgraph time series to approximately reconstruct the original time series of true states. Performance is quantified via the temperature and mean flow RMS relative error,

$$E_\theta(t) = \sqrt{\frac{\langle|\theta(x,y,z,t) - \theta^t(x,y,z,t)|^2\rangle}{\langle|\theta^t(x,y,z,t)|^2\rangle}}, \tag{3.1}$$

$$E_{\bar{\mathbf{u}}}(t) = \sqrt{\frac{\langle|\bar{\mathbf{u}}(x,y,t) - \bar{\mathbf{u}}^t(x,y,t)|^2\rangle}{\langle|\bar{\mathbf{u}}^t(x,y,t)|^2\rangle}}, \tag{3.2}$$

where $\theta^t(x,y,z,t)$ and $\bar{\mathbf{u}}^t(x,y,t)$ are the temperature and mean flow from the 'true' time series of states, and $\langle\cdot\rangle$ indicates a spatial average.

Simulated shadowgraphs are assimilated at times t_j, $j = 1 \ldots J$. During this process we converge on an estimate of the system state (J chosen large enough to ensure convergence). At time t_J assimilation is turned off and the final updated state estimate is used as an initial condition for a long term forecast. We note that the initial state estimate does not attain the minimum error, instead it occurs about 1 t_v into the forecast. This is a result of the simulation rapidly balancing the fields by strongly suppressing field errors with large wave numbers. This effect is very slight in the LETKF forecasts, but can be quite strong in DI forecasts. Three measures of the quality of a state estimate are used: the minimum values attained by $E_\theta(t)$ and $E_{\bar{\mathbf{u}}}(t)$ during a forecast, denoted $E_\theta^{\min}$ and $E_{\bar{\mathbf{u}}}^{\min}$, and the *predictability time* τ, defined as the time when $E_\theta(t)$ first crosses the (somewhat arbitrary) value of 0.15. The perfect model tests reported here for the LETKF use $k = 18$ ensemble members, a variance inflation factor $\Omega = 1.0 - 1.1$, a local region radius $L = 2.6d$,

and a falloff distance $r_f = 1.4d$.

3.1.1 Performance with Noise/Sparseness

Here we document the performance of DI and the LETKF as a function of measurement noise σ and measurement density ρ. We define the *ideal* scenario as measuring a shadowgraph every $t_v/4$ with $\rho = 127$ (corresponding to a 451×451 shadowgraph image) and $\sigma = 0.01$ (this situation can be achieved in an experiment). Under these conditions the DI and LETKF (with $k = 18$ ensemble members) converge on a state estimate within $\sim t_v$ and $\sim 3t_v$, respectively (observing ~ 4 and ~ 12 shadowgraphs, respectively). Both DI and the LETKF are effective for estimation of the (unobserved) mean flow $\bar{\mathbf{u}}(x, y)$, however the LETKF achieves a minimum error $E^{\min}_{\bar{\mathbf{u}}}$ that is less than half that of DI. The forecast error for a typical state estimate is shown in Figs. 3.1 and 3.2. The general character of the forecasts is a shadowing of the true state, followed by rapid divergence. When divergence begins, the spatial structure of the error is concentrated near defects. This behavior is expected, as the magnitude of the Lyapunov vector associated with the largest Lyapunov exponent is largest at the location of defects [20].

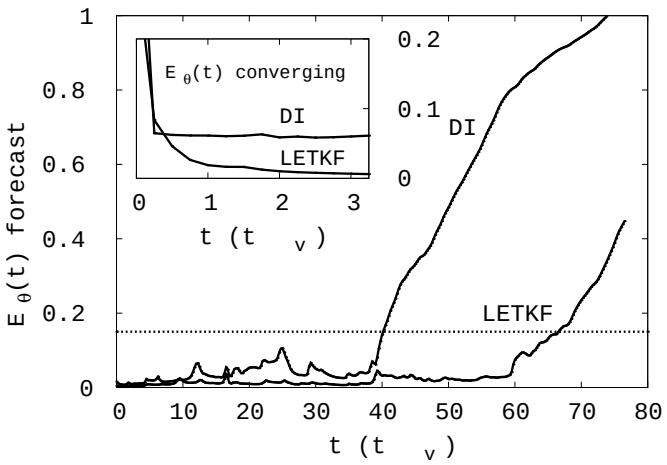

Figure 3.1: The error of the forecast temperature $E_\theta(t)$ with $\sigma = 0.01$ and $\rho = 127$. Also shown in the small graph is $E_\theta(t)$ as each method converges on a state. Assimilation is turned off at time $t_J = 3.25$ in the small graph, corresponding to time 0 in the large graph. The dashed line is our chosen threshold, $E_\theta(t) \leqslant 0.15$, below which we consider the forecasts 'good'.

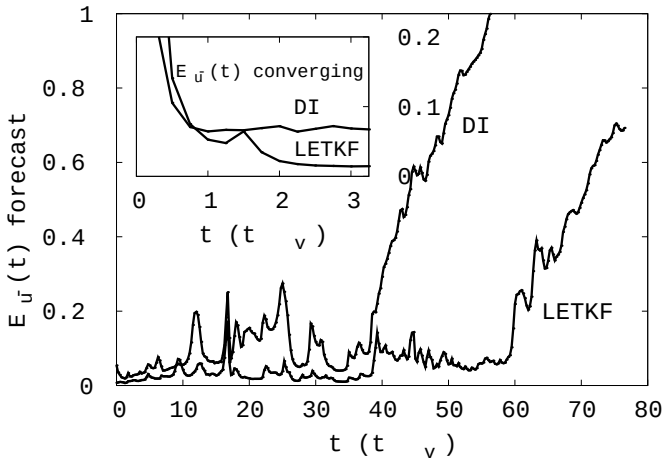

Figure 3.2: Mean flow error $E_{\bar{\mathbf{u}}}(t)$ of forecasts with $\sigma = 0.01$ and $\rho = 127$. Assimilation is turned off at time $t_J = 3.25$ in the small graph, corresponding to time 0 in the large graph. The insert shows $E_{\bar{\mathbf{u}}}(t)$ as each method converges on a state.

Under non-ideal conditions the LETKF proves much more robust than DI. Results for sparse measurements, shown in Fig. 3.3, demonstrate the large range of ρ for which the LETKF converges. One can observe the existence of a critical density of observations above which the LETKF does not substantially improve and below which it fails to converge. By adjusting the parameters of the LETKF's update step (as described in the Appendix) we have been able to push the critical density as low as $\rho = 1.3$ without a significant loss of quality in the state estimate. DI on the other hand exhibits a steady increase in $E_{\theta}^{\min}$ and $E_{\bar{\mathbf{u}}}^{\min}$ as ρ is decreased, as well as a rapidly deteriorating forecast when even a few observation locations are removed.

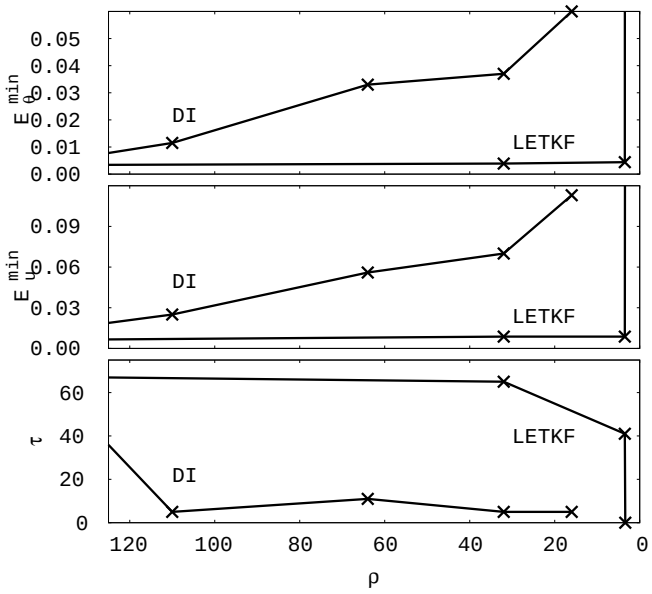

Figure 3.3: $E_\theta^{\min}$, $E_{\bar{\mathbf{u}}}^{\min}$, and the predictability time τ as the density of observations ρ is reduced.

Just as there is a critical measurement density, we have also found evidence of a critical measurement frequency. This frequency lies somewhere between 1 and 2 shadowgraph images per vertical diffusion time for repeatable convergence of the LETKF under ideal conditions. This corresponds to about 1 Hz in a typical experiment.

Since the shadowgraph signal is simply variations from the background intensity $I_\circ(x, y)$, the magnitude of measurement noise is best represented, not when compared with the typical shadowgraph magnitude, but when compared to the typical RMS intensity variation σ_{sg} of a shadowgraph. In other words, the meaningful *signal to noise ratio* is σ_{sg}/σ ($\sigma_{sg} \approx 0.12$ when $a = 0.08$ and $I_\circ(x, y) = 0.5$). DI relies on the Poisson solve (2.8) which is fundamentally insensitive to noise (it smoothes

the right hand side). However, this insensitivity competes with the sensitivity of the chaotic system dynamics when producing forecasts. The net result, in Fig. 3.4 indicates that DI forecasts are only useful for $\sigma \lesssim 0.4\sigma_{sg}$, whereas the LETKF operates up to and exceeding $\sigma = \sigma_{sg}$.

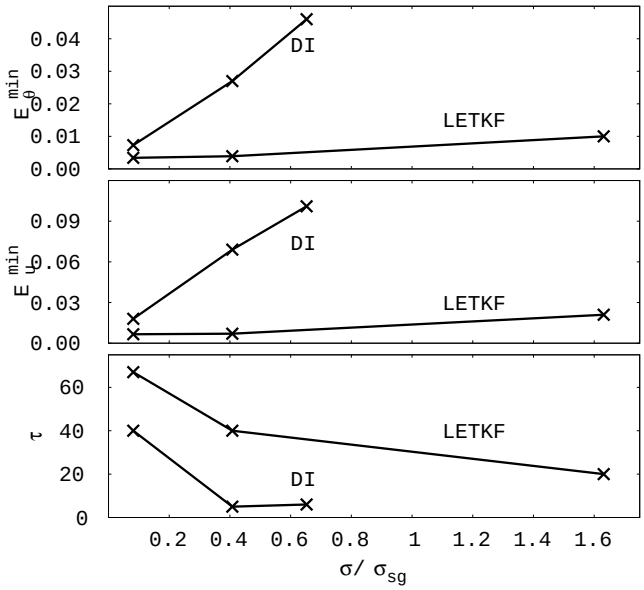

Figure 3.4: $E_\theta^{\min}$, $E_{\bar{\mathbf{u}}}^{\min}$, and the predictability time τ as measurement noise is increased.

We note that all results are from one particular realization of the possible 'true' time series, generated from one particular initial condition. These results are typical of what one can expect; however, variability can be expected (particularly in τ) for different data sets.

3.1.2 Parameter Estimation

The relevant parameters available for estimation include not only the model parameters Pr and R but also the observation operator parameter a of (1.6). In general, the LETKF facilitates estimation of observation operator parameters in exactly the same way as model parameters, by replacing $\boldsymbol{M}(\boldsymbol{\xi})$ by $\boldsymbol{M}(\boldsymbol{\xi}, \boldsymbol{p}) \equiv \hat{\boldsymbol{M}}(\boldsymbol{\gamma})$. The initial ensemble $\{\boldsymbol{\gamma}_0^{p,1} \ldots \boldsymbol{\gamma}_0^{p,k}\}$ is constructed as before, from states sampled from the attractor in the $\boldsymbol{\xi}$ component, while the $\boldsymbol{p}$ component is sampled from a normal distribution. When estimating a and R (with true values $a = 0.08$ and $R = 3414$) the initial distribution was given mean $(a = 0.07, R = 3073)$ and standard deviation $(\sigma_a = 0.02, \sigma_R = 683)$. The convergence process is demonstrated in Fig. 3.5.

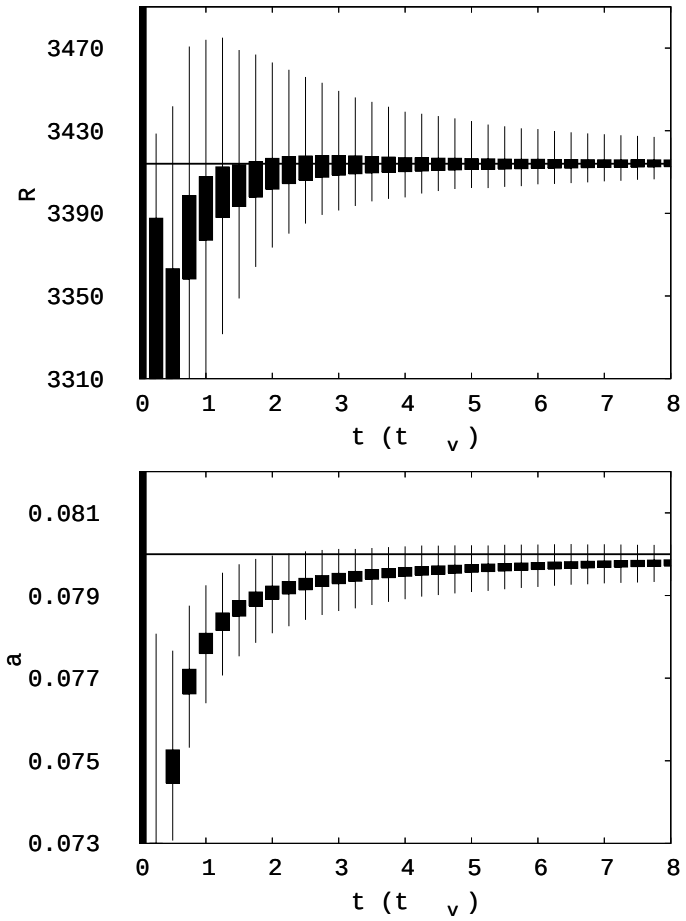

Figure 3.5: Simultaneously estimating the parameters a (with true value 0.08) and R (with true value 3414.0). The error bars give a visual representation of the ensemble spread, extending one standard deviation up and down. The thick error bars represent the case $\rho = 127$ and $\sigma = 0.01$, while the thinner represent the sparse measurement case, $\rho = 3.6$ and $\sigma = 0.01$.

Under ideal conditions the ensemble converges in $8t_v$ on $\boldsymbol{p} = [R \quad a]^{\mathrm{T}} = [3414.26 \;\; 0.07979]^{\mathrm{T}} \pm [1.61 \;\; 0.000072]^{\mathrm{T}}$, compared to the true value $\boldsymbol{p} = [3414.0 \;\; 0.08]^{\mathrm{T}}$. Here the error estimates for R and a are the standard deviations of the $\boldsymbol{p}$ component of the ensemble after the last update. Remarkably, even when measurements are

sparse ($\rho = 3.6$, near the critical measurement density) the parameter estimates are very good, $\boldsymbol{p} = [3416.71 \quad 0.07976]^{\mathrm{T}} \pm [9.9 \quad 0.00044]^{\mathrm{T}}$. When estimating the state and parameters simultaneously, the values of $E_{\theta}^{\min}$ and $E_{\bar{\mathbf{u}}}^{\min}$ are similar to those shown in Fig. 3.3 and 3.4. That is, the ability to estimate the system state is not adversely affected when parameters are simultaneously estimated. It is important to note that estimating parameters (in $\boldsymbol{\gamma}$ space) requires more ensemble members than when parameters are known, thus parameter estimation tests were performed with $k = 20$.

Due to limitations in our simulation, we were unable to estimate Pr in the full $\Gamma = 20$ system. Instead we estimated Pr, a, and R together in small aspect ratio tests ($\Gamma = 4$, $R = 8540$, $Pr = 1$). This small aspect ratio made possible the application of the EnKF, allowing for comparisons between the LETKF and the full EKF. Fig. 3.6 and 3.7 show the convergence of the ensemble toward the true parameter values. Both the EKF and LETKF assimilated data from simulated shadowgraphs ($\rho = 93$, $\sigma = 0.01$), and both achieve lower than 1% error in Pr parameter estimates.

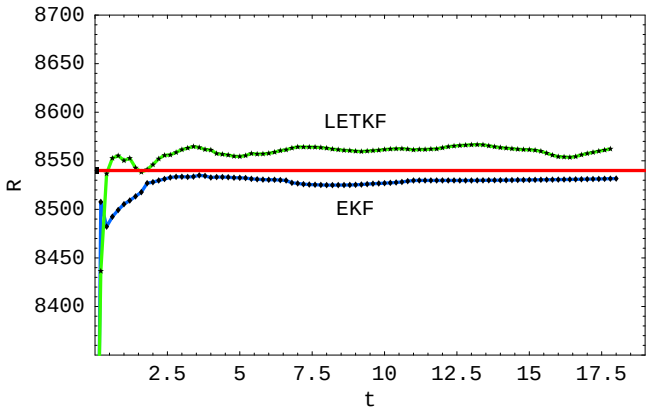

Figure 3.6: Convergence of the ensemble mean of the parameter R toward the true value, indicated by the red line. The initial ensemble had a large spread about the mean $R = 7857$.

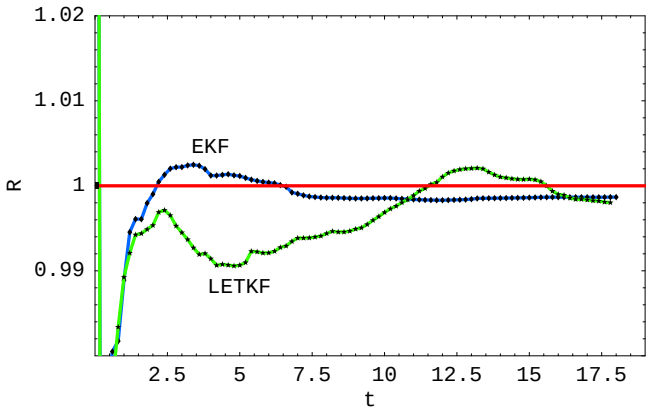

Figure 3.7: Convergence of the ensemble mean of the parameter Pr toward the true value, indicated by the red line. The initial ensemble had a large spread about the mean $Pr = 1.2$.

3.2 Experiment

3.2.1 Experimental Setup

The experiment differs from a perfect model scenario in that $\boldsymbol{G}$ and $\boldsymbol{M}$ are now approximations, requiring robustness to model error as well as observation operator error. In particular, the Boussinesq model is an approximation to the more exact Navier-Stokes equations and our geometric optics treatment is an approximation to a more involved physical optics treatment. For example, the Boussinesq equations do not treat the temperature dependence of the fluid viscosity, thermal expansion coefficient, specific heat (at constant pressure), or conductivity; each of which varies by 5% to 10% over the temperature range ΔT of the experiment.

The geometry, parameter values and boundary conditions are closely matched between experiments and simulations. For our experiments, the fluid is a thin ($d = 0.0602$ cm) layer of carbon dioxide gas compressed at a gauge pressure 31.58 bar. The layer is surrounded by a circular boundary of radius 1.25 cm. In the experiment, the top, bottom and lateral boundaries are composed of sapphire, aluminum and polyethersulfone, respectively; the thermal conductivities of the boundaries exceed that of the gas by at least an order of magnitude. For this fluid, the critical temperature difference for convection onset is $\Delta T = 6.02$ °C and $t_v = 1.66$ s. A fixed temperature difference $\Delta T = 10.23 \pm 0.09$ °C is imposed across the layer at a fixed mean temperature of 22.6 ± 0.1 °C. These conditions correspond to $R = 2902$ ($\epsilon = 0.7$), $Pr = 0.97$, and $\Gamma = 20.8$.

DI and the LETKF were used to assimilate shadowgraph images from the

experiment. Images were taken every $\Delta t = t_v/5$ (3.0 Hz) as 395×395 bitmaps ($\rho = 90$) having $\sigma_{sg} = 0.06$, a signal to noise ratio of approximately 20 ($\sigma/\sigma_{sg} \approx 0.05$).

In experiments, the true fluid state is not available for directly ascertaining the accuracy of state estimates. Instead, we generate a forecast of the state estimate, using the model, and compare the predicted shadowgraph sequence to subsequent measurements ($\boldsymbol{M}$ is applied to the forecast state every Δt). Shadowgraphs are first filtered by removing high frequency components (wavelengths less than $d/2$). We then threshold the image such that half the pixels are set to 1 (the remaining half are 0). This filtering/threshold procedure is applied to both the predicted and measured shadowgraph time series. The natural error measure is then the fraction of pixels incorrectly predicted, denoted E_I.

The results reported here using experimental data use an inflation factor of $\Omega \approx 1.4$. The large variance inflation is used to account for some of the model error, and greatly improves stability. In this section, in which we assimilate experimental data, the LETKF uses the parameter values $k = 18$, $L = 2.6d$, and $r_f = 1.4d$.

3.2.2 Analysis of Measurement Noise

Recall that the s component vector $\boldsymbol{\delta}$ represents measurement noise ($\boldsymbol{y}_j = \boldsymbol{M}(\boldsymbol{\xi}_j) + \boldsymbol{\delta}$). It is is a random variable which, in order to apply the Kalman filter methodology, is assumed to be normally distributed with mean 0. Two shadowgraph images ($I_\circ^{(1)}$ and $I_\circ^{(2)}$) were taken below onset ($\epsilon < 0$) and compared to estimate the distribution of noise in shadowgraph images. The the shadowgraph light intensity

at the location of pixel $[i,j]$ in each image is denoted $I_\circ^{(1)}[i,j]$ and $I_\circ^{(2)}[i,j]$, and the average is computed as $I_\circ^{avg} = (I_\circ^{(1)} + I_\circ^{(2)})/2$. The distribution of the quantity $\delta_{ij} = I_\circ^{(1)}[i,j] - I_\circ^{avg}[i,j]$ over the entire image is denoted $f(\delta_{ij})$. Fig. 3.8 shows the distribution $f(\delta_{ij})$ is symmetric and normally distributed with mean zero and standard deviation $\sigma \approx 0.003$. Thus the assumption made regarding the normality of measurement noise is a good approximation.

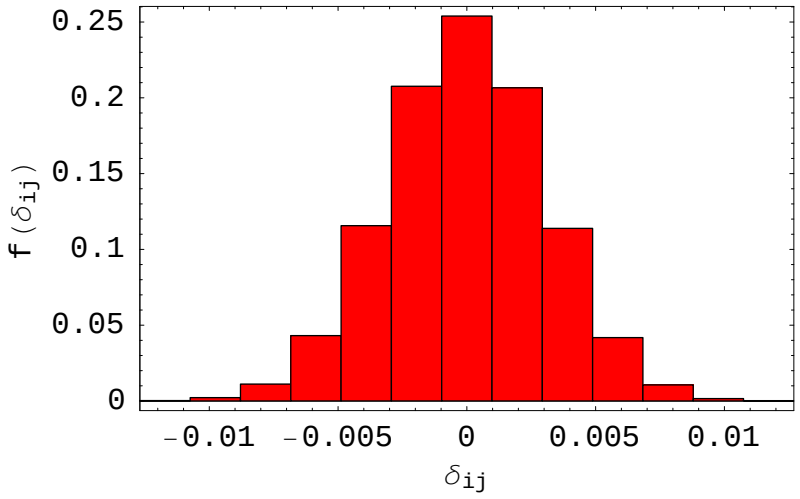

Figure 3.8: Probability distribution of shadowgraph pixel noise δ_{ij}.

The noise at each pixel is weakly correlated to noise at nearby pixels. This correlation can be measured via the quantity

$$C(m,n) \equiv \frac{\sum_{ij}\left(I_\circ^{(1)}[i+m,j+n] - I_\circ^{avg}[i+m,j+n]\right)\left(I_\circ^{(1)}[i,j] - I_\circ^{avg}[i,j]\right)}{\sum_{ij}\left(I_\circ^{(1)}[i,j] - I_\circ^{avg}[i,j]\right)^2}.$$

The one dimensional correlation function is denoted $C(n)$,

$$C(n) \equiv \frac{1}{4}\sum_{i^2+j^2=n^2} C(i,j). \tag{3.3}$$

Fig. 3.9 shows this correlation versus pixel distance.

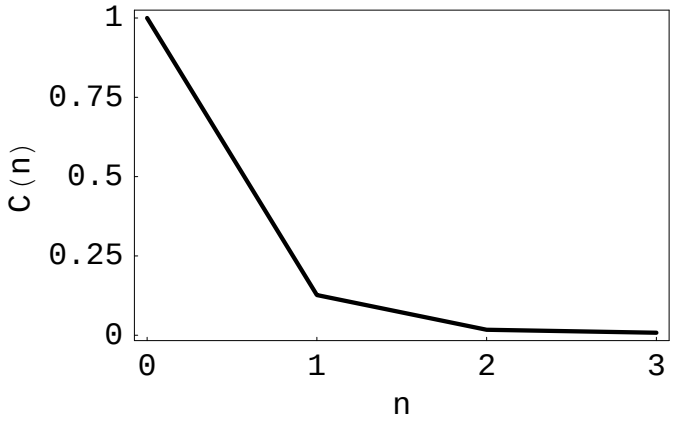

Figure 3.9: Correlation of shadowgraph pixel noise to the noise of nearby pixels.

There is a slight correlation between immediately adjacent pixels. Although we could build this slight correlation into the noise covariance matrix $\boldsymbol{R}$, Fig. 3.9 shows that the correlation is small. Thus we assume that pixel noise is independent and isotropic so that $\boldsymbol{R}$ is a multiple of the identity matrix. The full correlation $C(m, n)$ is plotted in Fig. 3.10. One can notice a slight asymmetry, the vertically adjacent pixels are more highly correlated than horizontally adjacent ones. Presumably this is specific to our shadowgraph apparatus.

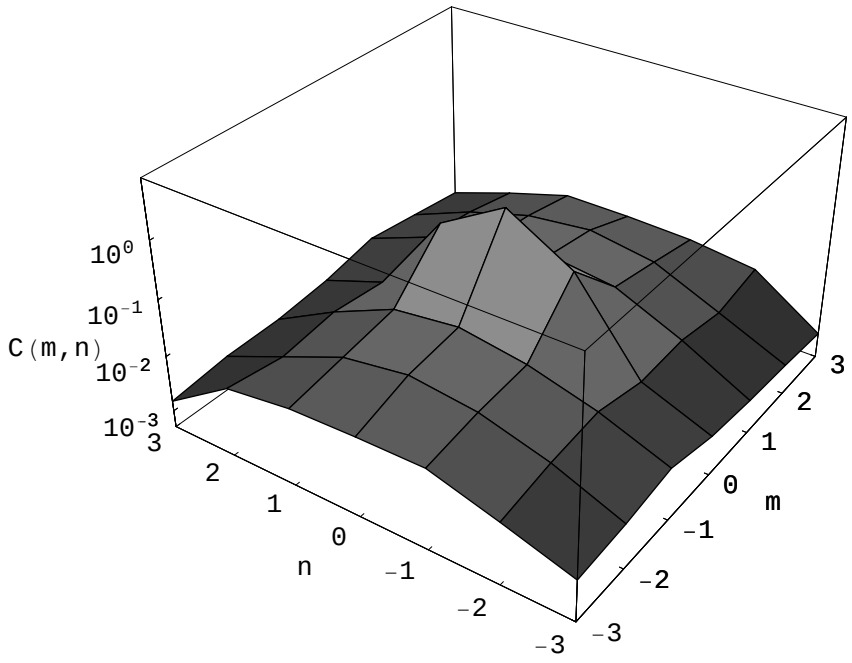

Figure 3.10: The correlation function $C(m, n)$ of shadowgraph measurement noise from the experiment.

The optimal value of σ for the LETKF update step was typically much larger than the measured value $\sigma = 0.003$. The best results were obtained with $\sigma \approx 0.01 - 0.03$, most likely due to the ability of an inflated σ to roughly compensate for some observation operator error.

3.2.3 Parameter Estimation and Performance with Sparseness

The LETKF is given $4t_v$ to converge on state and R estimates, this is sufficient for both ideal ($\rho = 90$) and sparse observation ($\rho = 4$) cases. In the ideal case, the LETKF converges on the parameter estimate $R = 2625$ (the experimen-

tally measured value is $R = 2902 \pm 26$). When $\rho = 4$ the LETKF converges on the estimate $R = 2491$. These estimates are obtained consistently throughout the experimental data set. Typical forecasts demonstrate a linear forecast error growth up to the saturation point near $E_I = 0.5$. Since R has been measured in the experiment, parameter estimation is not necessary. However, forcing the LETKF to use the measured R value harms the forecast, bringing it up to the level of the DI forecast. This indicates that the advantage of the LETKF in this case lies in its ability to estimate parameter values, as model error can typically be compensated for, to some extent, by adjustment of model parameters off their measured values.

An example of the resulting mean flow estimate is shown in Fig. 3.11. This data assimilation technique has allowed us to obtain (indirectly) the mean flow from shadowgraph measurements. Fig. 3.12 shows a typical state estimate from the LETKF. To the eye, DI state estimates look nearly identical to the LETKF estimates. However, DI forecasts shown in Fig. 3.13, which use the 'true' value of $R = 2902$ are significantly worse than LETKF forecasts, which use their respective R estimates.

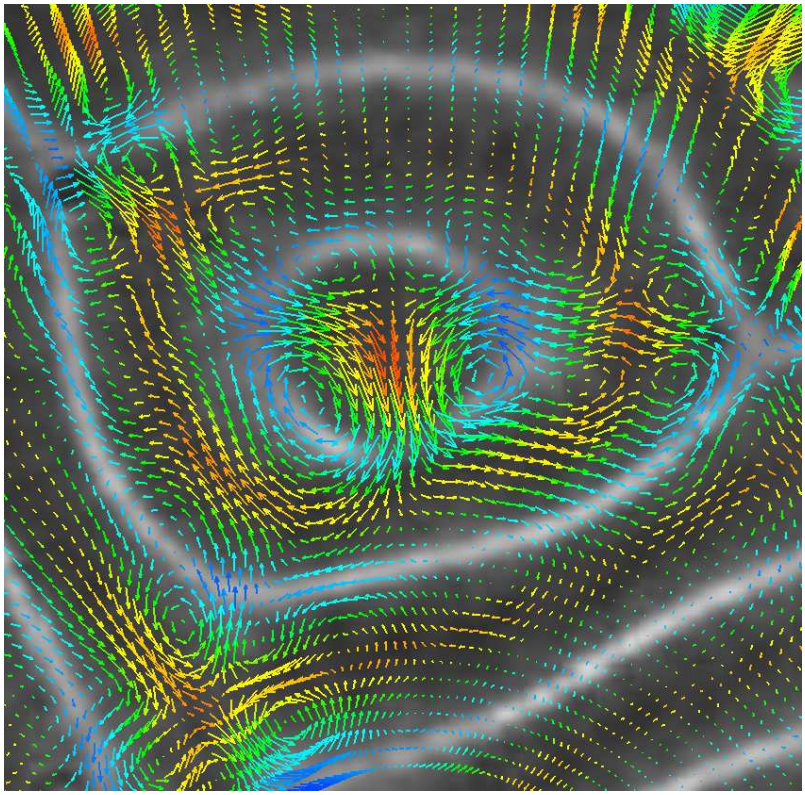

Figure 3.11: Close up image of the mean flow structure from the LETKF state estimate inferred from experimental data. The background shows the experimental shadowgraph image.

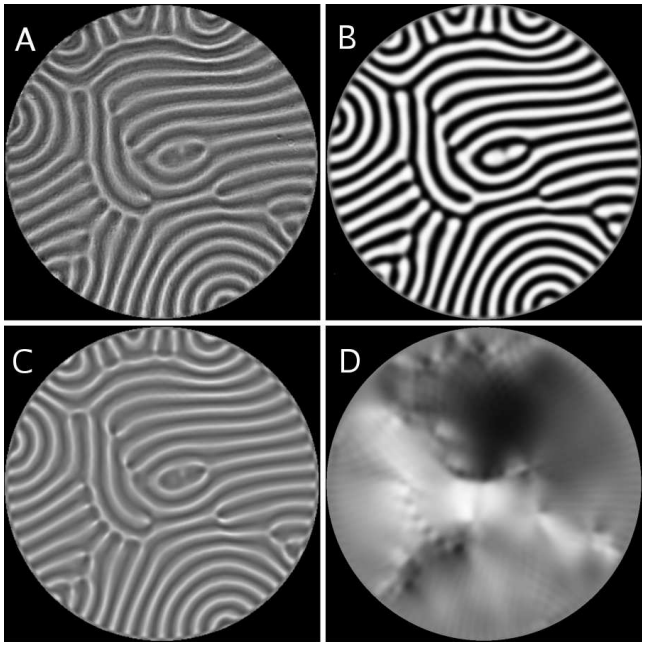

Figure 3.12: An estimate of the fluid state after assimilating for $4t_v$ of data ($J = 20$ frames). A: The $t = t_J$ shadowgraph measurement indicating columns of warm rising fluid (dark) and cold descending fluid (light). B: Temperature profile $\bar{\theta}(x, y)$ from the state estimate. C: The modeled shadowgraph $\boldsymbol{M}[\theta(x, y, z)]$ of the state estimate for comparison to A. D: The inferred vorticity potential $\phi(x, y)$ which solves $\nabla^2\phi(x, y) = -\hat{\boldsymbol{z}} \cdot (\nabla \times \bar{\boldsymbol{u}})$ and indicates regions of clockwise rotating (dark) and counter-clockwise rotating (light) mean flow.

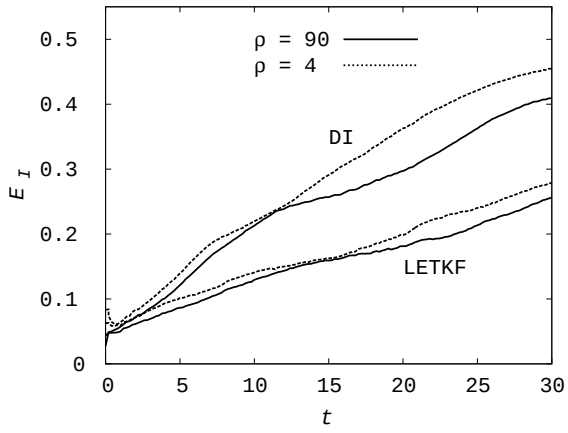

Figure 3.13: Forecast error E_I for DI and LETKF methods are shown for high and low measurement densities. The LETKF forecast uses its parameter estimate ($R = 2625$ for $\rho = 90$,$R = 2491$ for $\rho = 4$) while the DI forecast uses the measured value $R = 2902$.

Fig. 3.14 shows how the forecasts of Fig. 3.13 compare with typical perfect model forecasts (the best that can be expected) using the same parameters as the experiment ($R = 2902$, $\Gamma = 20.8$, $Pr = 0.97$) as well as the same measurement frequency ($\Delta t = t_v/5$), density ($\rho = 90$), and noise level ($\sigma/\sigma_{sg} \approx 0.05$). The experiment's forecast is unable to shadow the true state as seen in the perfect model case, likely due to model error.

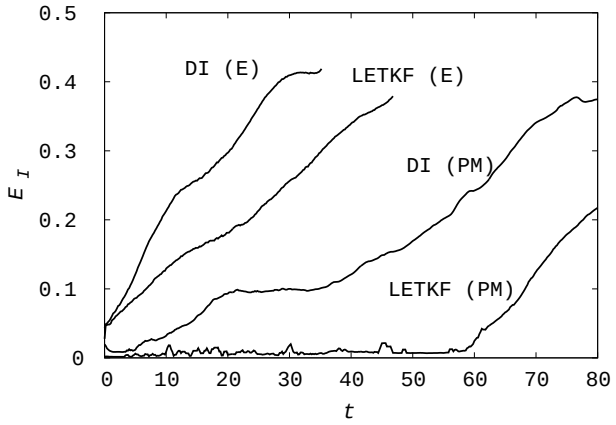

Figure 3.14: Forecast error E_I for DI and LETKF methods in perfect model (PM) tests and when using experimental data (E). The LETKF forecasts use the estimated value of R, while DI uses the true value.

3.3 Discussion

The results from applying the LETKF and DI methods to experimental data are far from the ideal results presented in the perfect model tests. There is significant model error. We have attempted to compensate for this model error by introducing a temperature dependence in the thermal conductivity and specific heat (each varies by about 5% over the temperature range in the experiment). However, we found that this did not improve forecasts. The model error may be a result of other assumptions made in the Boussinesq model. For example, that the velocity field is divergence free.

Recently it has been shown [36] that the *dimension density* $\delta_D = D/\Gamma^2$ (where D is the dimension of the full system) for spiral defect chaos is $D/\Gamma^2 \approx 0.25$ when

$\epsilon = 2.5$. This result was obtained in the same disk-shaped geometry we have investigated, with aspect ratios up to $\Gamma = 15$. This indicates that for our aspect ratio of $\Gamma = 20$, there is approximately $D = 100$ degrees of freedom (note that this is for $\epsilon = 2.5$ only; the dependence of dimension on ϵ remains unknown). The number of ensemble members will presumably scale with the number of dynamical degrees of freedom in a local region, which can be computed from this dimension density as $D_{local} = \delta_D L^2$. We used a local region radius of $L = 2.6d$ and a falloff distance of $r_f = 1.4d$ for the perfect model tests. For the experimental data, we found that a local region radius of $L = 2.6d$ and a falloff distance of $r_f = 1.0d$ worked well. In both cases, L is comparable to the correlation length of spiral defect chaos of $2.7d$ when $\epsilon = 0.7$ and $2.3d$ when $\epsilon = 1.0$ [37]. With these local region radii, local regions have (on average) only a few (1 or 2) degrees of freedom.

As the ensemble converges, it tends to confine itself to a space of dimension lower than k. The E dimension [38] D_E is a measure for the number of important directions in the space spanned by the ensemble perturbations. Roughly speaking, it gives the dimension of the space in which the ensemble is *spread out*. The E dimension is computed by forming the $N \times k$ matrix $\boldsymbol{Z}$ having the (global) ensemble perturbations as its columns. The real eigenvalues of the $k \times k$ positive semi-definite matrix $\boldsymbol{Z}^T\boldsymbol{Z}$, denoted σ_i^2 are used to compute the E dimension [38],

$$D_E \equiv \left(\sum_{i=1}^{k} \sigma_i\right)^2 \left(\sum_{i=1}^{k} \sigma_i^2\right)^{-1}. \tag{3.4}$$

Fig. 3.16 and 3.15 show the E dimension decreasing as the LETKF converges on the state and parameters. The update step generally increases the E dimension,

while the predict step generally decreases it. In perfect model tests the E dimension decreases to approximately $D_E \sim 5$, while when working with experimental data, it generally decreases to $D_E \sim 8$. This is consistent with the claim that local regions contain only a few degrees of freedom, and indicates that one could optimize by 'pruning' the ensemble size as it converges. All the results in sections 3.1 and 3.2 are for a constant $k = 18$ (or $k = 20$ when estimating parameters), but we have found that starting with $k = 18$ and reducing to $k = 8$ linearly within 10 measurement times gives similar results with a significant reduction in computation time. A large number of ensemble members ($k \approx 20$, as in the reported results of the previous sections) are required only for the first few assimilation steps. In addition, the strength of the model nonlinearities is largest when the ensemble spread is large (during the first few assimilation steps) thus one might begin assimilation with a large Ω and reduce it linearly to speed convergence. This procedure was found to be successful, but was not performed in the results reported here.

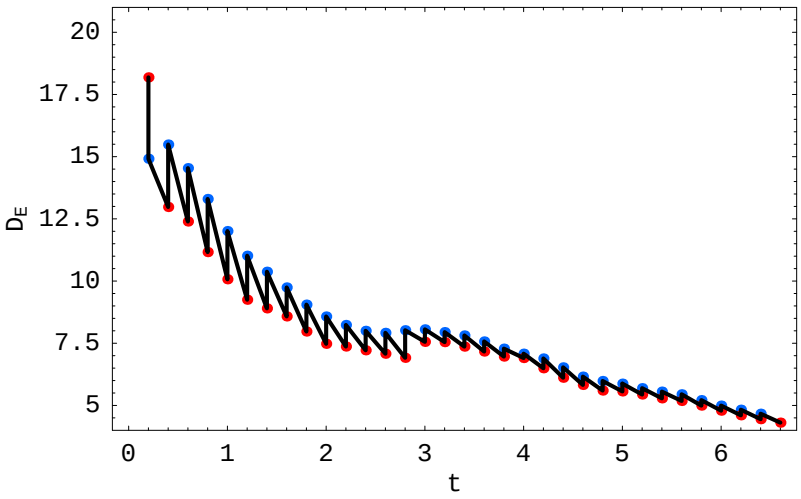

Figure 3.15: E dimension decreasing as the LETKF converges on perfect model data. Blue dots indicate the time just after an update step, while the red dots indicate the time just after the predict step. The ensemble has $k = 20$ ensemble members, and the measurements are ideal (in the sense described in section 3.1).

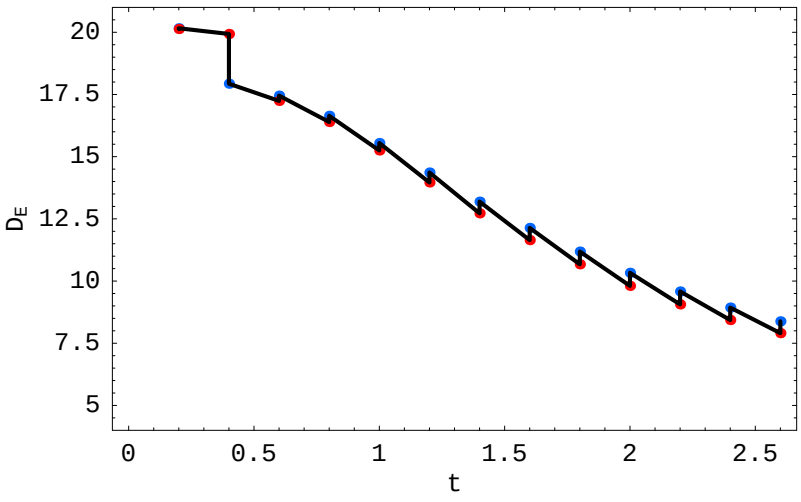

Figure 3.16: E dimension decreasing as the LETKF converges on experimental data. Blue dots indicate the time just after an update step, while the red dots indicate the time just after the predict step. The ensemble has $k = 22$ ensemble members in this example, and the measurements are at the highest measurement density (in the sense described in section 3.2).

In our model for incomplete measurements, observation locations are distributed uniformly. However, data may be incomplete due to large data voids in the shadowgraph time series. We have found that the LETKF can estimate the fluid state in these regions when the data voids have a characteristic radius not much larger than a correlation length. Fig. 3.17 shows a sequence of images of the midplane temperature estimate taken from the LETKF's assimilation of several experimental shadowgraph images having a large data void in the upper right.

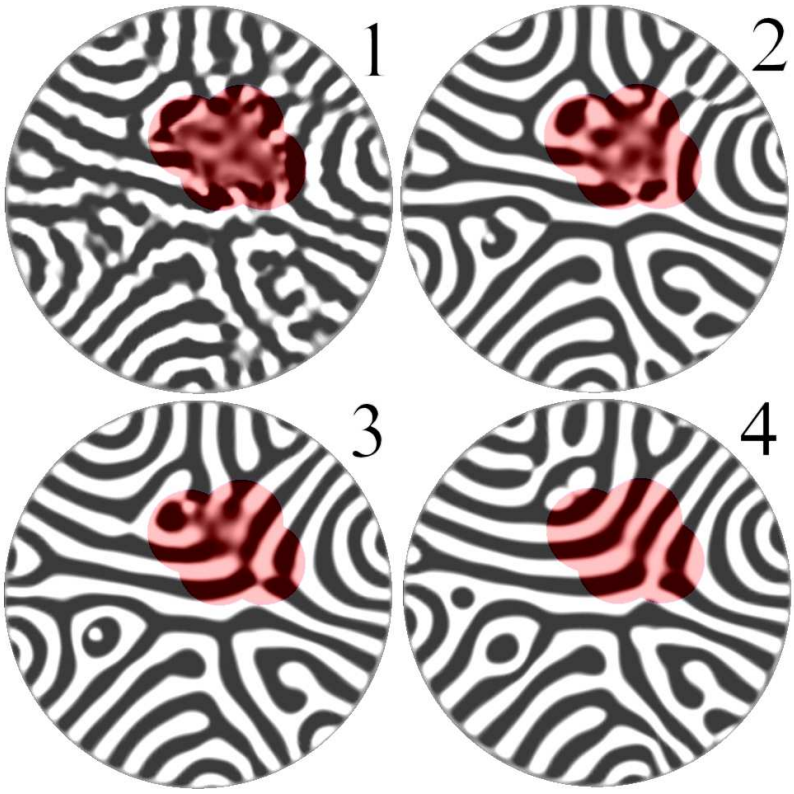

Figure 3.17: The midplane temperature field as the LETKF converges on an estimate of the system state using measurements which have a large data void. No measurements occur in the region with a red tint. The sequence of images occur at the times $t_j = t_1,\ t_3,\ t_{10},$ and t_{20}.

We have investigated two methods for estimating the fluid state in Rayleigh-Bénard convection experiments, DI and the LETKF. Both methods are effective for this purpose, with the LETKF outperforming DI both when using experimental data and in perfect model tests, especially when data is sparse/noisy. The LETKF is a promising technique for large experimental systems, as its complexity does not grow with the system size. In addition, it can take advantage of multiple processors, even if the model cannot, by parallelizing over the ensemble members during the

forecast step and over grid points during the update step. The LETKF method we have presented is potentially applicable to a large class of spatiotemporally chaotic laboratory experiments. Support for part I of this thesis we provided by National Science Foundation Grant 04-34193 and 04-34193 and the Office of Naval Research (Physics).

Part II

THE EFFECT OF ROTATION ON DYNAMO ACTION IN MAGNETOHYDRODYNAMIC TURBULENCE

Chapter 4

Introduction to Magnetohydrodynamics

Magnetohydrodynamics (MHD) is concerned with the study of conducting fluids (liquid metals or plasma), and the interaction between the fluid flow and electromagnetic fields. One motivation for the study of MHD is that planets and stars contain complex flows of molten metal or plasma. These flows are thought to be driven by convection, and may be responsible for the large scale magnetization of the atmosphere of stars and some planets such as the Earth. However, though the fundamental physics of MHD is understood, there is still much to learn about the dynamics of the flows, which are often chaotic and complex. For example, much research is focused on the question: Does an initial small magnetic field grow as a result of the flow? The answer to this question depends on the system investigated; if the answer is yes, the system is known as a *dynamo*.

The study of MHD via computer simulations is generally separated into two classes. In one case, the problem is simplified as much as possible to bring out the essential dynamics [39, 40, 41, 42, 43]. In these studies, to isolate the bulk dynamics from the effects of boundary conditions, periodic domains ($x, y, z \in [0, 2\pi]$) are employed. Rotation and convection are usually not included in favor of external forcing to drive the system. These studies investigate the role of turbulence and the conditions necessary for the generation of a dynamo in the simplest situations. The

other case involves complex simulations in which realistic boundary conditions are employed [44, 45, 46, 47]. These simulations generally include convection to drive the system and, in some cases, attempt to model the entire Earth. The study of MHD simulations (in both cases) is limited by the available resolution of computer models, which in turn is limited by available computing power.

There is a region between the two cases of complex, fully modeled flow and simple, idealized flow, which has not received as much attention as either extreme. It is the aim of this chapter to investigate one aspect of the MHD problem in this region which has not been addressed previously: the inclusion of the effects of rotation in an externally forced periodic domain. Investigation of this particular problem is interesting, as the effects of rotation may be isolated, providing insight into otherwise complex phenomena. There is some evidence that rotation plays a role in the ability of planets to generate a magnetic field. Venus, with a rotation rate 116 times slower than the Earth, has no measurable terrestrial magnetic field [48]. Mercury, with a rotation rate 176 times slower than earth, has a magnetic dipole moment about 1700 times weaker than Earth's [48]. We will focus on incompressible motion in which the fluid mass density is constant.

The dimensionless incompressible MHD equations describing the evolution of the velocity field $\mathbf{v}$ and magnetic field $\mathbf{B}$ take the form [49, 50]

$$\frac{\partial \mathbf{v}}{\partial t} + \mathbf{v} \cdot \boldsymbol{\nabla} \mathbf{v} = -\boldsymbol{\nabla} p + (\boldsymbol{\nabla} \times \mathbf{B}) \times \mathbf{B} + \nu \nabla^2 \mathbf{v} + \mathbf{F}, \tag{4.1}$$

$$\frac{\partial \mathbf{B}}{\partial t} + \mathbf{v} \cdot \boldsymbol{\nabla} \mathbf{B} = \mathbf{B} \cdot \boldsymbol{\nabla} \mathbf{v} + \eta \nabla^2 \mathbf{B}, \tag{4.2}$$

$$\boldsymbol{\nabla} \cdot \mathbf{v} = 0, \tag{4.3}$$

$$\boldsymbol{\nabla} \cdot \mathbf{B} \;=\; 0. \tag{4.4}$$

A constant external force $\mathbf{F}$ is present to drive the flow,

$$\mathbf{F} = \left[(\sin z + \cos y)\,\hat{\boldsymbol{x}} + (\sin x + \cos z)\,\hat{\boldsymbol{y}} + (\sin y + \cos x)\,\hat{\boldsymbol{z}}\right]. \tag{4.5}$$

All quantities above are dimensionless. Our simulations are done on a periodic domain in (x, y, z) where the periodicity length is 2π. Using overbars to denote dimensional quantities, we have that $(x, y, z) = (2\pi/\bar{L})(\bar{x}, \bar{y}, \bar{z})$ where $\bar{L}$ is the dimensional periodicity length of the system. Our dimensionless system with periodicity length 2π lends itself to the spectral decomposition of the fields described in Chapter 5 in which the allowed wave numbers in each coordinate direction are integer $k_{x,y,z} \in \mathbb{N}$. The dimensionless force as defined in equation (4.5) has a spatial RMS value of $\sqrt{3}$. This implies that velocities are normalized to $\bar{U} \equiv \sqrt{\bar{L}\bar{F}/(2\pi\sqrt{3}\bar{\rho})}$, (*i.e.*, $\mathbf{v} = \bar{\mathbf{v}}/\bar{U}$) where $\bar{F}$ is the spatial RMS of the dimensional applied force density and $\bar{\rho}$ is the mass density of the fluid (assumed constant in space and time). Times are in units of $\bar{L}/(2\pi\bar{U})$ (*i.e.* $t = 2\pi\bar{U}\bar{t}/\bar{L}$) and the magnetic field is normalized to $\sqrt{\bar{\rho}\bar{\mu}}\bar{U}$ (*i.e.*, $\mathbf{B} = \bar{\mathbf{B}}/(\bar{U}\sqrt{\bar{\rho}\bar{\mu}})$), where $\bar{\mu}$ is the magnetic permeability of the fluid. In these units, a normalized magnetic field $\mathbf{B}$ with magnitude $|\mathbf{B}| = 1$ represents a magnetic field for which the dimensional Alfvén wave velocity is $\bar{U}$; thus these units are termed Alfvénic units.

The first three equations (4.1), (4.2), and (4.3) are all that are necessary to simulate the flow, since if the initial $\mathbf{B}$ field is divergence free, equation (4.2) implies that $\mathbf{B}$ remains divergence free for all time. The dimensionless pressure p is found by taking the divergence of equation (4.1), imposing (4.3), and solving the Poisson-type

equation

$$\nabla^2 p = \boldsymbol{\nabla} \cdot \mathbf{F} - \boldsymbol{\nabla} \cdot (\mathbf{v} \cdot \boldsymbol{\nabla}\mathbf{v}) + \boldsymbol{\nabla} \cdot ((\boldsymbol{\nabla} \times \mathbf{B}) \times \mathbf{B}) \,. \tag{4.6}$$

The quantities $\nu = 2\pi\bar{\nu}/\bar{U}\bar{L}$ and $\eta = 2\pi\bar{\eta}/\bar{U}\bar{L}$ which appear in (4.1) and (4.2) are the dimensionless viscosity and magnetic diffusivity respectively; $\bar{\nu}$ and $\bar{\eta}$ are the dimensional viscosity and magnetic diffusivity respectively. The Reynolds number and magnetic Reynolds number are

$$R = \frac{\bar{L}\bar{U}_{\rm rms}}{\bar{\nu}} = \frac{2\pi U_{\rm rms}}{\nu} \text{ and} \tag{4.7}$$

$$R_m = \frac{\bar{L}\bar{U}_{\rm rms}}{\bar{\eta}} = \frac{2\pi U_{\rm rms}}{\eta}. \tag{4.8}$$

Here, $\bar{U}_{\rm rms}$ and $U_{\rm rms}$ are the space/time RMS average of the velocity field $\bar{\mathbf{v}}(\bar{\boldsymbol{x}}, \bar{t})$ and $\mathbf{v}(\boldsymbol{x}, t)$ respectively, $U_{\rm rms} = \bar{U}_{\rm rms}/\bar{U}$. Larger R (smaller viscosity) leads to smaller structure in the $\mathbf{v}$ flow and generally larger flow velocities. Similarly, larger R_m (lower Ohmic resistance) leads to smaller structure in the $\mathbf{B}$ field and less dissipation. The ratio $R_m/R = \nu/\eta$ is known as the magnetic Prandtl number Pr_m.

Dimensional analysis gives the viscous dissipative scale $\bar{\xi}_{\mathbf{v}} = \bar{\nu}^{3/4}/\bar{\epsilon}^{1/4}$ and Joule diffusive scale $\bar{\xi}_{\mathbf{B}} = \bar{\eta}^{3/4}/\bar{\epsilon}^{1/4}$, where $\bar{\epsilon}$ is the input power per unit mass [39]. These scales are the characteristic size of the smallest structures in the $\bar{\mathbf{v}}$ and $\bar{\mathbf{B}}$ field, respectively. The ratio of the viscous dissipative scale to the Joule diffusive scale is $\bar{\xi}_{\mathbf{v}}/\bar{\xi}_{\mathbf{B}} = (\bar{\nu}/\bar{\eta})^{3/4} = (\nu/\eta)^{3/4} = Pr_m^{3/4}$. For liquid metals the magnetic Prandtl number is very small [44] $Pr_m \sim 10^{-5} - 10^{-6}$, and thus structures in the fluid flow are much smaller than structures in the magnetic field. Such a large separation in scales means that a fully realistic simulation must employ a very dense mesh, capable of resolving the fluid flow while simultaneously being large enough to capture the large

spatial scales of the magnetic structure.

The forcing (4.5) is an oft studied form [43, 42, 51]. In the absence of a magnetic field, and if sufficiently weak, it generates a so-called ABC flow ($\mathbf{v}_{ABC} = \mathbf{F}/\nu$). This flow has as its only wave numbers $|k_x| = 1$, $|k_y| = 1$, and $|k_z| = 1$ and is known to generate chaotic particle trajectories. The ABC flow also possesses the special property that $\boldsymbol{\nabla} \cdot \mathbf{v}_{ABC} = 0$, $\boldsymbol{\nabla} \times \mathbf{v}_{ABC} = \mathbf{v}_{ABC}$, and thus $(\boldsymbol{\nabla} \times \mathbf{v}_{ABC}) \times \mathbf{v}_{ABC} = \mathbf{0}$. This flow has the maximum possible helicity for fixed kinetic energy, where helicity is defined as

$$\boldsymbol{H} \equiv \mathbf{v} \cdot (\boldsymbol{\nabla} \times \mathbf{v}). \tag{4.9}$$

Flow helicity is thought by some to be important for dynamo generation of magnetic fields [52]. For this ABC flow the helicity and energy density coincide. At sufficiently small ν, the ABC flow becomes unstable, and turbulent flows with time-dependence and higher wave number components result.

The dimensionless kinetic energy $E_{\mathbf{v}}$ and magnetic energy $E_{\mathbf{B}}$ in the periodic domain Γ are

$$E_{\mathbf{v}} = \int_{\Gamma} \frac{1}{2} |\mathbf{v}|^2 \mathrm{d}x^3, \tag{4.10}$$

$$E_{\mathbf{B}} = \int_{\Gamma} \frac{1}{2} |\mathbf{B}|^2 \mathrm{d}x^3. \tag{4.11}$$

Energy is injected by the external forcing $\mathbf{F}$ into the flow $\mathbf{v}$, after which it cascades to smaller scales and dissipates through viscous damping *or* is transferred to the $\mathbf{B}$ field. The energy in $\mathbf{B}$ in turn is damped through Ohmic dissipation.

4.1 The Kinematic Dynamo

We note that the system of equations (4.1)-(4.4) has a solution with the magnetic field identically equal to zero. In such a case the fluid velocity can (depending on ν) come to a turbulent, chaotic, periodic, or time-independent steady state. One can then ask whether this flow state is stable to the introduction of a small initial magnetic perturbation. If it is unstable, the initial perturbation will grow with time and is expected to eventually saturate in a nonlinear magnetized state. The problem of determining the stability of an initially unmagnetized flow to small magnetic perturbations is referred to as the kinematic dynamo problem.

The magnetic diffusivity is critical in determining whether a flow is a kinematic dynamo. For $\eta << 1$ the magnetic field is largely frozen into the fluid, stretching through differential flow in $\mathbf{v}$, while diffusion is unimportant in all but the smallest scales (this situation is conducive to dynamo action). For $\eta >> 1$ the magnetic field is highly dissipative, decaying toward $\mathbf{B} = 0$. Taking a dynamical systems perspective, for $\eta >> 1$ the system attractor lies in the $\mathbf{B} = 0$ plane. A blowout bifurcation occurs for a critical value of η at which the attractor expands into the full $\mathbf{v}$, $\mathbf{B}$ space [42]. In order to study the growth of a small initial $\mathbf{B}$ field, we $\mathbf{B}$-linearize equations (4.1) and (4.2) around $\mathbf{B} = 0$. Since the Lorentz term in equation (4.1) is second order in $\mathbf{B}$, we arrive at the standard Navier-Stokes equation,

$$\frac{\partial \mathbf{v}}{\partial t} + \mathbf{v} \cdot \boldsymbol{\nabla} \mathbf{v} = -\boldsymbol{\nabla} p + \nu \nabla^2 \mathbf{v} + \mathbf{F}. \tag{4.12}$$

In our $\mathbf{B}$-linearized situation, this equation is completely decoupled from the induction equation (4.2), which remains unchanged since every term is linear in $\mathbf{B}$. The

(simplified) *kinematic* MHD equations consist of (4.12), (4.2), and (4.3).

Because the velocity field now evolves according to equation (4.12), it takes all the usual properties common to standard unmagnetized fluids. In particular, it becomes turbulent for sufficiently small ν; if the fluid is not rotating, the energy spectrum is isotropic and follows the well known Kolmogorov spectrum $E_{\mathbf{v}} \sim k^{-5/3}$ for turbulence in the inertial range (the range where inertial forces dominate both viscous forces and the external force $\mathbf{F}$). Because $\mathbf{v}$ is time-dependant we cannot expect to find exactly time-exponential $\mathbf{B}$ solutions. However, we can still investigate the *average* growth or decay of $E_{\mathbf{B}}$.

4.2 Rotation

The effect of rotation on dynamo action was first investigated by Moffatt in [53, 54]. Here we investigate the effect of rotation in the kinematic case, in which the study of the velocity field reduces to the study of rotating fluids without regard to the magnetic field. This is advantageous because much literature already exists on rotating fluid turbulence [55, 56].

In a frame rotating with constant angular velocity $\mathbf{\Omega} = \Omega\hat{\boldsymbol{z}}$, the addition of the Coriolis and centrifugal forces modifies equation (4.12),

$$\frac{\partial \mathbf{v}}{\partial t} + \mathbf{v} \cdot \boldsymbol{\nabla}\mathbf{v} = -\boldsymbol{\nabla}P - 2\mathbf{\Omega} \times \mathbf{v} + \nu\nabla^2\mathbf{v} + \mathbf{F}. \tag{4.13}$$

The rotation rate $\mathbf{\Omega}$ is dimensionless and takes Alfvénic units, $\mathbf{\Omega} = \bar{\mathbf{\Omega}}\bar{L}/(2\pi\bar{U})$. Since the centrifugal force $-\mathbf{\Omega} \times (\mathbf{\Omega} \times \boldsymbol{r})$ can be written as a gradient of a scalar, it is incorporated into the new 'pressure' $P \equiv p - (1/2)|\mathbf{\Omega} \times \boldsymbol{r}|^2$. The addition of the

Coriolis force leads to two natural dimensionless numbers, the Rossby and Ekman numbers,

$$Ro \equiv \frac{\bar{U}_{\rm rms}}{2\bar{L}\bar{\Omega}} = \frac{U_{\rm rms}}{4\pi\Omega}, \tag{4.14}$$

$$Ek \equiv \frac{\bar{\nu}}{2\bar{L}^2\bar{\Omega}} = \frac{\nu}{8\pi^2\Omega} = \frac{Ro}{R}. \tag{4.15}$$

The Rossby number measures the relative magnitude of inertial forces to the Coriolis force, while the Ekman number measures the relative magnitude of viscous forces to the Coriolis force.

When $Ro \ll 1$ and $Ek \ll 1$ the fluid may be regarded as rapidly rotating. Rapidly rotating flows do not follow the Kolmogorov energy spectrum. Energy typically falls faster with wave number, $E_{\mathbf{v}} \sim k^{-2}$ [56]. In addition, the energy wave number spectrum is highly anisotropic, with much smaller energy in the k_z direction (along the axis of rotation). The Taylor-Proudman theorem states that, for the most rapidly rotating flows, this effect can be so strong that the fluid motion becomes essentially two dimensional, with derivatives in z approximately zero. To see how this happens, we note that $Ro \ll 1$ implies that, to a first approximation, the inertial terms in (4.13) are small compared to the Coriolis force, while $Ek \ll 1$ implies that the viscous force is similarly small. Thus, to a first approximation, we ignore all terms except the Coriolis force and the pressure, which in steady state must balance each other, $2\boldsymbol{\Omega} \times \mathbf{v} = -\boldsymbol{\nabla} P$. Removing the pressure by taking the curl gives $(\boldsymbol{\Omega} \cdot \boldsymbol{\nabla})\mathbf{v} = \Omega \frac{\partial \mathbf{v}}{\partial z} = 0$. Thus, $\mathbf{v}$ is approximately independent of z for large Ω. Two dimensional flows are known to exhibit an inverse energy cascade to larger scales than the scale at which energy is introduced [57].

Linearizing equation (4.13) about the state $\mathbf{v} = 0$ and taking a curl we obtain

$$\frac{\partial}{\partial t}(\boldsymbol{\nabla} \times \mathbf{v}) = 2\boldsymbol{\Omega} \cdot \boldsymbol{\nabla}\mathbf{v} + \nu \boldsymbol{\nabla} \times (\nabla^2 \mathbf{v}). \tag{4.16}$$

This equation supports traveling wave solutions known as *inertial* waves [54, 55]. Letting $\mathbf{v} = \mathbf{v}_\circ e^{i(\boldsymbol{k}\cdot\boldsymbol{r} - \omega t)}$ gives

$$(\boldsymbol{k} \times \mathbf{v}_\circ)\omega = 2i(\boldsymbol{\Omega} \cdot \boldsymbol{k})\mathbf{v}_\circ - i\nu k^2 (\boldsymbol{k} \times \mathbf{v}_\circ), \tag{4.17}$$

which leads to the dispersion relation $\omega = 2\Omega(k_z/k) - i\nu k^2$ and the condition $\mathbf{v}_\circ \cdot \boldsymbol{k} = 0$. This relation shows that inertial waves cannot have angular frequencies above 2Ω. The quality factor $Q \equiv Re(\omega)/(2Im(\omega))$ of these waves is given by

$$Q = \frac{k_z}{8\pi^2 k} \left(\frac{\nu}{2\lambda^2 \Omega}\right)^{-1}, \tag{4.18}$$

where $\lambda = 2\pi/k$. This expression shows that the wave with the highest Q factor has $k_x = k_y = 0$, $k_z = 1$. The factor $\left(\frac{\nu}{2\lambda^2\Omega}\right)$ is similar to the Ekman number (and exactly equal to it for the largest scale $\lambda = 2\pi$ waves). Equation 4.18 holds only in the bulk (far from boundaries). In bounded flows the quality factor is known to have a different dependence on Ek than derived here [58].

Chapter 5

Numerical Approach

5.1 Spectral Representation

The fields $\mathbf{v} = \mathrm{v}_x\hat{\boldsymbol{x}} + \mathrm{v}_y\hat{\boldsymbol{y}} + \mathrm{v}_z\hat{\boldsymbol{z}}$ and $\mathbf{B} = B_x\hat{\boldsymbol{x}} + B_y\hat{\boldsymbol{y}} + B_z\hat{\boldsymbol{z}}$ are expanded in Fourier series in which $k_x,\ k_y,\ k_z$ are integer,

$$\mathrm{v}_{x,y,z}(\boldsymbol{x}) = \sum_{k_x,k_y,k_z=-\infty}^{\infty} \mathrm{v}_{x,y,z}^{(\boldsymbol{k})} e^{i\boldsymbol{k}\cdot\boldsymbol{x}}, \tag{5.1}$$

$$B_{x,y,z}(\boldsymbol{x}) = \sum_{k_x,k_y,k_z=-\infty}^{\infty} B_{x,y,z}^{(\boldsymbol{k})} e^{i\boldsymbol{k}\cdot\boldsymbol{x}}, \tag{5.2}$$

$$\mathbf{v}^{(\boldsymbol{k})} = \mathrm{v}_x^{(\boldsymbol{k})}\hat{\boldsymbol{x}} + \mathrm{v}_y^{(\boldsymbol{k})}\hat{\boldsymbol{y}} + \mathrm{v}_z^{(\boldsymbol{k})}\hat{\boldsymbol{z}}, \tag{5.3}$$

$$\mathbf{B}^{(\boldsymbol{k})} = B_x^{(\boldsymbol{k})}\hat{\boldsymbol{x}} + B_y^{(\boldsymbol{k})}\hat{\boldsymbol{y}} + B_z^{(\boldsymbol{k})}\hat{\boldsymbol{z}}. \tag{5.4}$$

The fields $\mathbf{v}$ and $\mathbf{B}$ are real, thus the conditions $\mathrm{v}_{x,y,z}^{(-\boldsymbol{k})} = (\mathrm{v}_{x,y,z}^{(\boldsymbol{k})})^*$ and $B_{x,y,z}^{(-\boldsymbol{k})} = (B_{x,y,z}^{(\boldsymbol{k})})^*$ must hold, where $*$ is the complex conjugate operation. The condition $\mathrm{v}_{x,y,z}^{(\mathbf{0})} = 0$ is enforced, so that the fluid has no net momentum. We also require $\mathrm{B}_{x,y,z}^{(\mathbf{0})} = 0$ since the $\boldsymbol{k} = \mathbf{0}$ mode does not feel the effects of Ohmic dissipation ($\nabla^2\mathbf{B} = 0$ for this mode), and is thus unrealistic. For convenience we define the nonlinear terms

$$\boldsymbol{a} = \mathbf{v}\cdot\boldsymbol{\nabla}\mathbf{v}, \tag{5.5}$$

$$\boldsymbol{g} = \mathbf{B}\cdot\boldsymbol{\nabla}\mathbf{v}, \tag{5.6}$$

$$\boldsymbol{h} = \mathbf{v}\cdot\boldsymbol{\nabla}\mathbf{B}, \tag{5.7}$$

which have associated Fourier transforms $\boldsymbol{a}^{(\boldsymbol{k})}$, $\boldsymbol{g}^{(\boldsymbol{k})}$, and $\boldsymbol{h}^{(\boldsymbol{k})}$, defined similarly to equations (5.1 - 5.4). Taking the Fourier transform of the rotating kinematic MHD equations (4.13) and (4.2) we get the system of ordinary differential equations:

$$\frac{\mathrm{d}}{\mathrm{d}t}\mathbf{v}^{(\boldsymbol{k})} = -i\boldsymbol{k}P^{(\boldsymbol{k})} - \boldsymbol{a}^{(\boldsymbol{k})} - 2\boldsymbol{\Omega}\times\mathbf{v}^{(\boldsymbol{k})} - \nu k^2\mathbf{v}^{(\boldsymbol{k})} + \mathbf{F}^{(\boldsymbol{k})}, \tag{5.8}$$

$$\frac{\mathrm{d}}{\mathrm{d}t}\mathbf{B}^{(\boldsymbol{k})} = \boldsymbol{g}^{(\boldsymbol{k})} - \boldsymbol{h}^{(\boldsymbol{k})} - \eta k^2\mathbf{B}^{(\boldsymbol{k})}; \tag{5.9}$$

one set of equations for every discrete $\boldsymbol{k}$ vector. It is straight-forward to compute the pressure in spectral space,

$$P^{(\boldsymbol{k})} = k^{-2}\left(i\boldsymbol{k}\cdot\boldsymbol{a}^{(\boldsymbol{k})} - 2\boldsymbol{\Omega}\cdot(i\boldsymbol{k}\times\mathbf{v}^{(\boldsymbol{k})})\right). \tag{5.10}$$

In this representation, the fields $\mathbf{v}$, $\mathbf{B}$, $\boldsymbol{a}$, $\boldsymbol{g}$, $\boldsymbol{h}$ and P together represent the system state. Although $\mathbf{v}$ and $\mathbf{B}$ alone are enough to determine all these quantities, it is more convenient to think of all 6 fields collectively as the system state. The method used is pseudospectral, the nonlinear terms $\boldsymbol{a}$, $\boldsymbol{g}$, and $\boldsymbol{h}$ are computed in physical space, while all derivatives are computed in spectral space.

The Fourier space representation of all fields is truncated to include only wave numbers satisfying $|\boldsymbol{k}| < K$, reducing the problem to only the largest, most important scales. Truncating scales smaller than the viscous dissipative scale $K \sim 2\pi/\eta_{\mathbf{v}}$ has little effect of the dynamics, as the removed modes have negligible energy content. The sums in equation (5.1) and (5.2) then only sum over modes satisfying $|\boldsymbol{k}| < K$. The physical space representation of fields consists of values on a $N\times N\times N$ Cartesian grid.

5.2 Time Stepping

In this section we discretize the system in time, forming a map which takes the system state at the current and previous times, $t = t_j, t_{j-1}, t_{j-2} \ldots$, and outputs the system state at the next time $t = t_{j+1} = t_j + \delta t$. The state at the current time $t = t_j$ consists of $\mathbf{v}_j$, $\mathbf{B}_j$, $\boldsymbol{a}_j$, $\boldsymbol{g}_j$, $\boldsymbol{h}_j$, and P_j. We use a 3rd order semi-implicit method which mixes the explicit Adams-Bashforth method with the implicit Adams-Moulton method. For the system $\partial \boldsymbol{y}/\partial t = \boldsymbol{M}(\boldsymbol{y})$ the 3rd order Adams-Moulton method is

$$\boldsymbol{y}_{j+1} = \boldsymbol{y}_j + \delta t \left[(5/12)\boldsymbol{M}(\boldsymbol{y}_{j+1}) + (8/12)\boldsymbol{M}(\boldsymbol{y}_j) - (1/12)\boldsymbol{M}(\boldsymbol{y}_{j-1})\right], \tag{5.11}$$

while the 3rd order Adams-Bashforth method is given by

$$\boldsymbol{y}_{j+1} = \boldsymbol{y}_j + \delta t \left[(23/12)\boldsymbol{M}(\boldsymbol{y}_j) - (16/12)\boldsymbol{M}(\boldsymbol{y}_{j-1}) + (5/12)\boldsymbol{M}(\boldsymbol{y}_{j-2})\right]. \tag{5.12}$$

The Adams-Moulton method requires that $\boldsymbol{M}$ be inverted to solve for $\boldsymbol{y}_{j+1}$, hence it is used for the linear terms, while the Adams-Bashforth method is used for the nonlinear terms. For the system $\partial \boldsymbol{y}/\partial t = \boldsymbol{L}\boldsymbol{y} + \boldsymbol{N}\boldsymbol{L}(\boldsymbol{y})$ with linear term $\boldsymbol{L}\boldsymbol{y}$ and nonlinear term $\boldsymbol{N}\boldsymbol{L}(\boldsymbol{y})$ the mixed method is

$$\begin{aligned} \boldsymbol{y}_{j+1} \;=\; & (1 - \frac{5}{12}\delta t \boldsymbol{L})^{-1}\Big[(1 + \frac{8}{12}\delta t \boldsymbol{L})\boldsymbol{y}_j - \frac{1}{12}\delta t \boldsymbol{L}\boldsymbol{y}_{j-1} + \\ & \delta t\Big[\frac{23}{12}\boldsymbol{N}\boldsymbol{L}(\boldsymbol{y}_j) - \frac{16}{12}\boldsymbol{N}\boldsymbol{L}(\boldsymbol{y}_{j-1}) + \frac{5}{12}\boldsymbol{N}\boldsymbol{L}(\boldsymbol{y}_{j-2})\Big]\Big]. \end{aligned} \tag{5.13}$$

Although the induction equation (4.2) cannot produce divergence in the $\mathbf{B}$ field when solved exactly, all time stepping schemes (including implicit methods like the mixed method above) are unstable in this regard, and will generate a divergence. This instability is easy to overcome, by adding a *divergence cleaning* step after each

time step. Divergence cleaning can be accomplished in spectral space by subtracting the projection of $\mathbf{B}^{(\boldsymbol{k})}$ onto $\boldsymbol{k}$,

$$\mathbf{B}^{(\boldsymbol{k})} \to \mathbf{B}^{(\boldsymbol{k})} - \hat{\boldsymbol{k}}(\hat{\boldsymbol{k}} \cdot \mathbf{B}^{(\boldsymbol{k})}). \tag{5.14}$$

The final time stepping method takes all 6 fields and their Fourier transforms for the current and last two time steps, and outputs all fields and their Fourier transforms for the next time step:

$$\begin{aligned}
\text{Input} \quad : \quad & \mathbf{v}_j, \mathbf{B}_j, \boldsymbol{a}_j, \boldsymbol{g}_j, \boldsymbol{h}_j, P_j, \mathbf{v}_j^{(\boldsymbol{k})}, \mathbf{B}_j^{(\boldsymbol{k})}, \boldsymbol{a}_j^{(\boldsymbol{k})}, \boldsymbol{g}_j^{(\boldsymbol{k})}, \boldsymbol{h}_j^{(\boldsymbol{k})}, P_j^{(\boldsymbol{k})}, \\
& \mathbf{v}_{j-1}, \mathbf{B}_{j-1}, \boldsymbol{a}_{j-1}, \boldsymbol{g}_{j-1}, \boldsymbol{h}_{j-1}, P_{j-1}, \mathbf{v}_{j-1}^{(\boldsymbol{k})}, \mathbf{B}_{j-1}^{(\boldsymbol{k})}, \boldsymbol{a}_{j-1}^{(\boldsymbol{k})}, \boldsymbol{g}_{j-1}^{(\boldsymbol{k})}, \boldsymbol{h}_{j-1}^{(\boldsymbol{k})}, P_{j-1}^{(\boldsymbol{k})}, \\
& \mathbf{v}_{j-2}, \mathbf{B}_{j-2}, \boldsymbol{a}_{j-2}, \boldsymbol{g}_{j-2}, \boldsymbol{h}_{j-2}, P_{j-2}, \mathbf{v}_{j-2}^{(\boldsymbol{k})}, \mathbf{B}_{j-2}^{(\boldsymbol{k})}, \boldsymbol{a}_{j-2}^{(\boldsymbol{k})}, \boldsymbol{g}_{j-2}^{(\boldsymbol{k})}, \boldsymbol{h}_{j-2}^{(\boldsymbol{k})}, P_{j-2}^{(\boldsymbol{k})}. \\
\text{Output} \quad : \quad & \mathbf{v}_{j+1}, \mathbf{B}_{j+1}, \boldsymbol{a}_{j+1}, \boldsymbol{g}_{j+1}, \boldsymbol{h}_{j+1}, P_{j+1}, \mathbf{v}_{j+1}^{(\boldsymbol{k})}, \mathbf{B}_{j+1}^{(\boldsymbol{k})}, \boldsymbol{a}_{j+1}^{(\boldsymbol{k})}, \boldsymbol{g}_{j+1}^{(\boldsymbol{k})}, \boldsymbol{h}_{j+1}^{(\boldsymbol{k})}, P_{j+1}^{(\boldsymbol{k})}.
\end{aligned}$$

The following steps take place in the order they are written. Below, the notation $\mathbb{F}f(\boldsymbol{x})$ is used to indicate the Fourier transform of the function $f(\boldsymbol{x})$, while $\mathbb{F}^{-1}f(\boldsymbol{k})$ indicates the inverse transform.

$$\begin{aligned}
\text{Let } R_x^{(\boldsymbol{k})} \quad = \quad & (1 - \frac{8}{12}\delta t \nu k^2)(\mathrm{v}_x^{(\boldsymbol{k})})_j + \delta t \Big[\frac{1}{12}\nu k^2 (\mathrm{v}_x^{(\boldsymbol{k})})_{j-1} + \\
& 2\frac{8}{12}\Omega(\mathrm{v}_y^{(\boldsymbol{k})})_j - 2\frac{1}{12}\Omega(\mathrm{v}_y^{(\boldsymbol{k})})_{j-1} + \\
& \frac{23}{12}(-ik_x P_j^{(\boldsymbol{k})} - (a_x^{(\boldsymbol{k})})_j) - \frac{16}{12}(-ik_x P_{j-1}^{(\boldsymbol{k})} - (a_x^{(\boldsymbol{k})})_{j-1}) + \\
& \frac{5}{12}(-ik_x P_{j-2}^{(\boldsymbol{k})} - (a_x^{(\boldsymbol{k})})_{j-2}) + F_x \Big]. \\
\text{Let } R_y^{(\boldsymbol{k})} \quad = \quad & (1 - \frac{8}{12}\delta t \nu k^2)(\mathrm{v}_y^{(\boldsymbol{k})})_j + \delta t \Big[\frac{1}{12}\nu k^2 (\mathrm{v}_y^{(\boldsymbol{k})})_{j-1} - \\
& 2\frac{8}{12}\Omega(\mathrm{v}_x^{(\boldsymbol{k})})_j + 2\frac{1}{12}\Omega(\mathrm{v}_x^{(\boldsymbol{k})})_{j-1} + \\
& \frac{23}{12}(-ik_y P_j^{(\boldsymbol{k})} - (a_y^{(\boldsymbol{k})})_j) - \frac{16}{12}(-ik_y P_{j-1}^{(\boldsymbol{k})} - (a_y^{(\boldsymbol{k})})_{j-1}) +
\end{aligned}$$

$$\frac{5}{12}(-ik_y P^{(\boldsymbol{k})}_{j-2} - (a^{(\boldsymbol{k})}_y)_{j-2}) + F_y\Big].$$

$$\begin{aligned}
\text{Let } R^{(\boldsymbol{k})}_z &= (1 - \frac{8}{12}\delta t\nu k^2)(\mathrm{v}^{(\boldsymbol{k})}_z)_j + \delta t\Big[\frac{1}{12}\nu k^2(\mathrm{v}^{(\boldsymbol{k})}_z)_{j-1} + \\
&\quad \frac{23}{12}(-ik_z P^{(\boldsymbol{k})}_j - (a^{(\boldsymbol{k})}_z)_j) - \frac{16}{12}(-ik_z P^{(\boldsymbol{k})}_{j-1} - (a^{(\boldsymbol{k})}_z)_{j-1}) + \\
&\quad \frac{5}{12}(-ik_z P^{(\boldsymbol{k})}_{j-2} - (a^{(\boldsymbol{k})}_z)_{j-2}) + F_z\Big].
\end{aligned}$$

$$\text{Compute } (\mathrm{v}^{(\boldsymbol{k})}_x)_{j+1} = \frac{(1 + \frac{5}{12}\delta t\nu k^2)R^{(\boldsymbol{k})}_x + 2\frac{5}{12}\delta t\Omega R^{(\boldsymbol{k})}_y}{(1 + \frac{5}{12}\delta t\nu k^2)^2 + (2\frac{5}{12}\delta t\Omega)^2}. \tag{5.15}$$

$$\text{Compute } (\mathrm{v}^{(\boldsymbol{k})}_y)_{j+1} = \frac{(1 + \frac{5}{12}\delta t\nu k^2)R^{(\boldsymbol{k})}_y - 2\frac{5}{12}\delta t\Omega R^{(\boldsymbol{k})}_x}{(1 + \frac{5}{12}\delta t\nu k^2)^2 + (2\frac{5}{12}\delta t\Omega)^2}. \tag{5.16}$$

$$\text{Compute } (\mathrm{v}^{(\boldsymbol{k})}_z)_{j+1} = (1 + \frac{5}{12}\delta t\nu k^2)^{-1} R^{(\boldsymbol{k})}_z. \tag{5.17}$$

$$\begin{aligned}
\text{Compute } \mathbf{B}^{(\boldsymbol{k})}_{j+1} &= (1 + \frac{5}{12}\delta t\eta k^2)^{-1}\Bigg[(1 - \frac{8}{12}\delta t\eta k^2)\mathbf{B}^{(\boldsymbol{k})}_j + \\
&\quad \delta t\Big[\frac{1}{12}\eta k^2 \mathbf{B}^{(\boldsymbol{k})}_{j-1} + \frac{23}{12}(\boldsymbol{g}^{(\boldsymbol{k})}_j - \boldsymbol{h}^{(\boldsymbol{k})}_j) - \\
&\quad \frac{16}{12}(\boldsymbol{g}^{(\boldsymbol{k})}_{j-1} - \boldsymbol{h}^{(\boldsymbol{k})}_{j-1}) + \frac{5}{12}(\boldsymbol{g}^{(\boldsymbol{k})}_{j-2} - \boldsymbol{h}^{(\boldsymbol{k})}_{j-2})\Big]\Bigg].
\end{aligned} \tag{5.18}$$

$$\text{Assign } \mathbf{B}^{(\boldsymbol{k})}_{j+1} \rightarrow \mathbf{B}^{(\boldsymbol{k})}_{j+1} - \hat{\boldsymbol{k}}(\hat{\boldsymbol{k}} \cdot \mathbf{B}^{(\boldsymbol{k})}_{j+1}) \tag{5.19}$$

$$\text{Compute } \mathbf{v}_{j+1} = \mathbb{F}^{-1}\mathbf{v}^{(\boldsymbol{k})}_{j+1} \text{ and } \mathbf{B}_{j+1} = \mathbb{F}^{-1}\mathbf{B}^{(\boldsymbol{k})}_{j+1}. \tag{5.20}$$

$$\text{Let } J^{(\boldsymbol{k})}_{mn} = ik_m(\mathrm{v}^{(\boldsymbol{k})}_n)_{j+1} \quad \forall m, n \in \{x, y, z\}. \tag{5.21}$$

$$\text{Let } L^{(\boldsymbol{k})}_{mn} = ik_m(\mathrm{B}^{(\boldsymbol{k})}_n)_{j+1} \quad \forall m, n \in \{x, y, z\}. \tag{5.22}$$

$$\text{Compute } J_{mn} = \mathbb{F}^{-1}J^{(\boldsymbol{k})}_{mn} \text{ and } L_{mn} = \mathbb{F}^{-1}L^{(\boldsymbol{k})}_{mn} \quad \forall m, n \in \{x, y, z\}. \tag{5.23}$$

$$\text{Compute } (a_n)_{j+1} = \sum_{m \in \{x,y,z\}} (\mathrm{v}_m)_{j+1} L_{mn} \quad \forall n \in \{x, y, z\}. \tag{5.24}$$

$$\text{Compute } (g_n)_{j+1} = \sum_{m \in \{x,y,z\}} (B_m)_{j+1} L_{mn} \quad \forall n \in \{x, y, z\}. \tag{5.25}$$

$$\text{Compute } (h_n)_{j+1} = \sum_{m \in \{x,y,z\}} (\mathrm{v}_m)_{j+1} J_{mn} \quad \forall n \in \{x, y, z\}. \tag{5.26}$$

$$\text{Compute } \boldsymbol{a}^{(\boldsymbol{k})}_{j+1} = \mathbb{F}\boldsymbol{a}_{j+1}, \ \boldsymbol{g}^{(\boldsymbol{k})}_{j+1} = \mathbb{F}\boldsymbol{g}_{j+1}, \text{ and } \boldsymbol{h}^{(\boldsymbol{k})}_{j+1} = \mathbb{F}\boldsymbol{h}_{j+1}. \tag{5.27}$$

$$\text{Compute } P^{(\boldsymbol{k})}_{j+1} = k^{-2}\left(i\boldsymbol{k} \cdot \boldsymbol{a}^{(\boldsymbol{k})}_{j+1} - 2\boldsymbol{\Omega} \cdot (i\boldsymbol{k} \times \mathbf{v}^{(\boldsymbol{k})}_{j+1})\right). \tag{5.28}$$

$$\text{Compute } P_{j+1} \quad = \quad \mathbb{F}^{-1} P_{j+1}^{(\boldsymbol{k})}. \tag{5.29}$$

For small δt this system approximates the continuous equations. There are a total of 25 inverse Fourier transforms and 9 forward Fourier transforms, for a total of 34 transforms per time step. The transform in step (5.29) is not required, but is included for completeness. Each Fourier transform is accomplished by a fast Fourier transform (FFT) using a publicly available library [59] which takes advantage of the fact that the fields in physical space are real, speeding up transforms by a factor of roughly 2 over a complex calculation.

5.3 Parameters and Resolution Requirements

Ideally we wish to resolve all scales up to $\xi_{\mathbf{v}}$ and $\xi_{\mathbf{B}}$. However, in practice this is usually not necessary, as the energy content of modes drops quickly in k, even for scales larger than $\xi_{\mathbf{v}}$ or $\xi_{\mathbf{B}}$. The required K must be large enough to resolve the inertial range, but need not increase to the point where $\xi_{\mathbf{v}}$ is resolved. When the effects of rapid rotation are included, the resolution requirements drop further. By the Taylor-Proudman theorem, rapidly rotating flows do not require high resolution in the $\hat{\boldsymbol{z}}$ direction (the axis of rotation). However, although some speedup could be gained by exploiting these properties, a uniform resolution (N^3) grid was always employed. The highest possible resolved wave number is given by the Nyquist frequency $K = N/2$. However, in many studies involving the simulation of partial differential equations in a periodic cube, the relation $K = N/3$ is used to avoid aliasing issues. It was found that both cutoff wave numbers resulted in nearly

identical behavior for the runs performed, thus the condition $K = N/2$ was used for simplicity (and because most investigated resolutions were a power of 2).

We investigate the range $\nu \sim 10^{-1} - 10^{-2}$, $\eta \sim 10^{0} - 10^{-1}$, and rotation rates up to $\Omega = 8$. The inverse of ν appears in the Reynolds number. Thus, we typically refer to ν by its inverse (and similarly with η). In particular, the values $\nu^{-1} = 6.3$, 18, and 36 were used for most runs, for which the resolution was $N = 16$, 32, and 64, respectively. All three values of ν are small enough that without rotation the ABC flow $\mathbf{v}_{ABC}$ is unstable. The Reynolds numbers, Ekman numbers, and Rossby numbers of these flows will be computed from U_{rms} and discussed in Chapter 6.

In the dimensionless form employed, a time $\Delta t = 1$ is on the order of one *large eddy turnover time*, the characteristic time for the large scales in the flow to transit the domain. The most basic requirement for the time step is then $\delta t \ll 1$. To resolve the process of advection we must also have the standard Courant-Fredericks-Levy (CFL) condition $\delta t < \delta x / U_{\text{rms}} = 2\pi/(N U_{\text{rms}})$. Another requirement is that inertial waves with frequency 2Ω must be well resolved. The numerical method is 3^{rd} order in time, and thus the eventual time step is chosen at a point well within the region in which convergence follows a δt^{-3} law. Typically this results in a much smaller time step than the CFL condition requires. For example, most $\nu^{-1} = 18$ runs used $\delta t = 0.002$, while most $\nu^{-1} = 36$ runs used $\delta t = 0.0005$, about one order of magnitude smaller than the CFL condition requires and giving at least 500 time steps per period ($\tau = 2\pi/\Omega$) for the fastest rotation rate ($\Omega = 8$).

Chapter 6

Simulation Results

Simulations of the fluid flow velocity $\mathbf{v}$ begin with the initial condition $\mathbf{v}(x, y, z, 0) = \mathbf{0}$ and evolve for many large eddy turnover times (typically to $t = 400 \equiv T$). When calculating time averages, the evolution up to the time $t = 100 \equiv t_\circ$ is disregarded to ensure that transient effects are no longer present and that the dynamics reflect motion on the attractor. The investigated rotation rates are $\Omega = 0,\ 0.5,\ 1,\ 2,\ 4,\ 6,\ 8$. The notation

$$\langle \star \rangle = \sqrt{\frac{1}{(2\pi)^3} \int_\Gamma |\star|^2 \mathrm{d}x\mathrm{d}y\mathrm{d}z} \tag{6.1}$$

is used for the spatial RMS average of a scalar or vector quantity $\star$; and the notation

$$\langle\langle \star \rangle\rangle = \frac{1}{T - t_\circ} \int_{t_\circ}^{T} \langle \star \rangle \mathrm{d}t \tag{6.2}$$

is used for averages over space and time.

The average RMS velocity $U_{\mathrm{rms}} = \langle\langle \mathbf{v} \rangle\rangle$ is shown for $\nu^{-1} = 36$, $\nu^{-1} = 18$, and $\nu^{-1} = 6.3$ in Tables 6.1, 6.2, and 6.3, respectively. This average velocity is used to compute the Reynolds number, Rossby number, and Ekman number. The largest investigated Reynolds number is $R \approx 4 \times 10^3$.

Ω	0	1	2	4	6	8
U_{rms}	4.63	5.28	5.55	8.58	12.89	16.78
R	1048	1194	1256	1941	2916	3796
Ro $(\times 10^{-1})$	∞	7.37	4.20	2.21	3.42	3.36
Ek $(\times 10^{-4})$	∞	6.17	3.34	1.14	1.17	0.89

Table 6.1: U_{rms}, Reynolds number R, Rossby number Ro, and Ekman number Ek for $\nu^{-1} = 36$ and various rotation rates.

Ω	0	0.5	1	2	4	6	8
U_{rms}	4.57	4.48	4.70	6.17	9.76	13.01	15.47
R	517	506	532	698	1104	1471	1750
Ro $(\times 10^{-1})$	∞	7.13	3.74	2.45	1.94	1.72	1.53
Ek $(\times 10^{-4})$	∞	14.1	7.03	3.52	1.76	1.17	0.880

Table 6.2: U_{rms}, Reynolds number R, Rossby number Ro, and Ekman number Ek for $\nu^{-1} = 18$ and various rotation rates.

Ω	0	0.5	1	2	4	6	8
U_{rms}	5.53	5.12	5.45	6.35	8.10	8.90	8.90
R	219	203	216	251	321	352	352
Ro ($\times 10^{-1}$)	∞	8.15	4.34	2.53	1.61	1.18	0.89
Ek ($\times 10^{-4}$)	∞	40.2	20.1	10.0	5.03	3.35	2.51

Table 6.3: U_{rms}, Reynolds number R, Rossby number Ro, and Ekman number Ek for $\nu^{-1} = 6.3$ and various rotation rates.

One can see that the conditions for rapid rotation ($Ek \ll 1$, $Ro \ll 1$) are satisfied for these flows. Equation (4.18), derived in section 4.2 shows that the quality factor for inertial waves goes like Ek^{-1}. Thus, for the investigated rotation rates, especially those for which $Ek \sim 10^{-4}$, we can expect to see inertial waves lasting for long times.

6.1 Flow Characterization

Each simulation stores a time series of the average helicity $\langle \boldsymbol{H} \rangle$, input power $\langle \mathbf{F} \cdot \mathbf{v} \rangle$, inertia $\langle \mathbf{v} \cdot \boldsymbol{\nabla} \mathbf{v} \rangle$, Coriolis force $\langle 2\boldsymbol{\Omega} \times \mathbf{v} \rangle$, viscous force $\langle \nu \nabla^2 \mathbf{v} \rangle$, pressure force $\langle \boldsymbol{\nabla} P \rangle$, as well as the energy $E_{\mathbf{v}}$, and $E_{\mathbf{B}}$. Fig. 6.1 shows the time series of four force strengths from equation (4.13) for various rotation rates. Fig. 6.2 shows time series of the average helicity, velocity, and external power input. All quantities exhibit a chaotic time evolution.

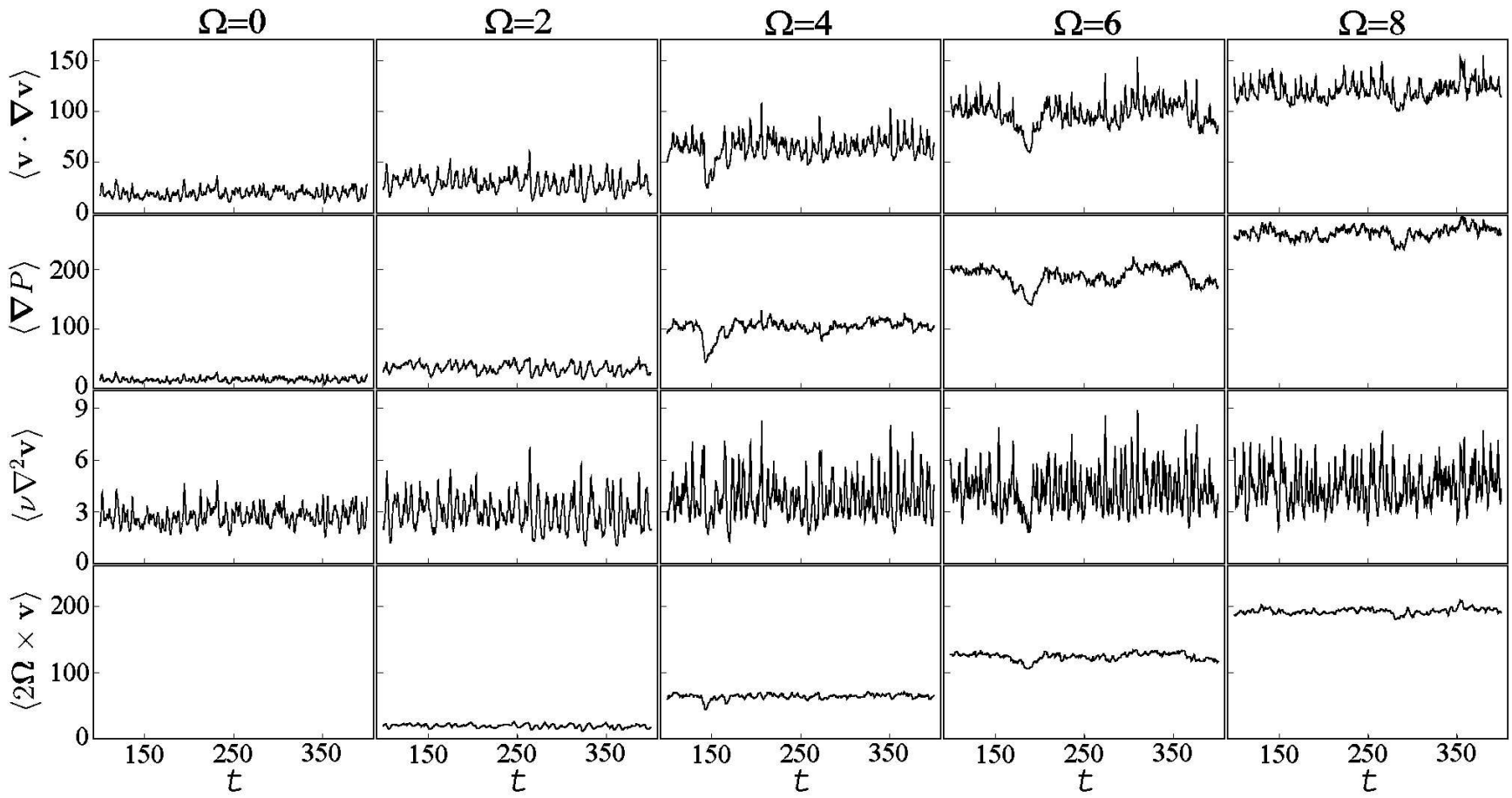

Figure 6.1: Time series (from $t = 100$ to $t = 400$) of the average inertia $\langle \mathbf{v} \cdot \boldsymbol{\nabla} \mathbf{v} \rangle$, pressure force $\langle \boldsymbol{\nabla} P \rangle$, viscous force $\langle \nu \nabla^2 \mathbf{v} \rangle$, and Coriolis force $\langle 2\boldsymbol{\Omega} \times \mathbf{v} \rangle$ for various rotation rates ($\Omega = 0$, 2, 4, 6, and 8) with $\nu^{-1} = 18$. For reference, $\langle \mathbf{F} \rangle = \sqrt{3}$.

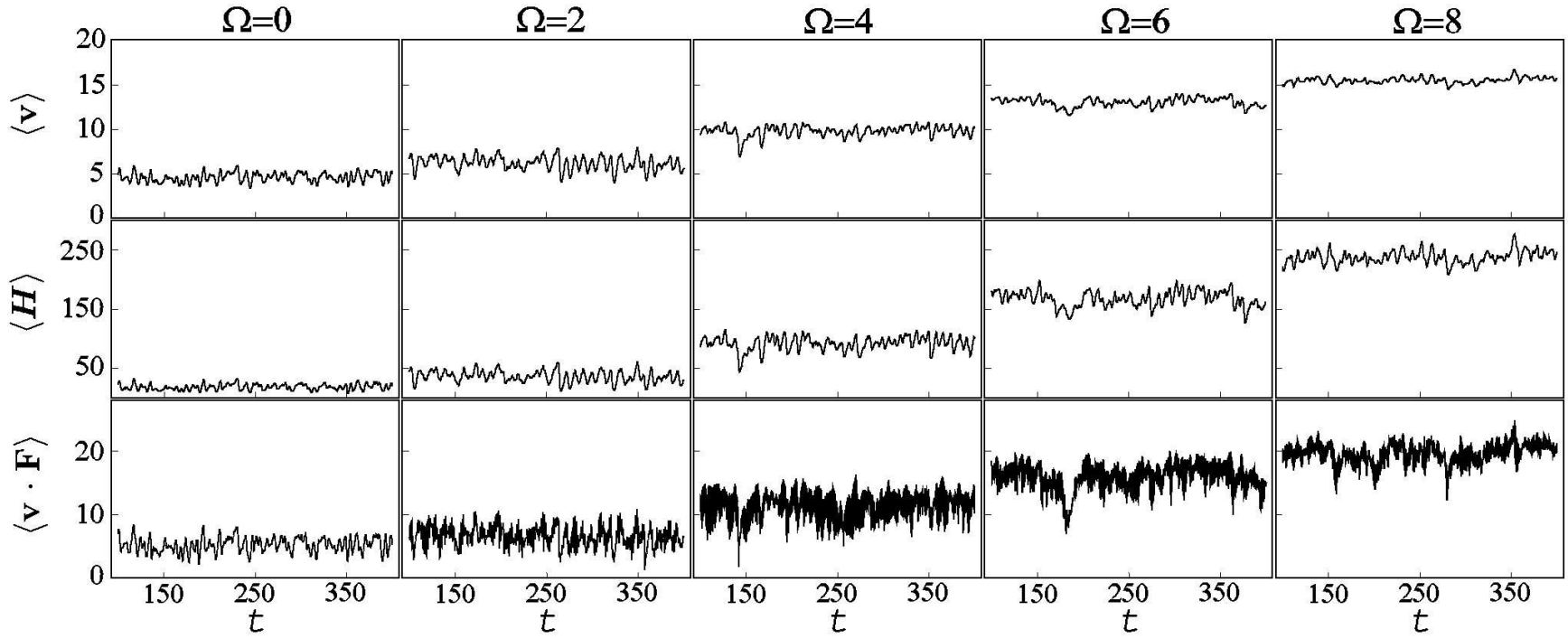

Figure 6.2: Time series (from $t = 100$ to $t = 400$) of the average velocity $\langle \mathbf{v} \rangle$, helicity $\langle \boldsymbol{H} \rangle$, and power $\langle \mathbf{F} \cdot \mathbf{v} \rangle$ for various rotation rates ($\Omega = 0$, 2, 4, 6, and 8) with $\nu^{-1} = 18$.

A convenient means of characterizing these plots is through the RMS fluctuation

$$\langle\langle\star\rangle\rangle_\sigma = \left[\frac{1}{T-t_\circ}\int_{t_\circ}^{T}\left(\langle\star\rangle - \langle\langle\star\rangle\rangle\right)^2 \mathrm{d}t\right]^{1/2}. \tag{6.3}$$

Figures 6.3, 6.4, 6.5, 6.6, 6.7, 6.8, and 6.9 show these quantities as a function of Ω for the cases $\nu^{-1} = 36$, $\nu^{-1} = 18$, and $\nu^{-1} = 6.3$. In each case the error bars do not indicate uncertainty in the mean quantity (this uncertainty is of the order of the line thickness). Rather, they extend vertically to represent the time variability of each quantity (as computed by (6.3)). We note that, when $\nu^{-1} = 6.3$, the variability $\langle\langle\star\rangle\rangle_\sigma$ in all flow variables drops to near zero for $\Omega > 4$. For these fast rotation rates, the $\nu^{-1} = 6.3$ flow is constant in time. Evidently the ABC flow is stabilized by the addition of the Coriolis force. However, the flow is turbulent and chaotic for all investigated Ω when $\nu^{-1} = 18$, as can be seen in Fig. 6.2 ($\nu^{-1} = 36$ is similarly chaotic for all Ω).

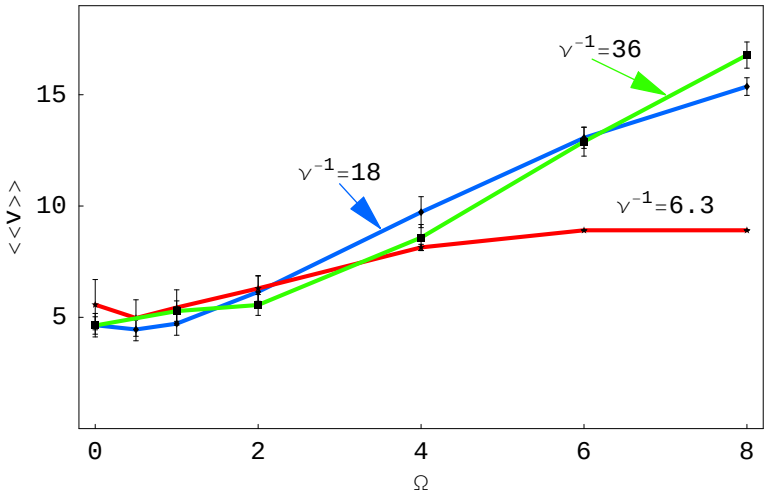

Figure 6.3: The average velocity $\langle\langle\mathbf{v}\rangle\rangle$ with varying Ω. The error bars do not indicate uncertainty in $\langle\langle\mathbf{v}\rangle\rangle$, they extend up and down by the amount $\langle\langle\mathbf{v}\rangle\rangle_\sigma$.

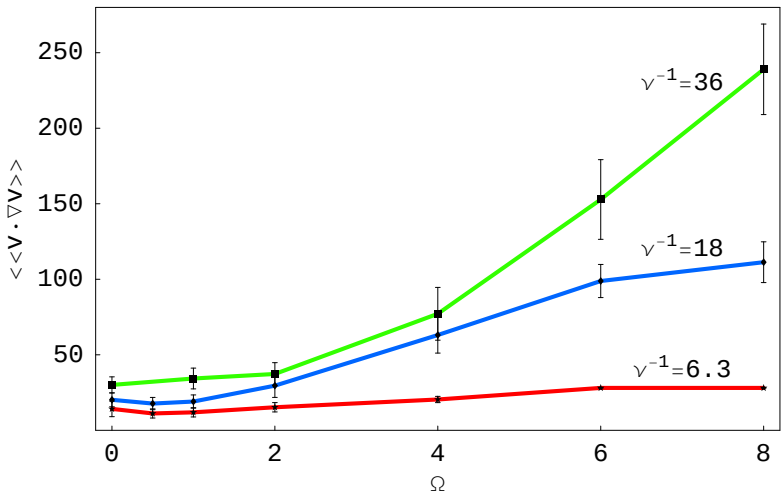

Figure 6.4: The average inertial force $\langle\langle \mathbf{v} \cdot \boldsymbol{\nabla} \mathbf{v} \rangle\rangle$ with varying Ω. The error bars do not indicate uncertainty in $\langle\langle \mathbf{v} \cdot \boldsymbol{\nabla} \mathbf{v} \rangle\rangle$, they extend up and down by the amount $\langle\langle \mathbf{v} \cdot \boldsymbol{\nabla} \mathbf{v} \rangle\rangle_\sigma$.

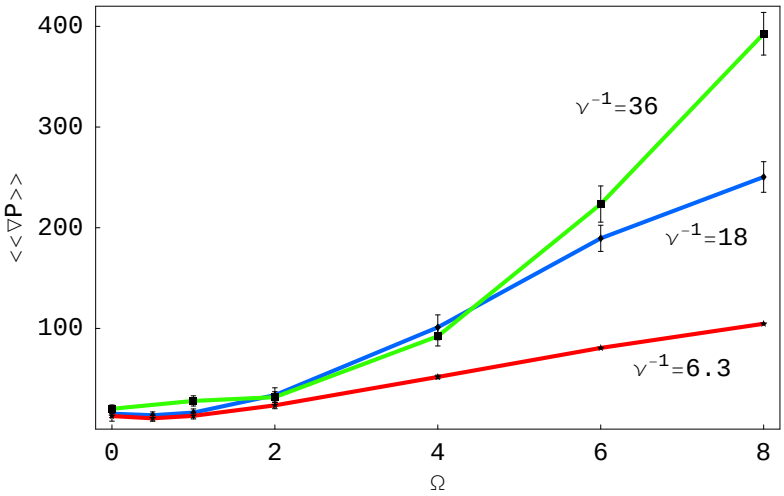

Figure 6.5: The average pressure force $\langle\langle \boldsymbol{\nabla} P \rangle\rangle$ with varying Ω. The error bars do not indicate uncertainty in $\langle\langle \boldsymbol{\nabla} P \rangle\rangle$, they extend up and down by the amount $\langle\langle \boldsymbol{\nabla} P \rangle\rangle_\sigma$.

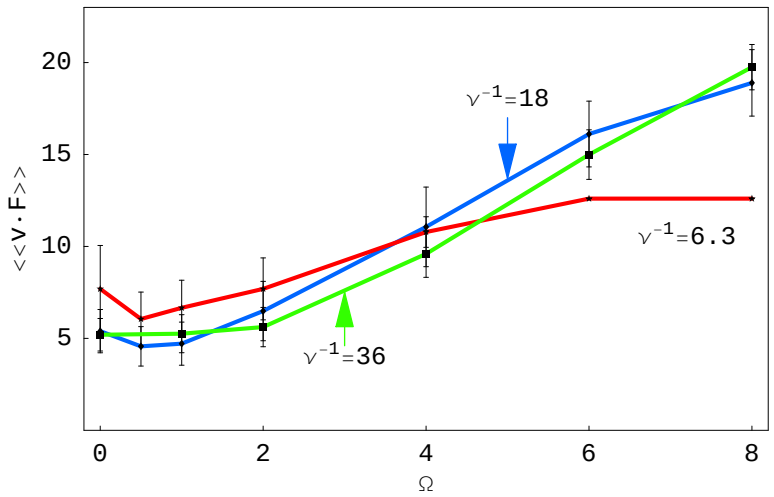

Figure 6.6: The average power $\langle\langle \mathbf{v} \cdot \mathbf{F} \rangle\rangle$ with varying Ω. The error bars do not indicate uncertainty in $\langle\langle \mathbf{v} \cdot \mathbf{F} \rangle\rangle$, they extend up and down by the amount $\langle\langle \mathbf{v} \cdot \mathbf{F} \rangle\rangle_\sigma$.

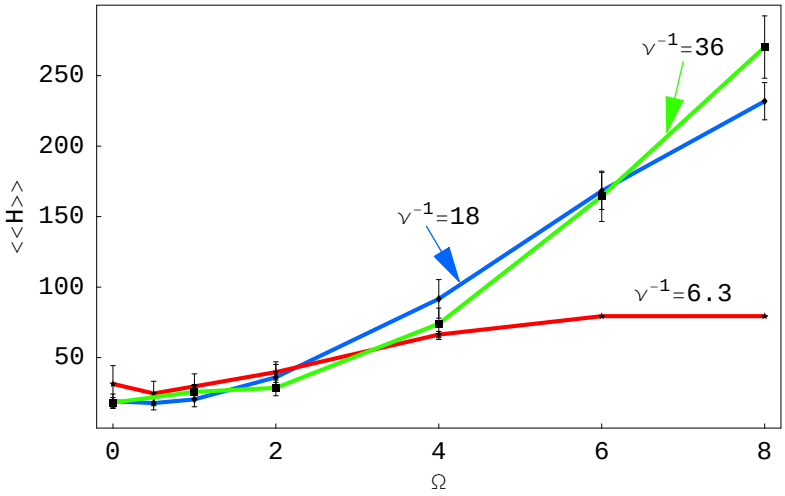

Figure 6.7: The average helicity $\langle\langle \boldsymbol{H} \rangle\rangle = \langle\langle \mathbf{v} \cdot (\boldsymbol{\nabla} \times \mathbf{v}) \rangle\rangle$ with varying Ω. The error bars do not indicate uncertainty in $\langle\langle \boldsymbol{H} \rangle\rangle$, they extend up and down by the amount $\rangle\langle \boldsymbol{H} \rangle\rangle_\sigma$.

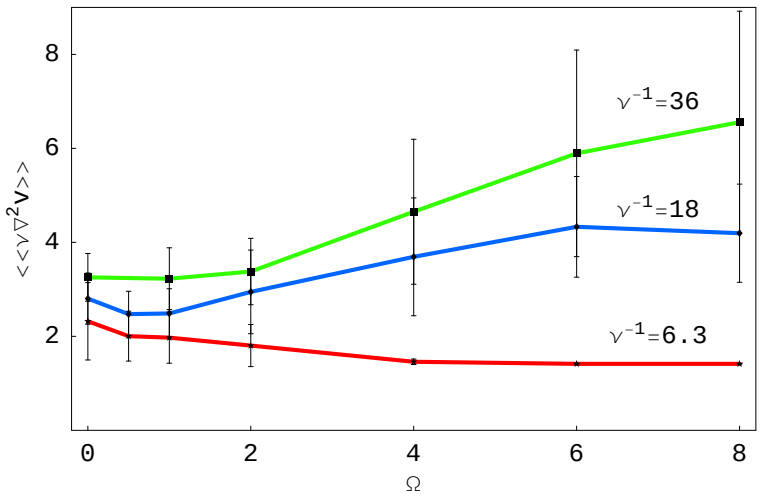

Figure 6.8: The average viscous force $\langle\langle \nu\nabla^2\mathbf{v}\rangle\rangle$ with varying Ω. The error bars do not indicate uncertainty in $\langle\langle \nu\nabla^2\mathbf{v}\rangle\rangle$, they extend up and down by the amount $\langle\langle \nu\nabla^2\mathbf{v}\rangle\rangle_\sigma$.

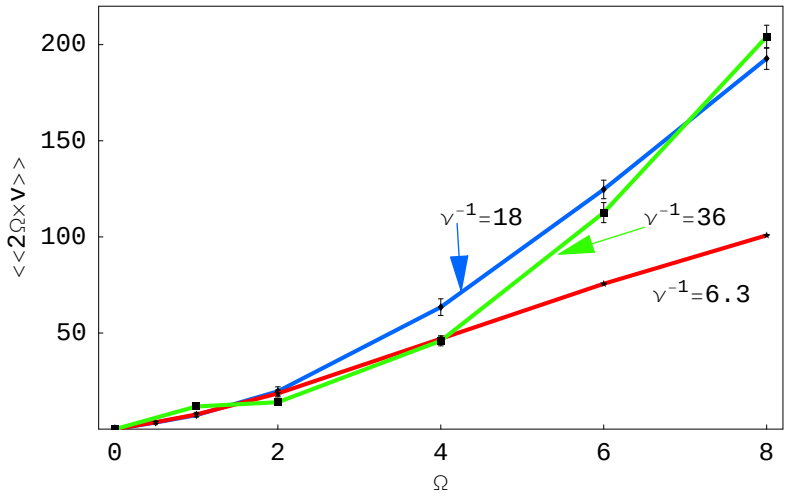

Figure 6.9: The average Coriolis force $\langle\langle 2\boldsymbol{\Omega}\times\mathbf{v}\rangle\rangle$ with varying Ω. The error bars do not indicate uncertainty in $\langle\langle 2\boldsymbol{\Omega}\times\mathbf{v}\rangle\rangle$, they extend up and down by the amount $\langle\langle 2\boldsymbol{\Omega}\times\mathbf{v}\rangle\rangle_\sigma$.

If inertial waves are present in the most rapidly rotating flows, we expect to see frequencies near 2Ω in spectra of dynamical quantities. This signal is most easily seen in the spectrum of the average power $\langle \mathbf{v} \cdot \mathbf{F} \rangle$, shown in Fig. 6.10 for $\Omega = 8$. The temporal Fourier transform of the average power is denoted $\mathrm{Pow}(\omega)$. The spectrum consists of a peak near the highest allowed frequency ($2\Omega = 16$) superimposed on a background of turbulent noise. A Gaussian fit of this power spectrum to a function of the form $c + ae^{-b*(\omega-\omega_\circ)^2}$ to the range $11.6 < \omega < 18.6$ finds the peak center at $\omega_\circ = 14.3$. Note that the $\boldsymbol{k} = 2\hat{\boldsymbol{z}} + \hat{\boldsymbol{x}}$ and $\boldsymbol{k} = 2\hat{\boldsymbol{z}} + \hat{\boldsymbol{y}}$ modes are expected to have a frequency $\omega = \frac{2}{\sqrt{5}}\Omega = 14.31$. From equation (4.18), the expected quality factor for $\boldsymbol{k} = 2\hat{\boldsymbol{z}} + \hat{\boldsymbol{y}}$ and $\boldsymbol{k} = 2\hat{\boldsymbol{z}} + \hat{\boldsymbol{x}}$ waves is $Q = 25.8$. However, a Gaussian fit to the peak in Fig. 6.10 gives an inverse fractional full width at half height of $\omega/\Delta\omega \sim 6.5$, approximately one fourth of the quality factor expected from linear theory for perturbations about $\mathbf{v} = 0$. The peak in Fig. 6.10 is a clear sign that inertial waves are present.

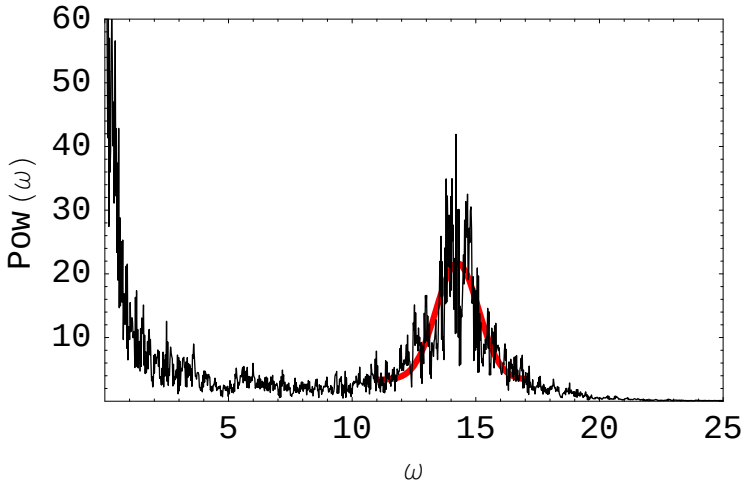

Figure 6.10: The spectrum of the spatially averaged power $\langle \mathbf{v} \cdot \mathbf{F} \rangle$ at the rotation rate $\Omega = 8$ (and $\nu^{-1} = 18$). The peak is centered at $\omega = 14.3$.

6.1.1 Flow Structure

The spatial structure of the flow develops anisotropy as rotation rates increase past $\Omega = 2$. Fig. 6.11 shows the structure of the pressure on the cube surface. The trend toward two-dimensionalization of the fluid state is evident, as predicted by the Taylor-Proudman Theorem. Figures 6.12 and 6.13 show the structure of the velocity magnitude and Coriolis force magnitude on the cube surface. The flow structure undergoes a qualitative transition as the rotation rate increases past $\Omega = 2$.

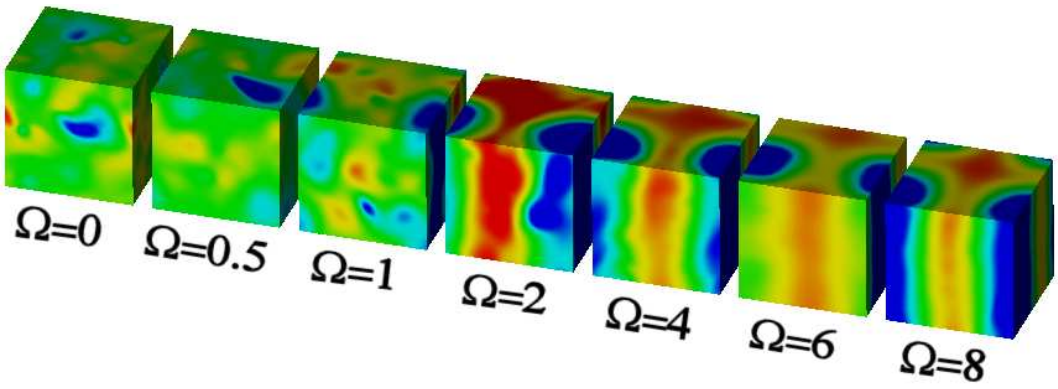

Figure 6.11: The pressure P at the time $t = T$ is shown on the cube surface for various rotation rates and $\nu^{-1} = 18$. The scale has been normalized so that the color spectrum approximately spans the range between the lowest and highest pressures attained on the cube surface. For each state, the pressure increases from blue to green to red, with pure green mapping to $P = 0$. The spatial average of the pressure is defined to be zero.

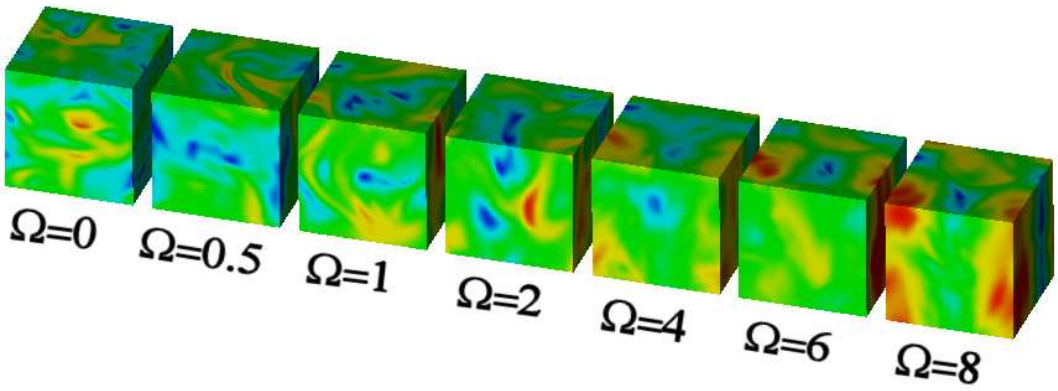

Figure 6.12: The velocity magnitude $|\mathbf{v}|$ at the time $t = T$ is shown on the cube surface for various rotation rates and $\nu^{-1} = 18$. The state is the same as that shown in Fig. 6.11. The scale has been normalized so that the color spectrum approximately spans the range between the lowest and highest velocity magnitudes on the cube surface. The velocity increases from blue to green to red.

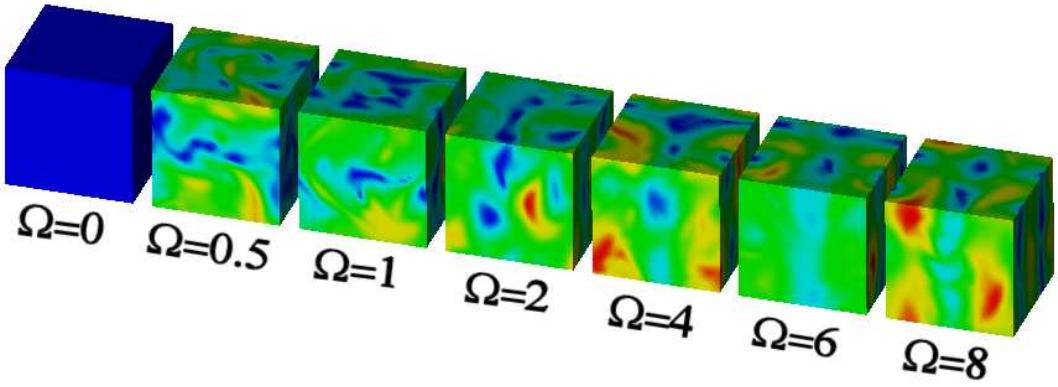

Figure 6.13: The magnitude of the Coriolis force $|2\mathbf{\Omega}\times\mathbf{v}| = 2\Omega\sqrt{v_x^2+v_y^2}$ at the time $t = T$ is shown on the cube surface for various rotation rates and $\nu^{-1} = 18$. The state is the same as that shown in Fig. 6.11 and 6.12. The scale has been normalized so that the color spectrum spans the range between the lowest and highest Coriolis force magnitude on the cube surface. The strength of the Coriolis force increases from blue to green to red.

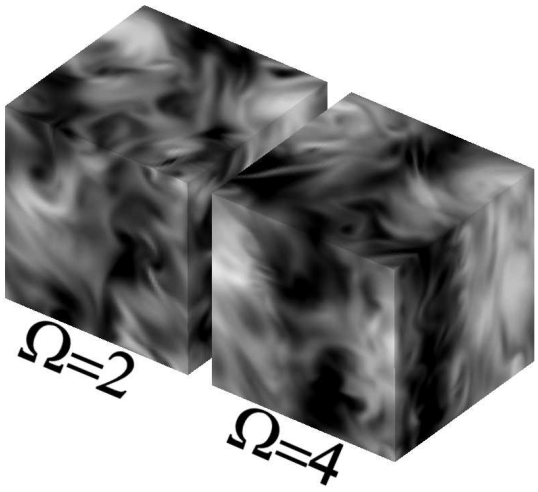

Figure 6.14: The velocity magnitude $|\mathbf{v}|$ at the time $t = T$ is shown on the cube surface for the rotation rates $\Omega = 2$ and $\Omega = 4$ for the high Reynolds number case $\nu^{-1} = 36$ at a high resolution (N=64). These similar-looking flows are vastly different in terms of their ability to generate a dynamo (as will be shown in Section 6.2). The scale has been normalized so that the color spectrum approximately spans the range between the lowest and highest velocity magnitudes on the cube surface. The velocity increases from black to white.

6.1.2 The Energy Spectrum

The one dimensional time averaged kinetic energy spectrum is

$$E_{\mathbf{v}}(k) = \frac{1}{T - t_\circ} \int_{t_\circ}^{T} \langle E_{\mathbf{v}}^{(\boldsymbol{k})} \rangle_{|\boldsymbol{k}|=k} \mathrm{d}t, \tag{6.4}$$

where $E_{\mathbf{v}}^{(\boldsymbol{k})} = \mathbb{F}\Big[|\mathbf{v}|^2/2\Big]$, and $\langle \star \rangle_{|\boldsymbol{k}|=k}$ indicates an average over all $\boldsymbol{k}$ vectors having length k. As a test case we compute the energy spectrum for a high resolution test case ($N = 96$, $K = 48$) with low viscosity $\nu^{-1} = 50$. Fig. 6.15 shows the results,

verifying that the code has produced a result roughly consistent with the expected Kolmogorov result of $E_{\mathbf{v}}(k) \sim k^{-5/3}$ in the inertial range. We regard the inertial range as extending from $k = 2$ to $k \approx 10$. $E_{\mathbf{v}}$ is largest for $k = 1$, which is the mode that $\mathbf{F}$ injects energy into.

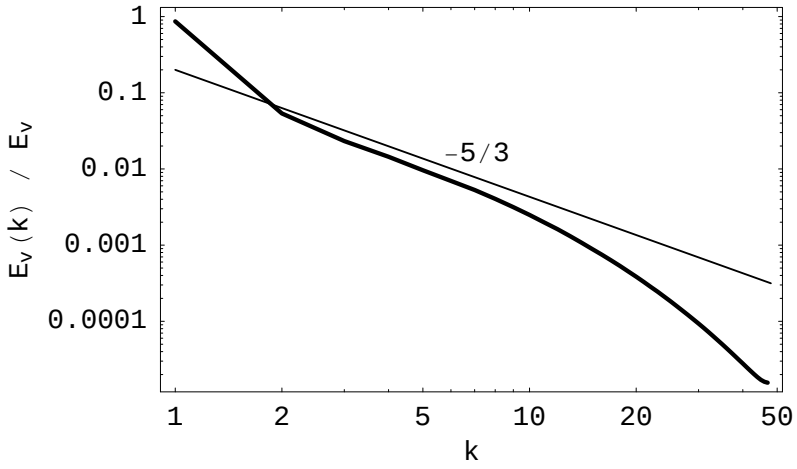

Figure 6.15: The normalized kinetic energy spectrum $E_{\mathbf{v}}(k)/E_{\mathbf{v}}$ is shown for the test case $\nu^{-1} = 50$, $\Omega = 0$, with resolution $N = 96$, $\delta t = 5 \times 10^{-4}$. The inertial range is seen to follow the expected Kolmogorov scaling in which $\log\Big(E_{\mathbf{v}}(k)\Big) \approx C_\circ - \frac{5}{3}\log(k)$ for some constant $C_\circ$.

For the range of ν investigated, there is no substantial inertial range, the arguments that lead to the k^{-2} spectrum in rotating turbulence do not hold here; a much lower ν (requiring a much higher resolution) would be needed to see this behavior. Instead, the energy spectrum exhibits k^{-3} behavior as seen in [55], although the conditions in this case are quite different (in [55] random forcing was applied at small scales, and the k^{-3} behavior was seen for scales larger than the forcing scale).

Fig. 6.16 shows the effect of rotation on the compensated kinetic energy spectrum $E_{\mathbf{v}}(k)k^3/E_{\mathbf{v}}$. These spectra are computed from $K = 32$ simulations.

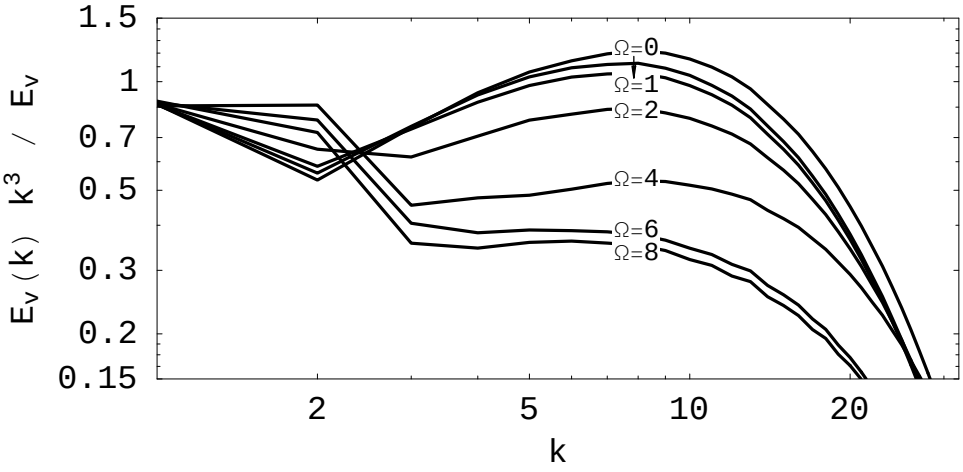

Figure 6.16: The compensated energy spectrum is shown for the rotation rates: $\Omega = 0,\ 0.5,\ 1,\ 2,\ 4,\ 6,\ 8$ with $\nu^{-1} = 18$.

One can identify a transition in the spectrum occurring between $\Omega = 1$ and $\Omega = 6$. Rotation rates below $\Omega = 2$ ($\Omega = 0,\ 0.5,\ 1$) largely follow the non-rotating expectation, with viscous dissipation at small scales causing the spectrum to curve downward, deviating from a power law. Rotation rates above $\Omega = 2$ ($\Omega = 4,\ 6,\ 8$) approximately follow a k^{-3} law from $k = 3$ to $k = 10$. This transition in the spectrum near $\Omega = 2$ coincides with the transition seen in the flow structure images of the previous section. High rotation rates have significantly more energy in the large scale $k = 2$ mode. We will see that the kinematic dynamics of the magnetic field also change substantially as the rotation rate increases past $\Omega = 2$.

6.2 Kinematic Dynamo Characterization

The growth or decay of the magnetic energy is measured by the finite time exponential growth rate

$$\sigma_\tau = \frac{1}{\tau}\log\left[\frac{E_{\mathbf{B}}(t_\circ+\tau)}{E_{\mathbf{B}}(t_\circ)}\right]. \tag{6.5}$$

The initial *seed* magnetic field $\mathbf{B}_\circ$ at time $t = t_\circ$ is random, with a small energy $E_{\mathbf{B}}(t_\circ)$ distributed evenly in the lowest 10 modes ($k = 1$ to $k = 10$). The initial velocity field $\mathbf{v}_\circ$ is taken from a long-time simulation and thus reflects a randomly chosen state from the attractor of the rotating Navier-Stokes system (4.13). The growth rate σ_τ appears to limit to a constant for large τ, we denote this constant σ_∞ as the average of σ_τ over random initial conditions for M long, ($\tau = 300$) simulations. We have

$$\sigma_\infty \approx \bar{\sigma}_\tau = \frac{1}{M}\sum_{i=1}^{M}\sigma_\tau^i, \tag{6.6}$$

where σ_τ^i denotes the value of σ_τ for initial condition i ($\mathbf{v}_\circ^i$, $\mathbf{B}_\circ^i$). The error in this approximation due to finite sampling (finite M) is estimated as

$$\Delta\sigma_\tau \approx \frac{1}{\sqrt{M}}\sqrt{\frac{1}{M-1}\sum_{i=1}^{M}(\sigma_\tau^i-\hat{\sigma}_\tau)^2}, \tag{6.7}$$

the sample standard deviation divided by $\sqrt{M}$. For $\nu^{-1} = 18$ we average over $M = 10$ initial conditions, while for $\nu^{-1} = 6.3$ we typically average over more (between $M = 10$ and $M = 20$). In the $\nu^{-1} = 36$ case, the resolution requirements are such that we only average over $M = 2$ or 3 initial conditions. Figure 6.17 shows a set of σ_τ^i time series; 10 traces for each of two different η values. Dynamo action is characterized by a positive σ_∞ indicating average growth of the seed magnetic

field, while negative σ_∞ indicates average decay of the field. Thus, in Figure 6.17 the black curves ($\eta^{-1} = 14$) show dynamo action, while the red curves ($\eta^{-1} = 10$) show an absence of dynamo action.

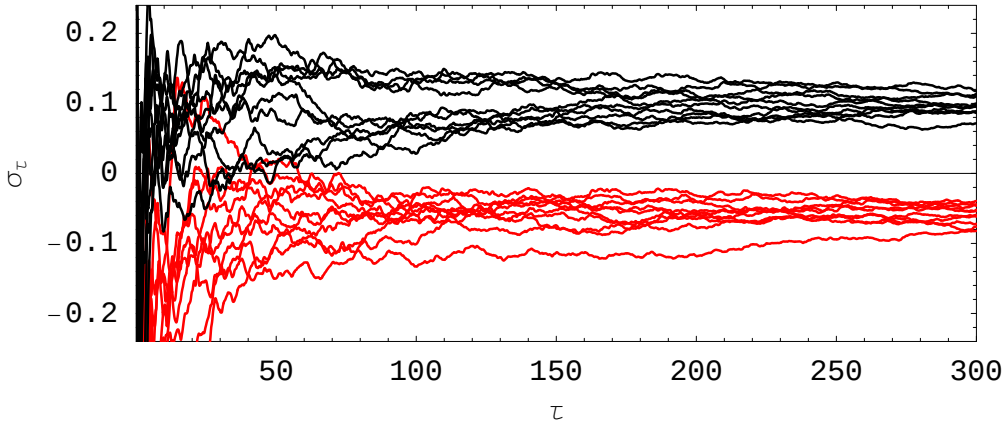

Figure 6.17: An example of the magnetic energy growth rate σ_τ converging on σ_∞ for several initial conditions. The red curves correspond to $\eta^{-1} = 10$ while the black correspond to $\eta^{-1} = 14$. In all cases $\Omega = 1$, $\nu^{-1} = 18$. From these ensembles we obtain the estimates $\sigma_\infty \approx \bar{\sigma}_{300} \pm \Delta\sigma_{300} = -0.0587 \pm 0.0129$ ($\eta^{-1} = 10$) and $\sigma_\infty \approx \bar{\sigma}_{300} \pm \Delta\sigma_{300} = 0.0967 \pm 0.0126$ ($\eta^{-1} = 14$).

For fixed ν and Ω, σ_∞ increases with η^{-1}. Fig. 6.18 shows this typically linear dependence. The critical value of η for which $\sigma_\infty = 0$ is denoted η_c. The fluid flow is independent of η, and thus for fixed ν and Ω the average velocity $U_{\rm rms} = \langle\langle \mathbf{v} \rangle\rangle$ is independent of η. We may then define (again, for fixed ν and Ω) the critical magnetic Reynolds number as $R_m^c = 2\pi U_{\rm rms}/\eta_c = 2\pi \langle\langle \mathbf{v} \rangle\rangle \eta_c^{-1}$.

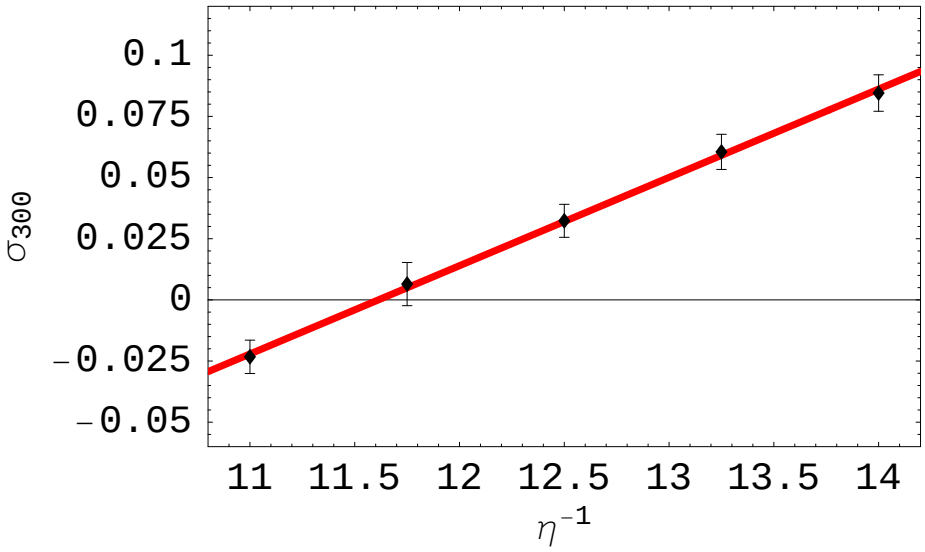

Figure 6.18: The magnetic energy growth rate versus η^{-1} for $\nu = 18^{-1}$, $\Omega = 0.5$. The red line is a linear fit to the data points, which intersects $\sigma_{300} = 0$ at a critical value of $\eta_c \approx 11.6^{-1}$.

To estimate η_c we fit the σ_∞ values to a straight line ($\bar{\sigma}_{300} = a\eta^{-1} + b$). Giving $\eta_c^{-1} = -b/a$. This fit takes into account the uncertainty $\Delta\sigma_{300}$ of each point by finding the line with maximum likelihood and assuming Gaussian statistics. This procedure is performed for several values of Ω and ν; the results are shown in Fig. 6.19. Just as the energy spectrum and flow structure change dramatically for rotation rates above $\Omega = 2$, so does the propensity for dynamo action. The value of η_c^{-1} decreases dramatically as rotation increases, indicating that rotation is desirable for the generation of a dynamo flow. The observed transition in the kinetic energy spectrum coincides with this drop in η_c^{-1} near $\Omega = 2$.

As rotation increases, so does $\langle\langle \mathbf{v} \rangle\rangle$, increasing the average input power $\langle\langle \mathbf{v} \cdot \mathbf{F} \rangle\rangle$

proportionately. In an experiment the maximum input power is typically limited by practical constraints. Thus, although the critical magnetic diffusivity has changed favorably for higher rotation rates, the critical input power dependence on Ω is crucial. The critical magnetic Reynolds number R_m^c is a more fair comparison because it multiplies η_c^{-1} by the RMS velocity, which is roughly proportional to the power input (see Fig. 6.6 and 6.3). Fig. 6.20 shows the critical magnetic Reynolds number versus rotation rate. Although the drop in R_m^c is not as large as for η_c^{-1}, there is still a significant drop as Ω increases past $\Omega = 2$. Fig. 6.20 summarizes the main result of this part of the thesis.

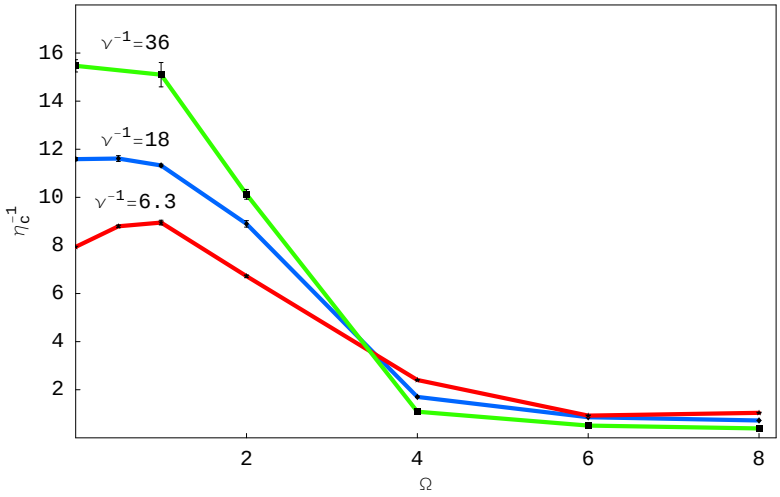

Figure 6.19: The critical magnetic diffusivity η_c^{-1} as a function of rotation rate. The error due to finite sampling of initial conditions is on the order of the line thickness. Faster rotation rates are seen to be conducive to dynamo action, with over a ten-fold decrease in η_c^{-1} when $\Omega > 4$ compared to the no rotation case.

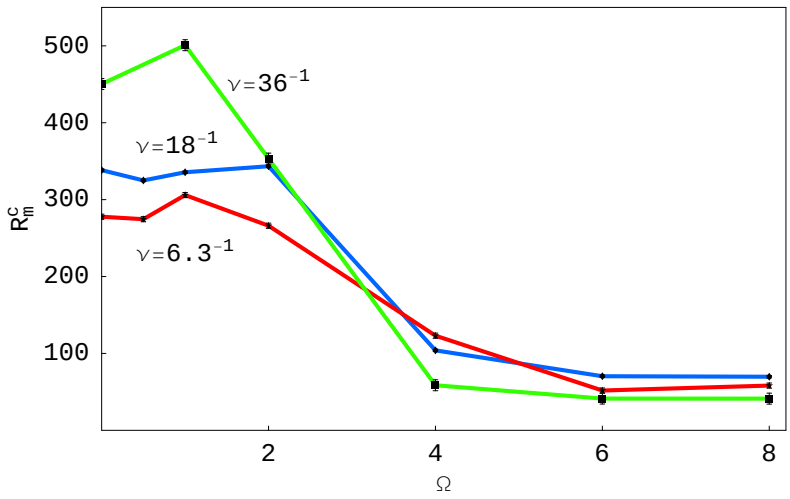

Figure 6.20: The critical magnetic Reynolds number R_m^c as a function of rotation rate. Faster rotation rates are seen to be conducive to dynamo action. The finite sample size induced uncertainty is on the order of the line thickness.

The drop off of R_m^c occurs for approximately the same values of Ω for *all* viscosities ($\nu^{-1} = 36$, $\nu^{-1} = 18$, and $\nu^{-1} = 6.3$). Thus, the viscous force is unlikely to be important in the observed behavior. The Rossby number, which compares the strength of the Coriolis force to the strength of the inertial force (not the viscosity as in the Ekman number), is the important dimensionless number. The favorable conditions for dynamo action occur for $\Omega > 4$ corresponding approximately to $Ro < 0.3$ (for $\nu^{-1} = 36$ and $\nu^{-1} = 18$).

The spatial structure of the growing magnetic field is shown in the surface of the cube for various rotation rates in Fig. 6.21. In these images, the values of η^{-1} are slightly above the value η_c^{-1} for the given rotation rate so that the magnetic field experiences average growth. These images give a sense of the spatial scale

and distribution of growing of magnetic structures in each case. The qualitative difference for different Ω largely reflects differences due to the changing η. Small scale structure is heavily suppressed for smaller η^{-1}.

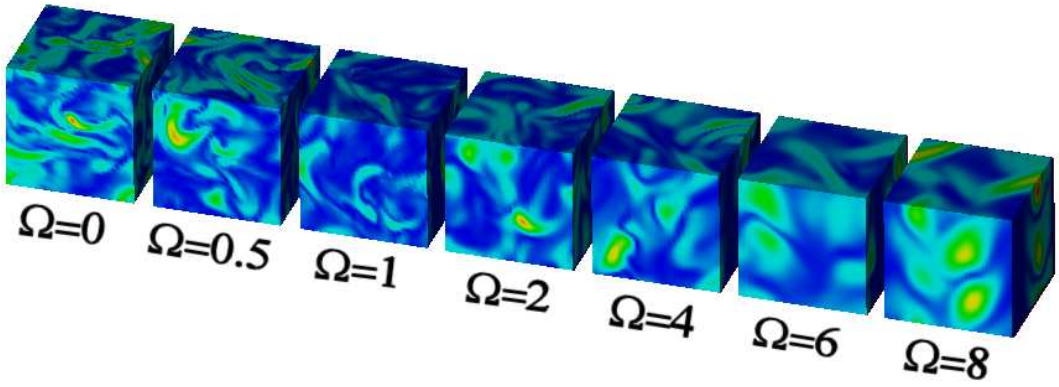

Figure 6.21: The magnitude of the magnetic field $|\mathbf{B}|$ at the time $t = T$ is shown on the cube surface for various rotation rates. Each state occurs for a value of η near (but below) η_c for that particular value of Ω; from left to right they are $\eta^{-1} = [12, 14, 14, 9, 2.5, 1.2, 0.8]$. The scale has been normalized so that the color spectrum spans the range between the lowest and highest value of $|\mathbf{B}|$ on the cube surface, where the strength of the magnetic field increases from blue to green to red.

6.3 Connection to an Envisioned Experimental Situation

Although the studied system is highly idealized (periodic boundaries, external ABC forcing, etc.), we are interested in how the reported results of section 6.2 can be used to inform and improve dynamo experiments. The important question we wish to address is this: given an available average input power density $\bar{P} = \langle\langle \bar{\mathbf{F}} \cdot \bar{\mathbf{v}} \rangle\rangle$, viscosity $\bar{\nu}$, and magnetic diffusivity $\bar{\eta}$ (and hence fixed Pr_m), is it generally beneficial to rotate the experimental apparatus (the goal being the generation of a dynamo flow)? In Fig. 6.20, the curves are for fixed ν, not fixed $\bar{\nu}$ (the relationship between ν and $\bar{\nu}$ involves $\bar{U}$ and thus the forcing strength $\bar{F}$), making Fig. 6.20 difficult to use to answer the question posed above. In our envisioned experiment, the power density $\bar{P}$ is controlled by the experimenter, who we suppose increases $\bar{P}$ until a dynamo is achieved. Thus, we wish to locate the critical power density $\bar{P}_c$, above which a dynamo is obtained for various fixed rotation rates $\bar{\Omega}$.

The average power density is

$$\bar{P} = \langle\langle \bar{\mathbf{F}} \cdot \bar{\mathbf{v}} \rangle\rangle, \tag{6.8}$$

which can also be expressed as

$$\begin{aligned} \bar{P} &= \frac{\bar{F}\bar{U}}{\sqrt{3}} \langle\langle \mathbf{F} \cdot \mathbf{v} \rangle\rangle \\ &= \frac{2\pi\bar{\rho}\bar{U}^3}{\bar{L}} \langle\langle \mathbf{F} \cdot \mathbf{v} \rangle\rangle \\ &= \frac{2\pi\bar{\rho}}{\bar{L}} \left(\frac{2\pi\bar{\eta}}{\bar{L}\eta} \right)^3 \langle\langle \mathbf{F} \cdot \mathbf{v} \rangle\rangle, \end{aligned} \tag{6.9}$$

where $\bar{U}$ depends on the magnetic diffusivity via $\bar{U} = (2\pi\bar{\eta})/(\bar{L}\eta)$. Defining the

dimensionless power to be $P = \bar{P}(\bar{L}/(2\pi))^4(1/(\bar{\rho}\bar{\eta}^3))$ we have

$$P = \frac{1}{\eta^3}\langle\langle \mathbf{F} \cdot \mathbf{v} \rangle\rangle. \tag{6.10}$$

This normalization is motivated by envisioning a situation in which a particular fluid is used (hence $\bar{\nu}$ and $\bar{\eta}$ are fixed and known) in an experiment of fixed configuration (for us with our periodic boundary conditions this corresponds to having a fixed known $\bar{L}$). Thus, in such a case, the dimensional power density $\bar{P}$ is easily computed from P, since $\bar{L}$, $\bar{\nu}$, $\bar{\eta}$, and $\bar{\rho}$ are fixed and known.

From our normalized Navier-Stokes equation 4.12, we see that the average value of $\langle\langle \mathbf{F} \cdot \mathbf{v} \rangle\rangle$ is in general a function of the dimensionless pair (ν, Ω). The normalized quantities ν and Ω involve the dimensional variable $\bar{U}$. We regard this as undesirable since $\bar{U}$ depends on $\bar{F}$ which is not fixed in our envisioned experimental situation. To remedy this, a new dimensionless variable is used,

$$C = \frac{\bar{\Omega}\bar{L}^2}{2\pi\bar{\eta}} = \frac{2\pi\Omega}{\eta}, \tag{6.11}$$

which is the ratio of the magnetic diffusion time to the rotation period. Additionally, Pr_m depends only on the fluid used; hence we express the power P as a function of C, Pr_m, and η to construct the space of dimensionless parameters (Pr_m, C, P) which has three desirable properties: 1) this triple is uniquely determined from the previously used dimensionless triple (ν, η, Ω), 2) all three quantities are easily computed from known dimensional quantities in an experiment, and 3) the relationship between $(\bar{\nu}, \bar{\eta}, \bar{\Omega})$ and (Pr_m, C, P) involves only fixed quantities.

Our procedure consists of fixing Pr_m and C, varying η to numerically find η_c, and computing the critical power $P_c(Pr_m, C) = P(Pr_m, C, \eta_c)$. To accomplish

this using our results from the previous section and without performing additional simulations for fixed values of C, we make the approximation that the surface separating the parameter space (ν, η, Ω) into dynamo and non-dynamo regions can be formed by linearly interpolating between the curves of Fig. 6.19. Fig. 6.22 shows this surface with the addition of points at $\nu^{-1} = 3$. This approximation is justified by the observation that the curves in Fig. 6.19, being roughly similar, indicate a smooth dependence on ν.

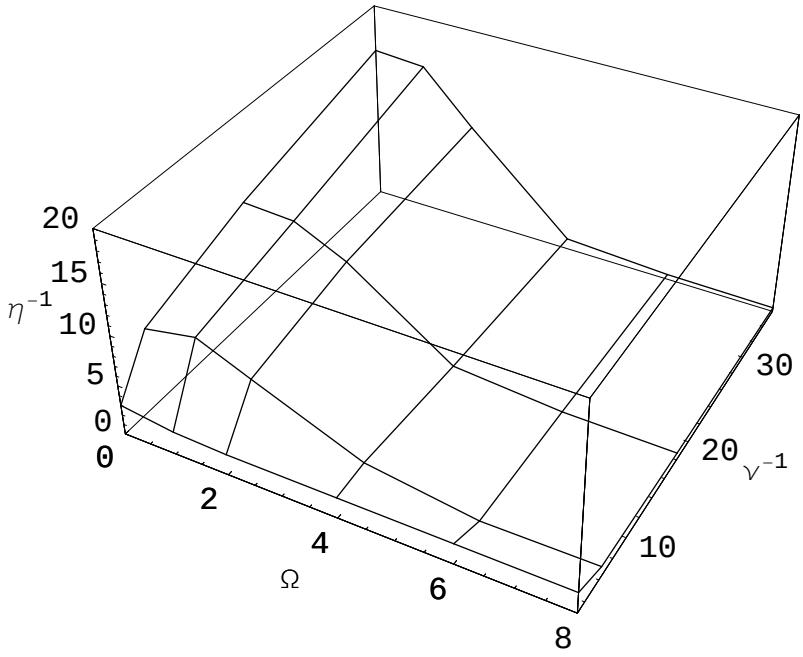

Figure 6.22: Surface seperating dynamo behavior from non-dynamo behavior for the parameter region $3 \leq \nu^{-1} \leq 36$, $0 \leq \Omega \leq 8$. Points above this surface generate a dynamo, while points below do not.

P is computed by first linearly interpolating between the curves of Fig. 6.6 to obtain a value for $\langle\langle \mathbf{F} \cdot \mathbf{v} \rangle\rangle$ for any given $(\nu,\ \Omega)$ in the range $3 \leq \nu^{-1} \leq 36$, $0 \leq \Omega \leq 8$.

This value is then multiplied by η^{-3} to obtain P (of equation (6.10)). The surface in Fig. 6.22 may then be mapped to the space (Pr_m, C, P). Fig. 6.23 shows an example of how the critical surface maps to constant Pr_m planes, demonstrating that for a fixed P, increasing the dimensionless rotation rate C is desirable for the generation of a dynamo (in the region of Pr_m investigated here).

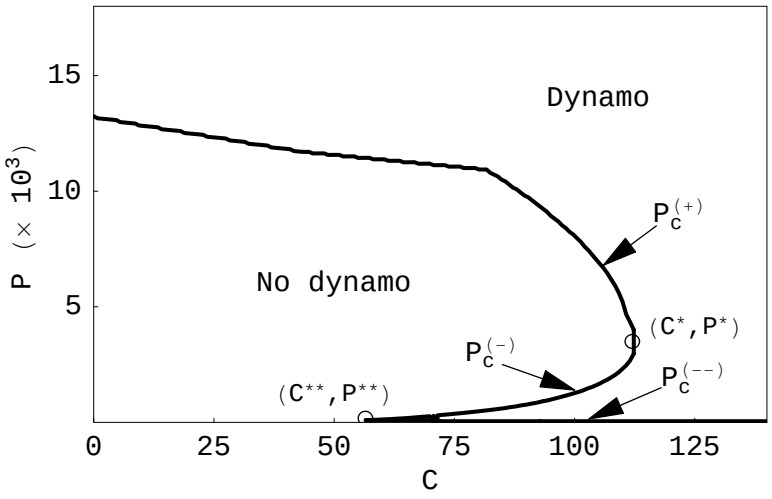

Figure 6.23: Curve separating dynamo behavior from non dynamo behavior in the plane (P, C) for $Pr_m = 0.5$.

The top portion of the curve in Fig. 6.23 is denoted $P_c^{(+)}$, the critical power above which a dynamo is always attained. The bottom surface is denoted $P_c^{(-)}$, it represents the boundary of a small dynamo window which exists for low powers. In addition, there is another critical power $P_c^{(--)} < P_c^{(-)}$ such that no dynamo action occurs for $P < P_c^{(--)}$. We define the point $(C^\star, P^\star)$ where $P_c^{(+)}$ and $P_c^{(-)}$ meet; as well as the point $(C^{\star\star}, P^{\star\star})$ where $P_c^{(-)}$ and $P_c^{(--)}$ meet (see Fig. 6.24). The curve $P_c^{(--)}$ is positive for all $C > C^{\star\star}$ (for zero power P we cannot have a dynamo). The

dynamo region is $P > P_c^{(+)}$ when $C < C^{\star\star}$, $P_c^{(--)} > P > P_c^{(-)}$ and $P > P_c^{(+)}$ when $C^{\star\star} < C < C^{\star}$, and $P > P_c^{(--)}$ when $C > C^{\star}$.

The dynamo window that exists in the range $P_c^{(--)} > P > P_c^{(-)}$ is shown in Fig. 6.24 along with the curve P_c^T for which the flow has complex time dependence for $P > P_c^T$ and is time-independent or periodic for $P < P_c^T$. The curve $P_c^{(--)}$ can be seen to exist in a region in which the power is so low that the resulting flow is not turbulent. The non-turbulent dynamo region evidently yields time independent or periodic flows having a spatial structure particularly efficient for dynamo generation. For increasing powers, turbulence develops above P_c^T in the form of fluctuations on top of a mean flow. This mean flow is similar in spatial structure to the time-independent flows just below P_c^T. Our interpretation of Fig. 6.24 is that when the additional turbulence is weak, the mean flow is able to preserve the efficient dynamo; however, as P increases past $P_C^{(-)}$, turbulence causes the flow to become disordered (perhaps introducing a greatly enhanced effective turbulence induced magnetic diffusivity) and the dynamo is lost. Above $P_c^{(+)}$ the power is sufficiently high that dynamo action occurs for highly turbulent flow.

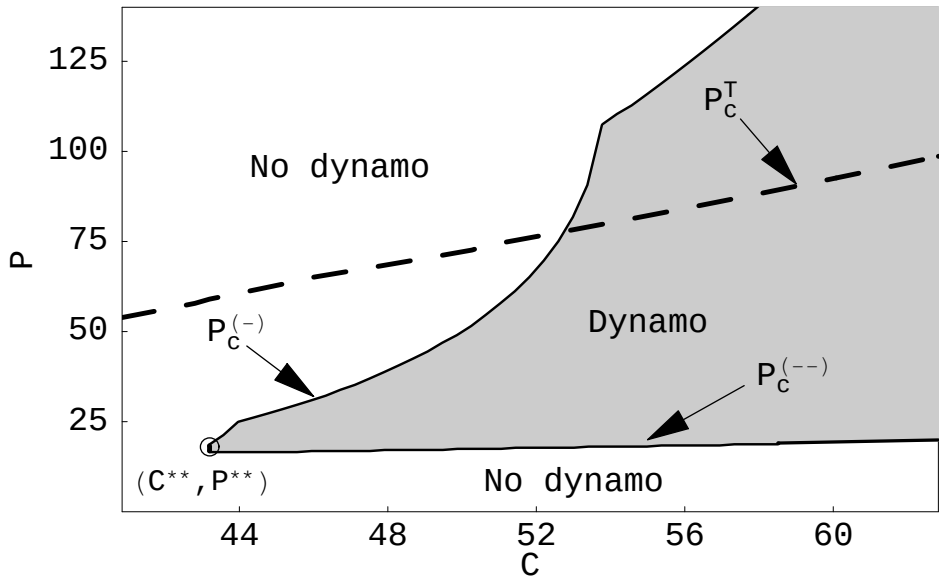

Figure 6.24: The critical power curves $P_c^{(--)}$, $P_c^{(-)}$, and P_c^T for $Pr_m = 0.2$.

Experiments operate in the regime $Pr_m \ll 1$. In principle, we wish to locate the critical power curves $P_c^{(+)}$, $P_c^{(-)}$, and $P_c^{(--)}$ in the limit as Pr_m goes to zero. The increase in η_c^{-1} with ν^{-1} seen in Fig. 6.19 corresponds to a rising $P_c^{(+)}$ as Pr_m is decreased. As one approaches the low Pr_m limit, we expect that $P_c^{(+)}$ will limit to a curve denoted $P_{c\infty}^{(+)}$ corresponding to a ν-independent η_c. This expectation is based on results obtained in the non-rotating case, demonstrating that R_m^c increases for decreasing Pr_m, reaching a plateau for small Pr_m ($Pr_m \sim 0.3$) [40]. We expect that the shape of $P_c^{(+)}$ will not be altered drastically in the limit $Pr_m \to 0$. However, investigation of very small magnetic Prandtl numbers proved to be beyond the capabilities of our available computer resources. The lowest Pr_m for which we have obtained the entire upper curve $P_c^{(+)}$ is $Pr_m \approx 0.45$. (data for which $\nu^{-1} > 36$ would be required to obtain $P_c^{(+)}$ for lower Pr_m).

Although we only obtain the upper curve for a relatively small region of Pr_m, we are able to obtain large portions of the $P_c^{(-)}$ curve as low as $Pr_m \sim 0.1$. We are uncertain as to the behavior of $P_c^{(-)}$ in the limit $Pr_m \to 0$; its behavior as Pr_m is decreased is shown in Fig. 6.25 (the dynamo window bounded by $P_c^{(-)}$ and $P_C^{(--)}$ exists for Pr_m as low as $Pr_m = 0.1$ and thus we cannot rule out its existence for $Pr_m \to 0$). The curve $P_c^{(--)}$ versus C is relatively unchanged as Pr_m decreases.

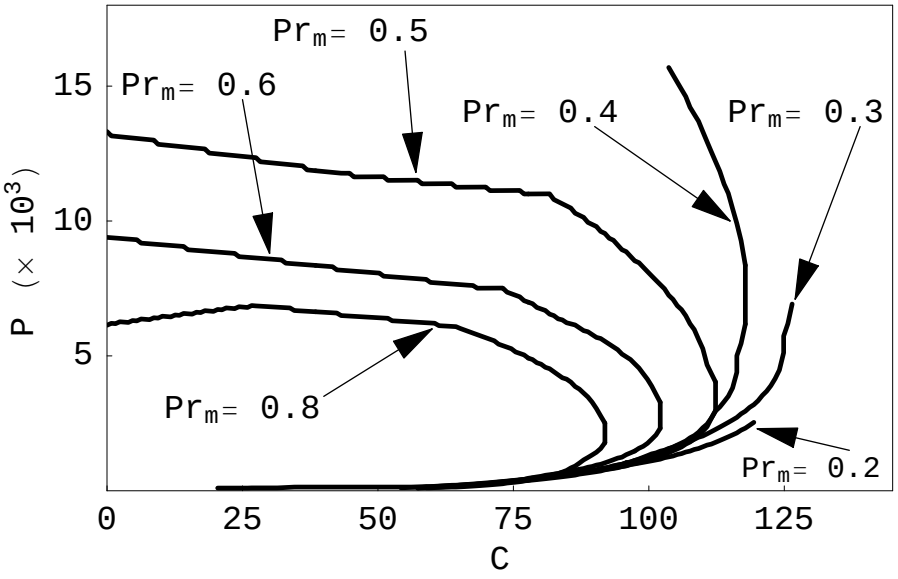

Figure 6.25: Critical power curves $P_c^{(+)}$ and $P_c^{(-)}$ versus C for several values of Pr_m; they are $Pr_m = 0.8,\ 0.6,\ 0.5,\ 0.4,\ 0.3,\ 0.2$. Curves $P_c^{(+)}$ which do not extend back to $C = 0$, are incomplete because it would require data from outside of the region $3 \leq \nu^{-1} \leq 36$.

6.4 Conclusions

As early as 1970 it was hypothesized that rotation increases the propensity for dynamo action in a magnetohydrodynamic fluid [53, 54]. Here we have shown, through the use of numerical simulations, that rotation is desirable for dynamo action. Moreover, the behavior change is marked by a sharp transition in the critical magnetic Reynolds number. This transition in magnetic behavior was found to coincide with changes in the flow structure and kinetic energy spectrum. In addition, the flow helicity grows with rotation rate, providing a possible explanation for the observed magnetic behavior.

6.4.1 Future Prospects

Our study has focused on external forcing on the scale of the domain (the largest scale $k = 1$ mode). However, quasi two-dimensional flows, which occur for the highest rotation rates investigated, are known to have an inverse energy cascade to larger scales. Studying rotation with a forcing scale small compared to the domain (perhaps with the use of a Taylor-Green vortex with $k_\circ > 1$) is thus of great interest. It is also of interest how boundaries effect the flow. These topics are appropriate for future study, when more computational recourses become available.

Appendix A

Geometric Optics Derivation of the Shadowgraph Light Intensity

The path of a light ray parameterized by the path length s is denoted $\boldsymbol{r}(s)$. Using this parameterization, $\mathbf{v} \equiv \mathrm{d}\boldsymbol{r}/\mathrm{d}s$ has magnitude 1. A light ray beginning at $\boldsymbol{r}_\circ = x_\circ \hat{\boldsymbol{x}} + y_\circ \hat{\boldsymbol{y}}$ in the xy plane with initial $\mathbf{v}$ vector pointing down along the z-axis ($\mathbf{v}_\circ = -\hat{\boldsymbol{z}}$), travels into a fluid contained between the planes $z = d/2$ and $z = -d/2$. Upon hitting the $z = -d/2$ plane, the light ray reflects and exits the fluid for subsequent imaging (through a series of lenses followed by a CCD).

In a medium with general index of refraction $n(x, y, z)$ the path satisfies

$$\frac{\mathrm{d}}{\mathrm{d}s}\left[n(\boldsymbol{r}(s))\frac{\mathrm{d}\boldsymbol{r}(s)}{\mathrm{d}s}\right] = \boldsymbol{\nabla} n(\boldsymbol{r}(\boldsymbol{s})). \tag{A.1}$$

Applying the chain rule we have

$$\left(\boldsymbol{\nabla} n(\boldsymbol{r}) \cdot \frac{\mathrm{d}\boldsymbol{r}}{\mathrm{d}s}\right)\frac{\mathrm{d}\boldsymbol{r}}{\mathrm{d}s} + n(\boldsymbol{r})\frac{\mathrm{d}^2\boldsymbol{r}}{\mathrm{d}^2 s} = \boldsymbol{\nabla} n(\boldsymbol{r}). \tag{A.2}$$

Substituting $\mathbf{v} = \mathrm{d}\boldsymbol{r}/\mathrm{d}s$ leads to

$$\frac{\mathrm{d}\mathbf{v}}{\mathrm{d}s} = \boldsymbol{R}(\boldsymbol{r}) - (\boldsymbol{R}(\boldsymbol{r}) \cdot \mathbf{v})\,\mathbf{v}, \tag{A.3}$$

$$\frac{\mathrm{d}\boldsymbol{r}}{\mathrm{d}s} = \mathbf{v}, \tag{A.4}$$

where

$$\boldsymbol{R}(\boldsymbol{r}) = \frac{\boldsymbol{\nabla} n(\boldsymbol{r})}{n(\boldsymbol{r})}. \tag{A.5}$$

The right hand side of equation (A.3) is simply the projection of $\boldsymbol{R}(\boldsymbol{r})$ onto the plane perpendicular to $\mathbf{v}$. The index of refraction of a fluid can be expressed as

$n(x,y,z) = 1 + \delta n(x,y,z)$ where δn is treated as a small perturbation, $\delta n \ll n$. We wish to treat the problem to first order in δn. Thus $\boldsymbol{R}(\boldsymbol{r})$ becomes

$$\boldsymbol{R}(\boldsymbol{r}) \approx \boldsymbol{\nabla}\delta n(\boldsymbol{r}). \tag{A.6}$$

To lowest order we ignore ray deviations within the fluid so that the ray exits the fluid at the same point it entered ($\boldsymbol{r}_\circ$). Additionally, the vector $\mathbf{v}$ is only slightly modified during transit through the fluid, thus we substitute $\mathbf{v} = \pm\hat{\boldsymbol{z}}$ in the right hand side of (A.3). This gives the simplified system

$$\frac{\mathrm{d}\mathbf{v}}{\mathrm{d}s} = \boldsymbol{R}_\perp(\boldsymbol{r}). \tag{A.7}$$

Here, the subscript $\perp$ indicates the projection of the $\boldsymbol{R}$ vector onto the xy plane. The exiting $\mathbf{v}$ vector $\mathbf{v}_e = \delta v_x\hat{\boldsymbol{x}} + \delta v_y\hat{\boldsymbol{y}} + \hat{\boldsymbol{z}}$ picks up a small component in the xy plane. The ray then travels in a straight line along the direction $\mathbf{v}_e$ to a final location $\boldsymbol{r} = (x_\circ + \delta x)\hat{\boldsymbol{x}} + (y_\circ + \delta y)\hat{\boldsymbol{y}} + (z_1 + d/2)\hat{\boldsymbol{z}}$ in the image plane, a distance $z_1 \gg d$ above the fluid. The offsets $\delta x = z_1\delta v_x$, and $\delta y = z_1\delta v_y$ are treated as perturbations. Integrating (A.7) gives

$$\begin{aligned}
\boldsymbol{\delta v}_\perp &\equiv \delta v_x\hat{\boldsymbol{x}} + \delta v_y\hat{\boldsymbol{y}} \\
&= \int_{d/2}^{-d/2} \boldsymbol{R}_\perp(\boldsymbol{r}_\circ)\mathrm{d}s + \int_{-d/2}^{d/2} \boldsymbol{R}_\perp(\boldsymbol{r}_\circ)\mathrm{d}s \\
&= 2\boldsymbol{\nabla}_\perp \int_{-d/2}^{d/2} \delta n(\boldsymbol{r}_\circ + z\hat{\boldsymbol{z}})\mathrm{d}z \qquad \text{(A.8)} \\
\boldsymbol{\delta r}_\perp &\equiv \delta x\hat{\boldsymbol{x}} + \delta y\hat{\boldsymbol{y}} = z_1\boldsymbol{\delta v}_\perp \\
&= 2z_1\boldsymbol{\nabla}_\perp \int_{-d/2}^{d/2} \delta n(\boldsymbol{r}_\circ + z\hat{\boldsymbol{z}})\mathrm{d}z \\
&= 2z_1 d\boldsymbol{\nabla}_\perp \overline{\delta n}(\boldsymbol{r}_\circ), \qquad \text{(A.9)}
\end{aligned}$$

where the overbar indicates vertically averaging, $\overline{\delta n} = (1/d)\int_{-d/2}^{d/2} \delta n \mathrm{d}z$. The map from the ray entrance point $\boldsymbol{r}_\circ$ to the final horizontal location $\boldsymbol{r}_f$ where it hits the image plane is

$$\boldsymbol{r}_f = \boldsymbol{P}(\boldsymbol{r}_\circ) \equiv \boldsymbol{r}_\circ + 2z_1 d \boldsymbol{\nabla}_\perp \overline{\delta n}(\boldsymbol{r}_\circ). \tag{A.10}$$

The map $\boldsymbol{P}$ is one-to-one since the deviation $\boldsymbol{\delta r}_\perp$ is small. The determinant of the Jacobian is the factor by which areas grow under the action of the map $\boldsymbol{P}$:

$$\begin{aligned} |\boldsymbol{DP}(\boldsymbol{r}_\circ)| &= \frac{\mathrm{d}r_{fx}}{\mathrm{d}r_{\circ x}}\frac{\mathrm{d}r_{fy}}{\mathrm{d}r_{\circ y}} - \frac{\mathrm{d}r_{fx}}{\mathrm{d}r_{\circ y}}\frac{\mathrm{d}r_{fy}}{\mathrm{d}r_{\circ x}} \\ &= \left(1 + 2z_1 d \frac{\mathrm{d}^2\overline{\delta n}}{\mathrm{d}^2 x}(\boldsymbol{r}_\circ)\right)\left(1 + 2z_1 d \frac{\mathrm{d}^2\overline{\delta n}}{\mathrm{d}^2 y}(\boldsymbol{r}_\circ)\right) - \\ &\quad 4z_1^2 d^2 \left(\frac{\mathrm{d}^2\overline{\delta n}}{\mathrm{d}x\mathrm{d}y}(\boldsymbol{r}_\circ)\right)^2 \\ &\approx 1 + 2z_1 d \nabla_\perp^2 \overline{\delta n}(\boldsymbol{r}_\circ). \end{aligned} \tag{A.11}$$

Equation (A.11) is accurate to first order in $\overline{\delta n}$. For an incident light intensity $I_\circ$ at the point $\boldsymbol{r}_\circ$ the point $\boldsymbol{r}_f$ will receive intensity $I = |\boldsymbol{DP}(\boldsymbol{r}_\circ)|^{-1} I_\circ$. Thus we have the relation

$$I(x,y) = \frac{I_\circ(x,y)}{1 + 2z_1 d \nabla_\perp^2 \overline{\delta n}(x,y)}. \tag{A.12}$$

The fluid's index of refraction varies due to spatial temperature variations. For slight dependence of n on the temperature deviation θ (ignoring the higher derivatives such as $\mathrm{d}^2 n/\mathrm{d}T^2$) we have: $\delta n = \delta n_\circ + (\mathrm{d}n/\mathrm{d}T)\theta$. Typically $\mathrm{d}n/\mathrm{d}T < 0$; a convenient form for the final shadowgraph formula is then

$$I(x,y) = \frac{I_\circ(x,y)}{1 - 2z_1 d |\mathrm{d}n/\mathrm{d}T| \nabla_\perp^2 \bar{\theta}(x,y)}. \tag{A.13}$$

Appendix B

Short-Time Nonlinear Evolution of an Initially Gaussian PDF

The goal of this appendix is to compute the initial time derivative of the mean, covariance, skewness, and kurtosis of a multivariate normal distribution (PDF, or equivalently, density of an ensemble of states) under nonlinear evolution. The last two quantities (skewness and kurtosis) are measures of deviations from normality. We consider a continuous time dynamical system

$$\frac{\partial \boldsymbol{x}}{\partial t} = \mathbf{F}(\boldsymbol{x}), \tag{B.1}$$

in which the N components of $\mathbf{F}$ can be written

$$F_i(\boldsymbol{x}) = C_i + A_{ij}x_j + B_{ijk}x_j x_k, \tag{B.2}$$

where repeated indices are summed. Without loss of generality, the B tensor is symmetric in its last two indices; $B_{ijk} = B_{ikj}$. This form of $\mathbf{F}(\boldsymbol{x})$, in which second order terms are the highest present, is very common. The Boussinesq equations (1.1), the standard Navier-Stokes equations (4.12), and the MHD equations (4.1) and (4.2) take this form when discretized in space, with all nonlinearities arising from terms which are second order in their state variables.

Denote the PDF as $\rho(\boldsymbol{x})$. Conservation of probability leads to the continuity equation in state space

$$\frac{\partial \rho}{\partial t} + \boldsymbol{\nabla} \cdot (\rho \mathbf{F}) = \frac{\partial \rho}{\partial t} + \rho \boldsymbol{\nabla} \cdot \mathbf{F} + \boldsymbol{\nabla}\rho \cdot \mathbf{F} = 0. \tag{B.3}$$

The initial ($t = t_\circ$) density $\rho_\circ(\boldsymbol{x})$ is Gaussian with covariance $\boldsymbol{\Sigma}_\circ$ and mean $\boldsymbol{\mu}_\circ$,

$$\rho_\circ(\boldsymbol{x}) = \frac{1}{(2\pi)^{N/2}|\boldsymbol{\Sigma}_\circ|^{1/2}} \exp\left[-\frac{1}{2}(\boldsymbol{x}-\boldsymbol{\mu}_\circ)^T\boldsymbol{\Sigma}_\circ^{-1}(\boldsymbol{x}-\boldsymbol{\mu}_\circ)\right]. \tag{B.4}$$

For this distribution we have $\boldsymbol{\nabla}\rho_\circ = -\boldsymbol{\Sigma}_\circ^{-1}(\boldsymbol{x}-\boldsymbol{\mu}_\circ)\rho_\circ$. It will be convenient to transform into a coordinate system in which $\rho_\circ$ is centered on the origin and normally distributed with covariance matrix equal to the $N \times N$ identity matrix. This coordinate transform is given by

$$\boldsymbol{\Delta} = \mathbf{P}_\circ^{-1}(\boldsymbol{x}-\boldsymbol{\mu}_\circ), \tag{B.5}$$

where $\mathbf{P}$ is real, symmetric, and satisfies

$$\mathbf{P}_\circ^2 = \boldsymbol{\Sigma}_\circ. \tag{B.6}$$

Using these new definitions, $\boldsymbol{\nabla}\rho_\circ = -\mathbf{P}_\circ^{-1}\boldsymbol{\Delta}\rho_\circ$. The initial time evolution of the density is then

$$\dot{\rho}_\circ \equiv \left.\frac{\partial\rho}{\partial t}\right|_{t=t_\circ} = \mathbf{P}_\circ^{-1}\boldsymbol{\Delta}\rho_\circ\cdot\mathbf{F} - \rho_\circ\boldsymbol{\nabla}\cdot\mathbf{F}. \tag{B.7}$$

Using (B.4) and (B.2), equation (B.7) becomes

$$\dot{\rho}_\circ = \rho_\circ\left[(C_i + A_{ij}x_j + B_{ijk}x_jx_k)P_{\circ il}^{-1}\Delta_l - A_{ii} - 2B_{iij}x_j\right]. \tag{B.8}$$

Eliminating $\boldsymbol{x}$ using the substitution $\boldsymbol{x} = \boldsymbol{\mu}_\circ + \mathbf{P}_\circ\boldsymbol{\Delta}$ leads to the form

$$\begin{aligned}\dot{\rho}_\circ \;=\; & \rho_\circ\Big[C_iP_{\circ il}^{-1}\Delta_l + A_{ij}\mu_{\circ j}P_{\circ il}^{-1}\Delta_l + A_{ij}P_{\circ jp}P_{\circ il}^{-1}\Delta_p\Delta_l + \\ & B_{ijk}\mu_{\circ j}\mu_{\circ k}P_{\circ il}^{-1}\Delta_l + 2B_{ijk}\mu_{\circ k}P_{\circ jp}P_{\circ il}^{-1}\Delta_p\Delta_l + B_{ijk}P_{\circ kn}P_{\circ jp}P_{\circ il}^{-1}\Delta_n\Delta_p\Delta_l - \\ & A_{ii} - 2B_{iij}\mu_{\circ j} - 2B_{iij}P_{\circ jl}\Delta_l\Big].\end{aligned} \tag{B.9}$$

Although long and seemingly cumbersome, this form is convenient because we can easily make use of the relations

$$\begin{aligned}
\int \rho_\circ \mathrm{d}\boldsymbol{x} &= 1 \,, && \text{(B.10)}\\
\int \Delta_i \rho_\circ \mathrm{d}\boldsymbol{x} &= 0 \,, && \text{(B.11)}\\
\int \Delta_i \Delta_j \rho_\circ \mathrm{d}\boldsymbol{x} &= \delta_{ij} \,, && \text{(B.12)}\\
\int \Delta_i \Delta_j \Delta_k \rho_\circ \mathrm{d}\boldsymbol{x} &= 0 \,, && \text{(B.13)}\\
\int \Delta_i \Delta_j \Delta_k \Delta_l \rho_\circ \mathrm{d}\boldsymbol{x} &= \delta_{ij}\delta_{kl} + \delta_{ik}\delta_{jl} + \delta_{il}\delta_{jk} \,, \\
&\equiv W_{ijkl}\left\{\delta\delta\right\} \,, && \text{(B.14)}\\
\int \Delta_i \Delta_j \Delta_k \Delta_l \Delta_m \rho_\circ \mathrm{d}\boldsymbol{x} &= 0 \,, && \text{(B.15)}\\
\int \Delta_i \Delta_j \Delta_k \Delta_l \Delta_m \Delta_n \rho_\circ \mathrm{d}\boldsymbol{x} &= \delta_{ij} W_{klmn}\left\{\delta\delta\right\} + \delta_{ik} W_{jlmn}\left\{\delta\delta\right\} + \\
&\quad \delta_{il} W_{jkmn}\left\{\delta\delta\right\} + \delta_{im} W_{jkln}\left\{\delta\delta\right\} + \delta_{in} W_{jklm}\left\{\delta\delta\right\} \,, \\
&\equiv W_{ijklmn}\left\{\delta\delta\delta\right\} \,, && \text{(B.16)}\\
\int \Delta_i \Delta_j \Delta_k \Delta_l \Delta_m \Delta_n \Delta_p \rho_\circ \mathrm{d}\boldsymbol{x} &= 0 \,, && \text{(B.17)}\\
&\vdots
\end{aligned}$$

These relations follow from noting that $|\boldsymbol{\Sigma}_\circ|^{1/2} = |\mathbf{P}_\circ|$ and under change of variables $\mathrm{d}\boldsymbol{x} \to |\mathbf{P}_\circ| \mathrm{d}\boldsymbol{\Delta}$.

At any time, the distribution mean is computed as

$$\boldsymbol{\mu} = \int \boldsymbol{x} \rho(\boldsymbol{x}) \mathrm{d}\boldsymbol{x}, \tag{B.18}$$

and its initial time derivative is

$$\dot{\boldsymbol{\mu}}_\circ \equiv \left.\frac{\partial \boldsymbol{\mu}}{\partial t}\right|_{t=t_\circ} = \int \boldsymbol{x} \dot{\rho}_\circ(\boldsymbol{x}) \mathrm{d}\boldsymbol{x} = \int \boldsymbol{\mu}_\circ \dot{\rho}_\circ(\boldsymbol{x}) \mathrm{d}\boldsymbol{x} + \int \mathbf{P}_\circ \boldsymbol{\Delta} \dot{\rho}_\circ(\boldsymbol{x}) \mathrm{d}\boldsymbol{x}. \tag{B.19}$$

Noting that $\int \dot{\rho}_\circ(\boldsymbol{x})\mathrm{d}\boldsymbol{x} = 0$ we have

$$\dot{\mu}_{\circ i} = P_{\circ ij} \int \Delta_j \dot{\rho}_\circ \mathrm{d}\boldsymbol{x}. \tag{B.20}$$

Only terms with odd powers of Δ in (B.9) will give non-zero contributions to this integral. After plugging (B.9) into (B.20) and using the relations $P_{\circ ij} = P_{\circ ji}$, $\Sigma_{\circ ij} = P_{\circ ik} P_{\circ jk}$, and $P_{\circ ij} P^{-1}_{\circ jk} = \delta_{ik}$, we obtain

$$\dot{\mu}_i = F_i(\boldsymbol{\mu}) + \Sigma_{\circ jk} B_{ijk}. \tag{B.21}$$

Evidently the mean evolves initially just as if it were a state evolving under the action of $\mathbf{F}$, except for a nonlinear correction due to the finite extent of the distribution. For very tight distributions (small $\boldsymbol{\Sigma}_\circ$), the distribution mean follows $\dot{\boldsymbol{\mu}} = \mathbf{F}(\boldsymbol{\mu})$.

The distribution covariance is given by

$$\Sigma_{ij} = \int (x_i - \mu_i)(x_j - \mu_j)\rho(\boldsymbol{x})\mathrm{d}\boldsymbol{x}, \tag{B.22}$$

and its initial time derivative is

$$\begin{aligned}
\dot{\Sigma}_{\circ ij} \equiv \left.\frac{\partial \Sigma_{ij}}{\partial t}\right|_{t=t_\circ} &= \int (x_i - \mu_{\circ i})(x_j - \mu_{\circ j})\dot{\rho}_\circ \mathrm{d}\boldsymbol{x} - \\
&\quad \dot{\mu}_{\circ i} \int (x_j - \mu_{\circ j})\rho_\circ \mathrm{d}\boldsymbol{x} - \dot{\mu}_{\circ j} \int (x_i - \mu_{\circ i})\rho_\circ \mathrm{d}\boldsymbol{x} \\
&= P_{\circ in} P_{\circ jm} \int \Delta_n \Delta_m \dot{\rho}_\circ \mathrm{d}\boldsymbol{x} - (\dot{\mu}_{\circ i} P_{\circ jn} + \dot{\mu}_{\circ j} P_{\circ in}) \int \Delta_n \rho_\circ \mathrm{d}\boldsymbol{x} \\
&= P_{\circ in} P_{\circ jm} \int \Delta_n \Delta_m \dot{\rho}_\circ \mathrm{d}\boldsymbol{x}.
\end{aligned} \tag{B.23}$$

Only terms with even powers of Δ in (B.9) will give non-zero contributions to this integral. After plugging (B.9) into (B.23) we obtain

$$\dot{\boldsymbol{\Sigma}}_\circ = \boldsymbol{D}\boldsymbol{F}_\circ \boldsymbol{\Sigma}_\circ + \left(\boldsymbol{D}\boldsymbol{F}_\circ \boldsymbol{\Sigma}_\circ\right)^T, \tag{B.24}$$

where $DF_{\circ ij} \equiv A_{ij} + 2B_{ijk}\mu_{\circ k}$ is defined as the Jacobian of $\mathbf{F}$ at the point $\boldsymbol{\mu}_\circ$. The same formula (B.24) is obtained when the dynamics are linear.

The skewness and kurtosis measures are given by [60] as

$$s = \int \left[(\boldsymbol{x}-\boldsymbol{\mu})^T\boldsymbol{\Sigma}^{-1}(\boldsymbol{y}-\boldsymbol{\mu})\right]^3 \rho(\boldsymbol{x})\rho(\boldsymbol{y})\mathrm{d}\boldsymbol{x}\mathrm{d}\boldsymbol{y}, \tag{B.25}$$

$$\kappa = \int \left[(\boldsymbol{x}-\boldsymbol{\mu})^T\boldsymbol{\Sigma}^{-1}(\boldsymbol{x}-\boldsymbol{\mu})\right]^2 \rho(\boldsymbol{x})\mathrm{d}\boldsymbol{x}, \tag{B.26}$$

Note that the skewness of $\rho_\circ$ is zero and the kurtosis of $\rho_\circ$ is N^2+2N (recall that N is the dimension of the space).

The initial time derivative of the skewness is

$$\begin{aligned}\dot{s}_\circ \equiv \left.\frac{\partial s}{\partial t}\right|_{t=t_\circ} = & \int \left[(\boldsymbol{x}-\boldsymbol{\mu}_\circ)^T\boldsymbol{\Sigma}_\circ^{-1}(\boldsymbol{y}-\boldsymbol{\mu}_\circ)\right]^3 (\dot{\rho}_\circ(\boldsymbol{x})\rho_\circ(\boldsymbol{y})+\rho_\circ(\boldsymbol{x})\dot{\rho}_\circ(\boldsymbol{y}))\mathrm{d}\boldsymbol{x}\mathrm{d}\boldsymbol{y} - \\ & 3\int \left[(\boldsymbol{x}-\boldsymbol{\mu}_\circ)^T\boldsymbol{\Sigma}_\circ^{-1}(\boldsymbol{y}-\boldsymbol{\mu}_\circ)\right]^2 \Big((\boldsymbol{x}-\boldsymbol{\mu}_\circ)^T\boldsymbol{\Sigma}_\circ^{-1}\dot{\boldsymbol{\Sigma}}_\circ\boldsymbol{\Sigma}_\circ^{-1}(\boldsymbol{y}-\boldsymbol{\mu}_\circ) + \\ & \dot{\boldsymbol{\mu}}_\circ^T\boldsymbol{\Sigma}_\circ^{-1}(\boldsymbol{y}-\boldsymbol{\mu}_\circ) + \dot{\boldsymbol{\mu}}_\circ^T\boldsymbol{\Sigma}_\circ^{-1}(\boldsymbol{x}-\boldsymbol{\mu}_\circ)\Big)\rho_\circ(\boldsymbol{x})\rho_\circ(\boldsymbol{y})\mathrm{d}\boldsymbol{x}\mathrm{d}\boldsymbol{y}. \end{aligned} \tag{B.27}$$

Where we have used the relation

$$\left.\frac{\partial}{\partial t}\boldsymbol{\Sigma}^{-1}\right|_{t=t_\circ} = -\boldsymbol{\Sigma}_\circ^{-1}\dot{\boldsymbol{\Sigma}}_\circ\boldsymbol{\Sigma}_\circ^{-1}. \tag{B.28}$$

The skewness is symmetric with respect to the interchange of $\boldsymbol{x}$ and $\boldsymbol{y}$. Using this fact, along with the notation $\boldsymbol{\Delta}^{(\boldsymbol{x})} = \mathbf{P}_\circ^{-1}(\boldsymbol{x}-\boldsymbol{\mu}_\circ)$, $\boldsymbol{\Delta}^{(\boldsymbol{y})} = \mathbf{P}_\circ^{-1}(\boldsymbol{y}-\boldsymbol{\mu}_\circ)$, and defining

$$\boldsymbol{L} \equiv \mathbf{P}_\circ^{-1}\boldsymbol{DF}_\circ\mathbf{P}_\circ + \mathbf{P}_\circ\boldsymbol{DF}_\circ^T\mathbf{P}_\circ^{-1}, \tag{B.29}$$

we get

$$\begin{aligned}\dot{s}_\circ = & 2\int \left[(\boldsymbol{\Delta}^{(\boldsymbol{x})})^T\boldsymbol{\Delta}^{(\boldsymbol{y})}\right]^3 \dot{\rho}_\circ(\boldsymbol{x})\rho_\circ(\boldsymbol{y})\mathrm{d}\boldsymbol{x}\mathrm{d}\boldsymbol{y} - \\ & 3\int \left[(\boldsymbol{\Delta}^{(\boldsymbol{x})})^T\boldsymbol{\Delta}^{(\boldsymbol{y})}\right]^2 (\boldsymbol{\Delta}^{(\boldsymbol{x})})^T\boldsymbol{L}\boldsymbol{\Delta}^{(\boldsymbol{y})}\rho_\circ(\boldsymbol{x})\rho_\circ(\boldsymbol{y})\mathrm{d}\boldsymbol{x}\mathrm{d}\boldsymbol{y}. \end{aligned} \tag{B.30}$$

Both integrals have odd powers of $\boldsymbol{\Delta}^{\boldsymbol{y}}$, thus evaluating the d$\boldsymbol{y}$ portion of both integrals first gives $\dot{s}_\circ = 0$.

The initial time derivative of the kurtosis is

$$\begin{aligned}
\dot{\kappa}_\circ \equiv \left.\frac{\partial \kappa}{\partial t}\right|_{t=t_\circ} &= \int \left[(\boldsymbol{x}-\boldsymbol{\mu}_\circ)^T \boldsymbol{\Sigma}_\circ^{-1}(\boldsymbol{x}-\boldsymbol{\mu}_\circ)\right]^2 \dot{\rho}_\circ \mathrm{d}\boldsymbol{x} - \\
&\quad 2\int \left[(\boldsymbol{x}-\boldsymbol{\mu}_\circ)^T \boldsymbol{\Sigma}_\circ^{-1}(\boldsymbol{x}-\boldsymbol{\mu}_\circ)\right] \Big((\boldsymbol{x}-\boldsymbol{\mu}_\circ)^T \boldsymbol{\Sigma}_\circ^{-1}\dot{\boldsymbol{\Sigma}}_\circ \boldsymbol{\Sigma}_\circ^{-1}(\boldsymbol{x}-\boldsymbol{\mu}_\circ) + \\
&\quad 2\dot{\boldsymbol{\mu}}_\circ^T \boldsymbol{\Sigma}_\circ^{-1}(\boldsymbol{x}-\boldsymbol{\mu}_\circ)\Big) \\
&= \int \left[\boldsymbol{\Delta}^T\boldsymbol{\Delta}\right]^2 \dot{\rho}_\circ \mathrm{d}\boldsymbol{x} - 2\int \left[\boldsymbol{\Delta}^T\boldsymbol{\Delta}\right] \boldsymbol{\Delta}^T \boldsymbol{L}\boldsymbol{\Delta}\rho_\circ \mathrm{d}\boldsymbol{x} \\
&= \int \Delta_i\Delta_i\Delta_j\Delta_j\dot{\rho}_\circ \mathrm{d}\boldsymbol{x} - 2\int L_{jl}\Delta_i\Delta_i\Delta_j\Delta_l\rho_\circ \mathrm{d}\boldsymbol{x}. \qquad \text{(B.31)}
\end{aligned}$$

Using (B.9) and the fact that $\delta_{ii} = N$, we arrive at

$$\begin{aligned}
\dot{\kappa}_\circ &= 4(N+2)DF_{\circ ii} - 2(N+2)L_{ii} \\
&= 0,
\end{aligned}$$

since $L_{ii} = 2DF_{\circ ii}$ (which can be shown using (B.29)).

In summary, we computed the short-time evolution of the mean, covariance, skewness, and kurtosis for a multivariate normal distribution. The results are summarized as

$$\dot{\boldsymbol{\mu}} = \mathbf{F}(\boldsymbol{\mu}) + \mathbf{B}\boldsymbol{\Sigma}_\circ, \qquad \text{(B.32)}$$

$$\dot{\boldsymbol{\Sigma}}_\circ = \boldsymbol{D}\boldsymbol{F}_\circ\boldsymbol{\Sigma}_\circ + \Big(\boldsymbol{D}\boldsymbol{F}_\circ\boldsymbol{\Sigma}_\circ\Big)^T, \qquad \text{(B.33)}$$

$$\dot{s}_\circ = 0, \qquad \text{(B.34)}$$

$$\dot{\kappa}_\circ = 0. \qquad \text{(B.35)}$$

The initial growth of these measures of skewness and kurtosis are zero; thus the

growth of skewness and kurtosis must be (at least) second order in time for short times.

Bibliography

[1] F. T. Arecchi, S. Boccaletti, and P. Ramazza. Pattern formation and competition in nonlinear optics. *Physics Reports*, 318:1–2, September 1999.

[2] H. L. Swinney and V. I. Krinsky. *Waves and Patterns in Chemical and Biological Media*. The MIT Press, December 1991.

[3] Stephen W. Morris, Eberhard Bodenschatz, David S. Cannell, and Guenter Ahlers. Spiral defect chaos in large aspect ratio rayleigh-bénard convection. *Phys. Rev. Lett.*, 71(13):2026–2029, Sep 1993.

[4] M. C. Cross and P. C. Hohenberg. Pattern formation outside of equilibrium. *Rev. Mod. Phys.*, 65(3):851–1086, 1993.

[5] P. C. Hohenberg and B. I. Shraiman. Chaotic behavior of an extended system. *Physica D Nonlinear Phenomena*, 37:109–115, July 1989.

[6] Hao-wen Xi, J. D. Gunton, and Jorge Viñals. Spiral defect chaos in a model of rayleigh-bénard convection. *Phys. Rev. Lett.*, 71(13):2030–2033, Sep 1993.

[7] R.E. Kalman. A new approach to linear filtering and prediction problems. *J. Basic Eng.*, 82:35–45, 1960.

[8] Dan Simon. *Optimal State Estimation: Kalman, H Infinity, and Nonlinear Approaches*. Wiley-Interscience, 2006.

[9] Geir Evensen. *Data Assimilation: The Ensemble Kalman Filter*. Springer, 2006.

[10] E. Ott, B. R. Hunt, I. Szunyogh, A. V. Zimin, E. J. Kostelich, M. Corazza, E. Kalnay, D. J. Patil, and J. A. Yorke. Estimating the state of large spatio-temporally chaotic systems. *Physics Letters A*, 330:365–370, September 2004.

[11] E. Ott, B. R. Hunt, I. Szunyogh, A. V. Zimin, E. J. Kostelich, M. Corazza, E. Kalnay, D. J. Patil, and J. A. Yorke. A local ensemble Kalman filter for atmospheric data assimilation. *Tellus Series A*, 56:415–+, October 2004.

[12] B.R. Hunt, E.J. Kostelich, and I. Szunyogh. Efficient data assimilation for spatiotemporal chaos: A local ensemble transform kalman filter. *Physica D*, 230:112–126, 2007.

[13] Jeffrey S. Whitaker and Thomas M. Hamill. Ensemble data assimilation without perturbed observations. *Mon. Wea. Rev.*, 130:1913, 2002.

[14] M. K. Tippett *et al.*, Mon. Wea. Rev. 131, 1485 (2003).

[15] Craig H. Bishop, Brian J. Etherton, and Sharanya J. Majumdar. Adaptive sampling with the ensemble transform kalman filter. part i: Theoretical aspects. *Mon. Wea. Rev.*, 129:420, 2001.

[16] J.L. Anderson. An ensemble adjustment kalman filter for data assimilation. *Mon. Wea. Rev.*, 129:2884, 2001.

[17] J.S. Whitaker T.M. Hamill and C. Snyder. Distance-dependent filtering of background error covariance estimates in an ensemble kalman filter. *Mon. Wea. Rev.*, 129:2776–2790, 2001.

[18] P. L. Houtekamer and Herschel L. Mitchell. A sequential ensemble kalman filter for atmospheric data assimilation. *Mon. Wea. Rev.*, 129:123, 2001.

[19] E. Bodenschatz, W. Pesch, and G. Ahlers. Recent Developments in Rayleigh-Bénard Convection. *Annual Review of Fluid Mechanics*, 32:709–778, 2000.

[20] D. A. Egolf, I. V. Melnikov, W. Pesch, and R. E. Ecke. Mechanisms of extensive spatiotemporal chaos in Rayleigh-Bénard convection. *Nature*, 404:733–736, April 2000.

[21] K.-H. Chiam, M. C. Cross, H. S. Greenside, and P. F. Fischer. Enhanced tracer transport by the spiral defect chaos state of a convecting fluid. *Phys. Rev. E*, 71(3):036205–+, March 2005.

[22] R. Schmitz, W. Pesch, and W. Zimmermann. Spiral-defect chaos: Swift-Hohenberg model versus Boussinesq equations. *Phys. Rev. E*, 65(3):037302–+, March 2002.

[23] M. C. Cross and Y. Tu. Defect Dynamics for Spiral Chaos in Rayleigh-Bénard Convection. *Physical Review Letters*, 75:834–837, July 1995.

[24] K.-H. Chiam, M. R. Paul, M. C. Cross, and H. S. Greenside. Mean flow and spiral defect chaos in rayleigh-bénard convection. *Phys. Rev. E*, 67(5):056206, May 2003.

[25] Y. Hu, R. Ecke, and G. Ahlers. Convection for Prandtl numbers near 1: Dynamics of textured patterns. *Phys. Rev. E*, 51:3263–3279, April 1995.

[26] M. Paul and M. Einarsson. Extensive Chaos in Rayleigh-Benard Convection. *APS Meeting Abstracts*, pages A10+, November 2006.

[27] F. H. Busse. Non-linear properties of thermal convection. *Reports of Progress in Physics*, 41:1929–1967, December 1978.

[28] L. S. Tuckerman. Divergence-free velocity fields in nonperiodic geometries. *J. Comput. Phys.*, 80(2):403–441, 1989.

[29] J. Swift and P. C. Hohenberg. Hydrodynamic fluctuations at the convective instability. *Phys. Rev. A*, 15(1):319–328, Jan 1977.

[30] M. C. Cross and P. C. Hohenberg. Pattern formation outside of equilibrium. *Rev. Mod. Phys.*, 65(3):851, Jul 1993.

[31] J. Lega, J. V. Moloney, and A. C. Newell. Swift-hohenberg equation for lasers. *Phys. Rev. Lett.*, 73(22):2978–2981, Nov 1994.

[32] W. Merzkirch. *Flow visualization*. New York, Academic Press, Inc., 1974. 258 p., 1974.

[33] S. Rasenat, G. Hartung, B. L. Winkler, and I. Rehberg. The shadowgraph method in convection experiments. *Exp. Fluids*, 7:412–420, 1989.

[34] J.L. Anderson and S.L. Anderson. A monte carlo implementation of the nonlinear filtering problem to produce ensemble assimilations and forecasts. *Mon. Wea. Rev.*, 127:2741, 1999.

[35] Louis M. Pecora and Thomas L. Carroll. Synchronization in chaotic systems. *Phys. Rev. Lett.*, 64(8):821–824, Feb 1990.

[36] M. R. Paul, M. I. Einarsson, P. F. Fischer, and M. C. Cross. Extensive chaos in rayleigh-b[e-acute]nard convection. *Physical Review E (Statistical, Nonlinear, and Soft Matter Physics)*, 75(4):045203, 2007.

[37] S. Morris, E. Bodenschatz, D. Cannell, and G. Ahlers. The spatiotemporal structure of spiral-defect chaos. *Physica D*, 97:164, 1996.

[38] M. Oczkowski, I. Szunyogh, and D. J. Patil. Mechanisms for the Development of Locally Low-Dimensional Atmospheric Dynamics. *Journal of Atmospheric Sciences*, 62:1135–1156, April 2005.

[39] Y. Ponty, H. Politano, and J.-F. Pinton. Simulation of Induction at Low Magnetic Prandtl Number. *Physical Review Letters*, 92(14):144503–+, April 2004.

[40] Y. Ponty, P. D. Mininni, D. C. Montgomery, J.-F. Pinton, H. Politano, and A. Pouquet. Numerical Study of Dynamo Action at Low Magnetic Prandtl Numbers. *Physical Review Letters*, 94(16):164502–+, April 2005.

[41] Y. Ponty, P. D. Mininni, J.-F. Pinton, H. Politano, and A. Pouquet. Dynamo action at low magnetic Prandtl numbers: mean flow versus fully turbulent motions. *New Journal of Physics*, 9:296–+, August 2007.

[42] D. Sweet, E. Ott, J. M. Finn, T. M. Antonsen, and D. P. Lathrop. Blowout bifurcations and the onset of magnetic activity in turbulent dynamos. *Physical Review E*, 63(6):066211–+, June 2001.

[43] N. Seehafer, F. Feudel, and O. Schmidtmann. Nonlinear dynamo with ABC forcing. *Astronomy and Astrophysics*, 314:693–699, October 1996.

[44] Paul H. Roberts and Gary A. Glatzmaier. Geodynamo theory and simulations. *Rev. Mod. Phys.*, 72(4):1081–1123, Oct 2000.

[45] C. A. Jones and P. H. Roberts. Convection-driven dynamos in a rotating plane layer. *Journal of Fluid Mechanics*, 404:311–343, February 2000.

[46] M. Meneguzzi and A. Pouquet. Turbulent dynamos driven by convection. *Journal of Fluid Mechanics*, 205:297–318, 1989.

[47] A. Brandenburg, R.L. Jennings, Å. Nordlund, M. Rieutord, R.F. Stein, and I. Tuominen. Magnetic structures in a dynamo simulation. *J. Fluid Mech.*, 306:325–352, 1996.

[48] K. R. Lang. *Astrophysical Data I. Planets and Stars.* Astrophysical Data I. Planets and Stars, X, 937 pp. 33 figs.. Springer-Verlag Berlin Heidelberg New York, 1992.

[49] P. A. Davidson. *An Introduction to Magnetohydrodynamics*. An Introduction to Magnetohydrodynamics, by P. A. Davidson, pp. 452. ISBN 0521791499. Cambridge, UK: Cambridge University Press, March 2001., March 2001.

[50] F. Krause and K.-H. Raedler. *Mean-field magnetohydrodynamics and dynamo theory*. Oxford, Pergamon Press, Ltd., 1980. 271 p., 1980.

[51] D. Galloway and U. Frisch. A note on the stability of a family of space-periodic Beltrami flows. *Journal of Fluid Mechanics*, 180:557–564, 1987.

[52] H. K. Moffatt. *Magnetic field generation in electrically conducting fluids*. Cambridge, England, Cambridge University Press, 1978. 353 p., 1978.

[53] H. K. Moffatt. An approach to a dynamic theory of dynamo action in a rotating conducting fluid. *Journal of Fluid Mechanics*, 53:385–399, 1972.

[54] H. K. Moffatt. Dynamo action associated with random inertial waves in a rotating conducting fluid. *Journal of Fluid Mechanics*, 44:705–719, 1970.

[55] L. M. Smith and F. Waleffe. Transfer of energy to two-dimensional large scales in forced, rotating three-dimensional turbulence. *Physics of Fluids*, 11:1608–1622, June 1999.

[56] P. K. Yeung and Y. Zhou. Numerical study of rotating turbulence with external forcing. *Physics of Fluids*, 10:2895–2909, November 1998.

[57] Jérôme Paret and Patrick Tabeling. Experimental observation of the two-dimensional inverse energy cascade. *Phys. Rev. Lett.*, 79(21):4162–4165, Nov 1997.

[58] M. Rieutord and L. Valdettaro. Inertial waves in a rotating spherical shell. *Journal of Fluid Mechanics*, 341:77–99, June 1997.

[59] The library used for fast Fourier transforms is the fftw library (http://www.fftw.org/).

[60] K. V. MARDIA. Measures of multivariate skewness and kurtosis with applications. *Biometrika*, 57(3):519–530, 1970.